

NUMERICAL INVESTIGATION OF THERMAL PERFORMANCE OF  
MINICHANNELS WITH TRANSVERSELY PATTERNED NON-SLIP/SLIP  
SURFACES (SUPERHYDROPHOBIC SURFACES) IN TURBULENT REGIME

A Thesis

by

MANISH HARISH VANKUDRE

Submitted to the Graduate and Professional School of  
Texas A&M University  
in partial fulfillment of the requirements for the degree of

MASTER OF SCIENCE

Chair of Committee,	Jorge L. Alvarado
Committee Members,	Diego Donzis
	Michael Pate
Head of Department,	Bryan Rasmussen

December 2021

Major Subject: Mechanical Engineering

Copyright 2021 Manish Harish Vankudre

## ABSTRACT

This study focuses on investigating the thermal performance of superhydrophobic surfaces in turbulent channel flow. The superhydrophobic surface consisted of slip and non-slip bands arranged transverse to the flow direction. A numerical investigation using CFD software Star-CCM+ was implemented on a minichannel for a Reynolds number of 5600. The  $\kappa - \omega$  turbulence model with coupled solver was used for simulating the flow. Several numerical cases were simulated to understand the effect of non-slip to slip ratio and width of non-slip bands on pressure drop and thermal performance of circular minichannels. Two non-slip to slip ratios (1 and 1/3) and three different non-slip band widths ( $0.2\delta$ ,  $0.4\delta$ ,  $0.8\delta$ ) were used in the simulation process. Parameters representative of the flow and heat transfer behavior such as boundary layer thickness, friction factor, slip length, shape factor, Nusselt number and performance evaluation criterion (PEC) were calculated to better understand the effects of non-slip to slip ratio and width of non-slip bands on thermal performance. The study concluded by investigating the impact of Reynolds number on thermal performance. In summary, the decrease in non-slip to slip ratio and increase in non-slip width lead to reduction in pressure drop and enhancement of heat transfer. Furthermore, the configuration with non-slip to slip ratio of 1/3 and non-slip width of  $0.8\delta$  was found to be the optimal design, achieving a 40% reduction in pressure drop and a PEC value of 3.39.

## ACKNOWLEDGEMENTS

First and foremost, I would like to thank my committee chair, Dr. Jorge L. Alvarado, for his guidance and mentorship. He has always been extremely helpful and has generously shared his knowledge with me throughout the numerous discussions we had during this research work.

Personally, I want to mention my lab mate, Pavanrohith Govindaraju, who kept motivating me and was always available to help me. Thanks also go to my friends and colleagues and the department faculty and staff for making my time at Texas A&M University a great experience.

Finally, I would like to thank my parents, Dr. Harish, and Dr. Meena Vankudre, my sister Mrs. Nirmiti Vankudre and my brother-in-law Mr. Bhushan Jagtap for their continuous support and encouragement throughout my masters' journey.

## CONTRIBUTORS AND FUNDING SOURCES

### *Contributors:*

This work was supervised by a thesis committee consisting of Professor Jorge Alvarado, Professor Michael Pate of the Department of Mechanical Engineering, and Professor Diego Donzis of the Department of Aerospace Engineering.

All the work conducted for the thesis was completed by the student independently.

### *Funding Sources:*

Graduate study was supported by a graduate fellowship from the J. Mike Walker '66 Department of Mechanical Engineering.

## NOMENCLATURE

$a$	Width of non-slip band
$b$	Width of slip band
$D$	Diameter of minichannel
$f$	Friction factor
GCI	Grid Convergence Index
$h_z$	Local convective heat transfer coefficient
FR	Fractal ratio
$k$	Thermal conductivity
LR	Length ratio
$L$	Length of minichannel
$l_s$	Length of the cavity
$\dot{m}$	Mass flow rate
$Nu_z$	Local Nusselt number
PEC	Performance evaluation criterion
Pr	Prandtl Number
$Re_D$	Reynolds number based on hydraulic diameter
$Re_\theta$	Reynolds number based on momentum thickness
SHS	Superhydrophobic surface
$T_s$	Surface temperature
$T_c$	Centerline temperature
$u_\tau$	Friction velocity

$V_s$	Slip velocity
$\bar{v}$	Average velocity
$x^+$	Wall units
$\rho$	Density of fluid
$\delta$	Radius of minichannel
$\delta_t$	Thermal boundary layer thickness
$\delta_x$	Hydrodynamic boundary layer thickness
$\sigma$	Grid size
$\beta$	Liquid-solid-vapor contact angle
$\mu$	Dynamic viscosity

## TABLE OF CONTENTS

	Page
ABSTRACT .....	ii
ACKNOWLEDGEMENTS .....	iii
CONTRIBUTORS AND FUNDING SOURCES.....	iv
NOMENCLATURE.....	v
TABLE OF CONTENTS .....	vii
LIST OF FIGURES.....	ix
LIST OF TABLES .....	xii
CHAPTER I INTRODUCTION .....	1
1.1 Motivation.....	1
1.2 Thesis Overview.....	3
CHAPTER II LITERATURE REVIEW.....	4
2.1 Low drag surfaces with microscale modifications.....	4
2.2 Superhydrophobic Surface (SHS) in laminar flow regime .....	9
2.3 Superhydrophobic Surfaces (SHS) in turbulent flow regime.....	14
Experimental Studies.....	14
Numerical Studies .....	17
Thermal Performance Studies .....	22
CHAPTER III RESEARCH GAPS IDENTIFIED AND OBJECTIVES OF THE STUDY.....	25
3.1 Research Gaps Identified .....	25
3.2 Objectives of Study .....	26
CHAPTER IV NUMERICAL METHODOLOGY.....	27
4.1 Computational Fluid Dynamics Approach for SHS.....	28
Problem Formulation.....	29
Numerical Generation of Physical Domain .....	30

Fluid and Solid Material Selection.....	33
Governing Equations for CFD Analysis .....	34
Mesh Generation .....	36
Boundary Conditions.....	47
Solver Selection.....	51
Convergence criterion for the numerical study .....	53
Post Processing.....	54
4.2 Grid Independence Study .....	58
<b>CHAPTER V RESULTS AND DISCUSSION .....</b>	<b>61</b>
5.1 Grid Independence Study .....	61
5.2 Validation of Numerical Scheme .....	62
Thermal Validation .....	65
Validation of pressure drop in circular minichannel .....	66
5.3 Effect of non-slip/slip ratio and width of non-slip bands on pressure drop .....	66
5.4 Effect of non-slip/slip bands on slip velocity.....	68
5.5 Effect of non-slip/slip bands on local first shape factor.....	74
5.6 Effect of non-slip/slip bands on local slip length.....	78
5.7 Effect of non-slip/slip bands on boundary layer thickness .....	81
5.8 Effect of non-slip/slip bands on local Nusselt number ( $Nu_z$ ) and local convective heat transfer coefficient ( $h_z$ ) and PEC.....	89
Performance Evaluation Criterion (PEC).....	99
5.9 Effect of Reynolds number on the thermal performance of circular minichannel .....	100
<b>CHAPTER VI CONCLUSION AND SCOPE FOR FUTURE WORK .....</b>	<b>103</b>
6.1 Conclusion.....	103
6.2 Scope for future work.....	104
<b>REFERENCES .....</b>	<b>106</b>
<b>APPENDIX A MATLAB CODE FOR SHAPE FACTOR CALCULATIONS.....</b>	<b>110</b>
<b>APPENDIX B STARCCM+ MACRO FOR PLANE GENERATION .....</b>	<b>111</b>



## LIST OF FIGURES

	Page
Figure 1. Variation of power per rack over a decade [2] .....	2
Figure 2. Bionic surfaces - (a) placoid-shaped grooves, (b) V-shaped grooves, (c) riblet-shaped grooves and (d) ridge-shaped grooves (Reprinted from [7]) .....	5
Figure 3. Lotus leaf with water droplet (Reprinted from [9]) .....	6
Figure 4. Water droplet on (a) smooth surface, (b) superhydrophobic surface with Wenzel state, (c) superhydrophobic surface with Cassie-Baxter state (Reprinted from [10]) .....	7
Figure 5. Schematic representing SHS interaction with water (Reprinted from [11]).....	8
Figure 6. Meniscus formation over the micro structured surface with varying pitch values (Reprinted from [14]) .....	10
Figure 7. Variation of product of friction factor and Reynolds number with respect to Reynolds number for different ridge geometries (Reprinted from [16]).....	11
Figure 8. Different micro surface geometries - (a) square holes, (b) square posts, (c) longitudinal grooves and (d) transverse grooves (Reprinted from [19]) .....	13
Figure 9. Test section used by Woolford <i>et al.</i> [23] (Reprinted from [23]).....	15
Figure 10. (a) Ridge and (b) square post surface structures considered by Martell <i>et al.</i> [32] (Reprinted from [32]).....	19
Figure 11. Surface texture: (a) Square Posts (b) Streamwise ridge (Reprinted from [38]) .....	23
Figure 12. General methodology for a CFD analysis.....	28
Figure 13. Simulated minichannel with SHS features .....	29
Figure 14. SOLIDWORKS model of the rectangular minichannel used for validation purposes .....	31
Figure 15. Isometric view of the SOLIDWORKS circular minichannel model .....	32
Figure 16. (a) Structured Mesh [41].....	37
Figure 17. Circular pipe with source and target surfaces .....	39

Figure 18. Circular pipe with patches .....	39
Figure 19. Source and target specification for a rectangular channel .....	41
Figure 20. Source surface and patch for channel .....	41
Figure 21. Surface mesh for rectangular channel geometry.....	42
Figure 22. Surface mesh in the near wall region of channel geometry .....	43
Figure 23. Volume mesh generated for rectangular minichannel .....	43
Figure 24. Source and target surfaces representative used to generate volume mesh for a minichannel .....	44
Figure 25. Butterfly face mesh for circular minichannel .....	44
Figure 26. 2D surface of minichannel with patches.....	45
Figure 27. Patch near the solid-liquid interface .....	45
Figure 28. Initial surface mesh for minichannel geometry .....	47
Figure 29. Volume mesh for minichannel geometry.....	47
Figure 30. Rectangular minichannel with boundary assignments.....	48
Figure 31. Circular minichannels with solid and liquid domain boundary assignments .	50
Figure 32. Variation of normalized mean velocity with $y^+$ values for uncontrolled turbulence case.....	63
Figure 33. Variation of normalized mean velocity with respect to $y^+$ values for transverse ridges case .....	64
Figure 34. Slip velocity contour for non-slip to slip ratio 1.0 and non-slip width of (a) $0.2\delta$ , (b) $0.4\delta$ , (c) $0.8\delta$ .....	69
Figure 35. Slip velocity contour for non-slip to slip ratio 1/3 and non-slip width of (a) $0.2\delta$ , (b) $0.4\delta$ , (c) $0.8\delta$ .....	70
Figure 36. Slip velocity profile for non-slip to slip ratio of 1.0 and non-slip width of (a) $0.2\delta$ , (b) $0.4\delta$ , (c) $0.8\delta$ .....	71
Figure 37. Slip velocity profile for non-slip to slip ratio of 1/3 and non-slip width of (a) $0.2\delta$ , (b) $0.4\delta$ , (c) $0.8\delta$ .....	73

Figure 38. Local first shape factor for non-slip to slip ratio of 1.0 and non-slip width of (a) $0.2\delta$ , (b) $0.4\delta$ , (c) $0.8\delta$ .....	75
Figure 39. Local first shape factor for non-slip to slip ratio of 1/3 and non-slip width of (a) $0.2\delta$ , (b) $0.4\delta$ , (c) $0.8\delta$ .....	77
Figure 40. Local slip length for non-slip to slip ratio of 1.0 and non-slip width of (a) $0.2\delta$ , (b) $0.4\delta$ , (c) $0.8\delta$ .....	79
Figure 41. Local slip length for non-slip to slip ratio of 1/3 and non-slip width of (a) $0.2\delta$ , (b) $0.4\delta$ , (c) $0.8\delta$ .....	81
Figure 42. Boundary layer thicknesses for base case simulation .....	82
Figure 43. Boundary layer thickness for non-slip to slip ratio of 1.0 and non-slip width of (a) $0.2\delta$ , (b) $0.4\delta$ , (c) $0.8\delta$ .....	84
Figure 44. Boundary layer thickness for non-slip to slip ratio of 1/3 and non-slip width of (a) $0.2\delta$ , (b) $0.4\delta$ , (c) $0.8\delta$ .....	85
Figure 45. Geometry with slip (black) and non-slip (grey) bands for the case with slip surface at the inlet .....	87
Figure 46. Thermal boundary layer thickness for non-slip to slip ratio of 1/3 and non-slip width of $0.4\delta$ for the case with slip surface at the inlet .....	88
Figure 47. $h_z$ and $Nu_z$ variation with respect to streamwise distance for base case with non-slip walls.....	89
Figure 48. $h_z$ and $Nu_z$ values for non-slip to slip ratio of 1 and non-slip width of (a) $0.2\delta$ , (b) $0.4\delta$ , (c) $0.8\delta$ .....	91
Figure 49. $h_z$ and $Nu_z$ values for non-slip to slip ratio of 1/3 and non-slip width of (a) $0.2\delta$ , (b) $0.4\delta$ , (c) $0.8\delta$ .....	92
Figure 50. $\delta t/\delta x$ and $h_z$ values for non-slip to slip ratio of 1.0 and non-slip width of (a) $0.2\delta$ , (b) $0.4\delta$ and (c) $0.8\delta$ .....	96
Figure 51. $\delta t/\delta x$ and $h_z$ values for non-slip to slip ratio of 1/3 and non-slip width of (a) $0.2\delta$ , (b) $0.4\delta$ and (c) $0.8\delta$ .....	98
Figure 52. Relative slip velocity for the two non-slip/slip cases .....	101

## LIST OF TABLES

	Page
Table 1. Numerically simulated non-slip/slip cases.....	30
Table 2. Numerically simulated non-slip/slip cases.....	32
Table 3. Properties of water at 300K.....	33
Table 4. Properties of copper at 300K.....	34
Table 5. Parameter assigned for surface mesh generation in a rectangular channel .....	42
Table 6. Parameters assigned for surface mesh in circular minichannel.....	46
Table 7. Boundary conditions for rectangular minichannel .....	49
Table 8. Boundary conditions for fluid and solid domain in circular minichannel .....	51
Table 9. CFD solvers and models used in the numerical study .....	52
Table 10. CFD solution method options used in the numerical study .....	53
Table 11. Mesh sizes considered for grid independence study .....	61
Table 12. Convective heat transfer coefficient for different grids .....	62
Table 13. GCI and extrapolated values for refined grids .....	62
Table 14. Cases considered for numerical validation .....	63
Table 15. Normalized Bulk Velocity Comparison for Uncontrolled Turbulence.....	64
Table 16. Comparison of normalized bulk velocity for 1:1 ridges .....	65
Table 17. Analytical and simulated values of average Nusselt number for circular minichannel.....	65
Table 18. Analytical and simulated pressure drop value for circular minichannel.....	66
Table 19. Nonslip/slip configurations simulated in the study.....	67
Table 20. Nusselt number values for the non-slip/slip case simulated .....	94

Table 21. Nusselt number, friction factor, and PEC values for different configurations for Re of 5600 .....	99
Table 22. Nusselt number, friction factor, and PEC values .....	100
Table 23. Nusselt number for laminar and turbulent flow cases.....	102
Table 24. Pressure Drop for laminar and turbulent flow cases .....	102

# CHAPTER I

## INTRODUCTION

### **1.1 Motivation**

The modern world is constantly in the race to design and create devices that are not only fast but also more efficient and smaller in dimension. From electronic devices to computers, where high-speed data transfer and server processing takes place, to mechanical devices like turbines, compressors, and heat exchangers, excessive heat generation can lead to a reduction in the life of the system. In the case of electronic devices, a substantial amount of heat is generated on a per-volume basis, which needs to be managed effectively at a millimeter scale.

With the development in computing technologies, many researchers believe that Moore's law is no longer applicable with the industry doubling the number of components in less than two years [1]. From the thermal stance, this means that the increase in components leads to an increase in heat-generating devices, and in turn, leads to an increase in power density of the whole system. Figure 1 shows the trend for increase in power density per rack for data centers over the course of 10 years [2].

Thus, focusing on thermal transport has become a very crucial aspect to enable further miniaturization of electronic systems. The two important factors, which have a major impact on the thermal transport and sizing of the component are: chip surface temperature and the amount of energy required to manage the corresponding thermal load.

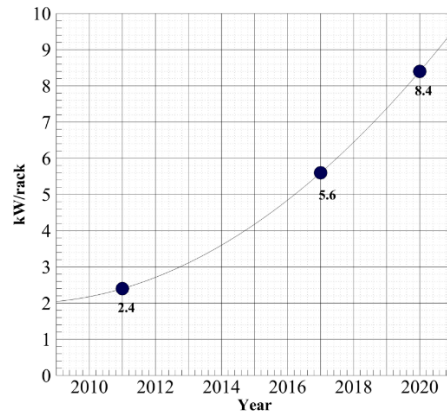


Figure 1. Variation of power per rack over a decade [2]

When single-phase fluid systems are used in electronic systems, the temperature rise, and pressure drop of the working fluid across the component should be taken into account. Failure to account for temperature rise in electronic systems could lead to a shorter silicon chip lifespan as described by Bar-Cohen [3], where a 2°C-temperature rise could result in a 10% reduction in the silicon chip reliability.

To counter the issue of temperature rise caused by increasing power density and reducing the component size, many methods have been proposed such as air cooling, direct liquid cooling, and microchannel heat sinks with intricate channel geometries. The issue with these methods is that they experience significant pressure drop at a moderate flow rate, which in turn increases the pumping power required to maintain a constant flow rate. As it is well known, the pressure drop is caused by the shear stress present near the liquid-solid interface when the fluid is in motion. With the development of microfluidic and other microscale devices, ways to reduce this frictional resistance have been sought [4,5]. For instance, superhydrophobic surfaces (SHS) are known to exhibit low-pressure

drop when used in heat exchanger devices [6]. However, little is known about the effects of superhydrophobic surfaces (SHS) as potential slip-surface in cooling systems requiring low-pressure drop. Thus, there is a need for an effective methodology that would reduce the pressure drop and facilitate efficient heat dissipation.

## **1.2 Thesis Overview**

The information presented in this thesis aims at understanding the thermal performance of superhydrophobic surfaces arranged transversally when used to induce a slip boundary condition under a turbulent regime. It starts with a comprehensive literature review exploring the studies carried out related to superhydrophobic surfaces in the laminar and turbulent flow regimes. The review also delves into the experimental and numerical simulations available in the literature. Chapter III summarizes the shortcomings of the previous research work and outlines the objectives for the current study. Chapter IV discusses the numerical methodology adopted for this study, covering topics such as geometry creation, meshing, physics selection, post-processing in detail. Chapter V shows all the results for the study including grid independence results and analysis, followed by validation of the numerical methodology, and results discussion related to different superhydrophobic surfaces configurations. Chapter VI includes concluding remarks and along with it highlights potential research activities for future work.



## CHAPTER II

### LITERATURE REVIEW

This chapter presents an overview of research activities carried out in recent years, whose objectives were to reduce pressure drop while enhancing thermal transport in micro- and minichannels. Brief literature has been provided which discusses the use of bionics and microchannel heat sinks with porous fins to reduce the pressure drop in heat transfer devices. This is followed by a literature review of superhydrophobic surfaces in the laminar and turbulent flow regimes in which significant drag reduction and thermal enhancement have been achieved.

#### **2.1 Low drag surfaces with microscale modifications**

Over the last decade, different techniques have been explored to achieve reduction in pressure drop in microchannels. One such approach is the use of bionic surfaces. Studies have shown that evolution has led to the development of unsmoothed surfaces on aquatic animals and winged insects which are known to have good drag reduction capabilities. Cui *et al.* [7] studied the effects of four different types of bionic grooved surfaces in microchannel and their corresponding pressure reduction. The four bionic surfaces are shown in Figure 2.

The ridge-shaped grooves were found to have the highest pressure drop followed by V-shaped, placoid-shaped, and riblet-shaped grooves. The generation of vortices formed inside the grooves led to a decrease in shear stress between the fluid and the

surface. Thus, the reduction in pressure drop was attributed to the vortex generation which also led to lower effective contact area between the fluid and the surface.

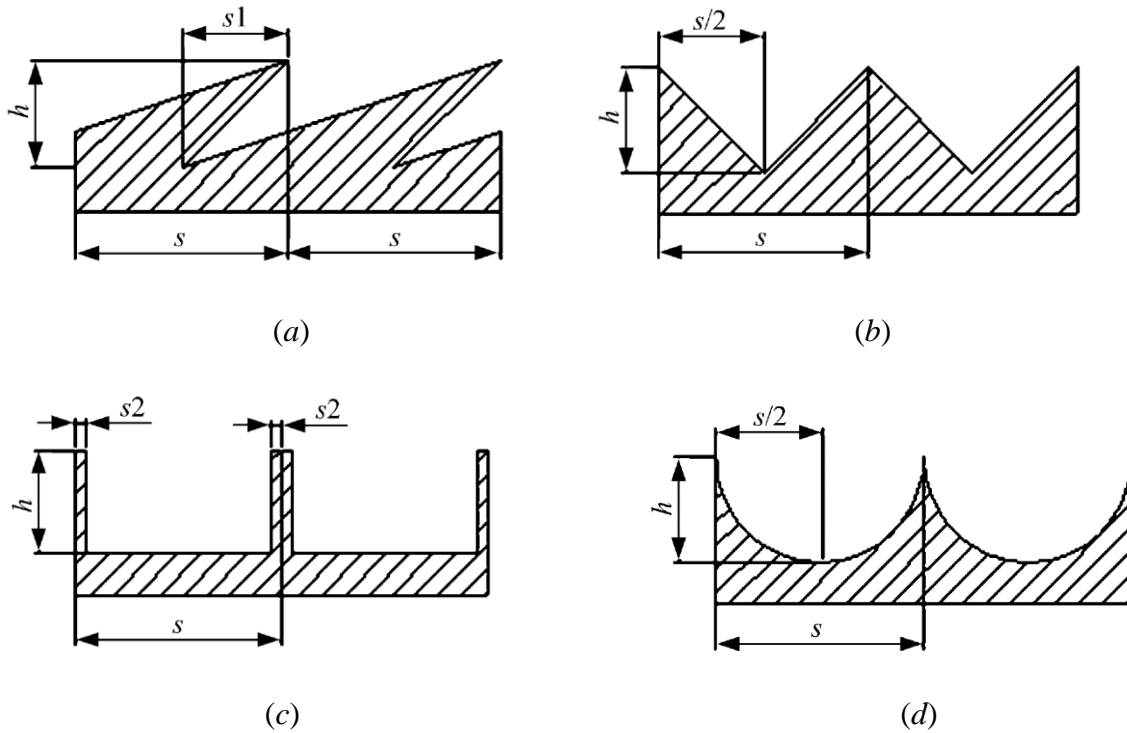


Figure 2. Bionic surfaces - (a) placoid-shaped grooves, (b) V-shaped grooves, (c) riblet-shaped grooves and (d) ridge-shaped grooves (Reprinted from [7])

Wavy microchannel heat sinks were found to be effective in removal of heat from micro-electronic systems. However, the decrease in hydraulic diameter of the components leads to an increase in pressure drop for such heat sinks. Thus, to reduce the pressure drop, Gui *et al.* [8] proposed a new design of microchannel heat sinks using porous fins. The results indicated that the wavy microchannel heat sinks with porous fins not only reduced the pressure drop but also led to a reduction in thermal resistance. The reduction in

pressure drop was attributed to the permeation effect and the slip behavior of the coolant at the interface. In comparison with the superhydrophobic surfaces described later in this chapter, these methods were found to produce lesser reduction in pressure drop.

Before exploring the research work associated with superhydrophobic surfaces, it is important to understand what constitutes a superhydrophobic surface. Superhydrophobic surfaces can be found in nature. For instance, leaves of *Nelumbo nucifera* (lotus) are seen to exhibit a phenomenon known as the lotus effect. The presence of this phenomenon causes the water droplets, which fall on such leaves to bead on the surface and roll off. The droplets, as they roll off the leaf, collect all the dirt present on the leaf and thus are often referred to as self-cleaning leaves. The phenomenon is caused by the combined effect of hierarchical double structure present on the leaf surface and the waxes which are intrinsically hydrophobic in nature. Depending upon the surface texture, the liquid droplet on the surface can be represented by two different models: Cassie-Baxter and Wenzel state.



Figure 3. Lotus leaf with water droplet (Reprinted from [9])

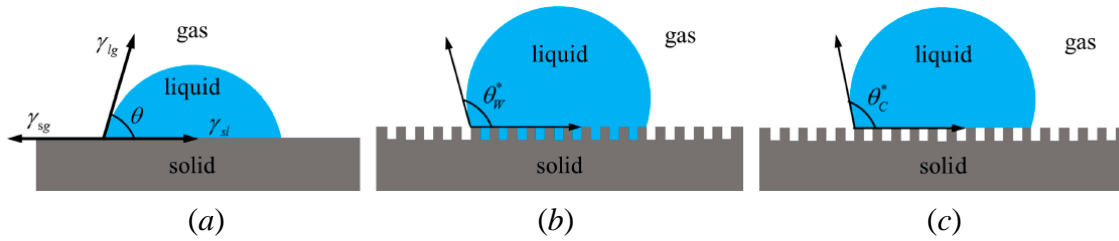


Figure 4. Water droplet on (a) smooth surface, (b) superhydrophobic surface with Wenzel state, (c) superhydrophobic surface with Cassie-Baxter state (Reprinted from [10])

On a normal smooth hydrophilic surface, the water droplet spreads out evenly. The contact angle, which the droplet makes with the surface, is less than  $90^\circ$  for such smooth hydrophilic surfaces as shown in Figure 4(a). For a rough surface, the water fills in the gaps present in between the surface roughness. Such a surface is said to be in Wenzel state and is referred to as a wetted surface as shown in Figure 4(b). In the Cassie-Baxter state, the superhydrophobic surface, which combines the effect of surface roughness and hydrophobicity causes the water to settle on top of the surface roughness elements with the trapping of air/gas in between the roughness structures. Figure 4(c) shows the Cassie-Baxter state with the contact angle greater than  $90^\circ$ . The lotus leaves have been found to reach a contact angle of  $170^\circ$ , which indicates 0.6% of the droplet is in contact with the surface.

Before exploring the drag-reduction and heat transfer enhancement capabilities of superhydrophobic surfaces (SHS), it is imperative to understand the physical representation of such surfaces. Figure 5 shows the SHS in consideration. The surface has roughness elements present in the form of micro-posts or ridges arranged in a regular

pattern. Chemical treatments are carried out to impart hydrophobicity on the surface. If the feature spacing is close enough and the pressure applied is sufficiently low, then the fluid flowing over the surface will not penetrate or fall into the cavities formed by the ridges/posts. In such cases, water is found to have contact only with the posts and ridges of the surface as shown in Figure 5.

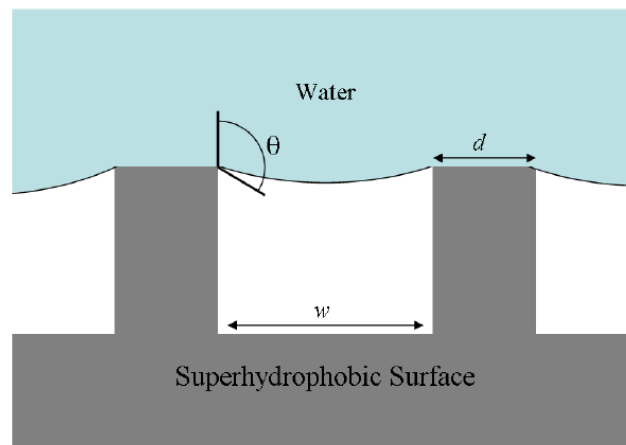


Figure 5. Schematic representing SHS interaction with water (Reprinted from [11])

The repulsion of water by the superhydrophobic surfaces causes the cavities to entrap air inside them. Thus, this leads to the formation of two types of interfaces. The water and rib interface is often referred to as a non-slip surface, and the water-air interface commonly referred to as shear free (slip) interface. The drag reduction is achieved due to the slip, which takes place along the shear free air-water interface supported between the peaks of the surface.

While most of the experimental work related to superhydrophobic surfaces takes into account contact angle due to the presence of microscale cavities, numerical investigations in most cases models the air-water interface as a continuous flat surface.

The following sections present information about superhydrophobic surfaces in laminar and turbulent flow regimes.

## **2.2 Superhydrophobic Surface (SHS) in laminar flow regime**

Ou and Rothstein [12,13] were among the first to experimentally investigate flow through a microchannel with superhydrophobic surfaces in the laminar flow regime. The experiments demonstrated the effect of different microchannel geometries and superhydrophobic surfaces on pressure drop for a range of flow rates in a microchannel. The use of microparticle image velocimetry enabled the measurement of velocity profile by resolving the flow below the length scale of the superhydrophobic surface (SHS) features. The experiments demonstrated a pressure drop reduction of 40% and a slip length of more than 40 microns for some SHS designs.

Slip flows in superhydrophobic microchannels aligned with spanwise grooves were experimentally explored by Byun *et al.* [14]. The groove structure led to the formation of the meniscus in the cavity supported between two non-slip surfaces. Furthermore, it was observed that the increase in the pitch-to-wide ratio of the groove structure led to increased penetration of the meniscus in the air cavities. Figure 6 shows the wetting transition for different pitch ratios in a superhydrophobic channel.

Numerous numerical simulation approaches have been proposed to better understand the hydrophobic surface in the laminar flow regime. Maynes *et al.* [15] considered the liquid-vapor interface to be flat to explore two different conditions related to the cavity region. The first one assumed that flow of liquid over the cavity is shear

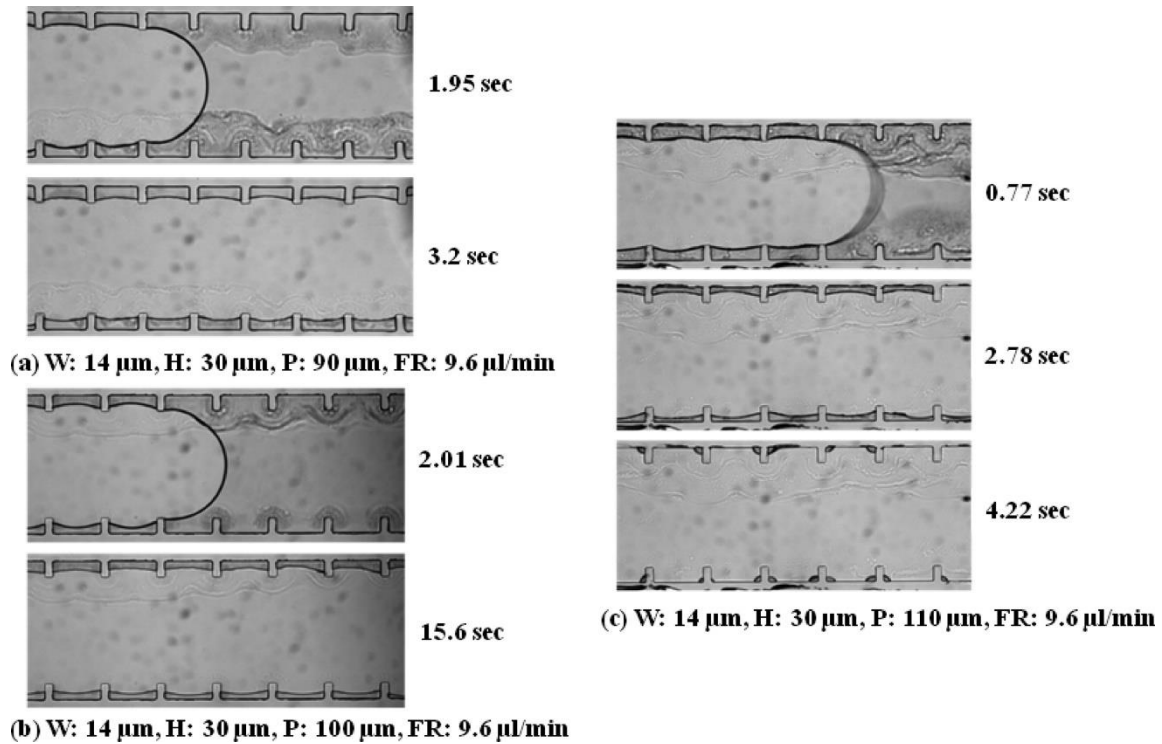


Figure 6. Meniscus formation over the micro structured surface with varying pitch values (Reprinted from [14])

free. For the second condition, the microchannel fluid velocity was matched to the vapor fluid velocity, as well as the shear stress value at the liquid-gas interface correspondingly. Significant reductions in frictional pressure drop were achieved in comparison to smooth channel flow. In such cases, cavity-to-rib width, the hydraulic diameter of the cavity, and the Reynolds number were observed to affect frictional resistance. Furthermore, it was observed that the impact of the vapor cavity on frictional resistance was minimal if the vapor cavity depth was more than 25% of the width. The usefulness of such surfaces was limited by many factors, one of which was higher pressure values. Higher pressure values caused the external fluid to penetrate the cavities and diminish the hydrophobic effect of the cavities. Maynes *et al.* [15] proposed an equation given, which provided an estimate

of the pressure differential between the liquid and vapor space causing the fluid to penetrate the cavities, as follows:

$$\Delta P_i = \frac{2\sigma\cos\beta}{l_s} \quad (1)$$

where  $\sigma$ ,  $\beta$ ,  $l_s$ , are surface tension of the liquid, liquid-vapor-solid contact angle, length of cavity respectively. Attempts have been made to model the liquid-gas interface to capture the circulation effects in the cavities. Gaddam *et al.* [16] employed the volume of fluid model for streamwise aligned grooves as it was seen that the assumption of the flat interface at the liquid-vapor interface overpredicted the effective slip length. Simulations were carried out for different ridge structures to investigate the effects on pressure drop reduction. From Figure 7, it is evident that the lotus-like structures had the maximum impact on the reduction of frictional resistance.

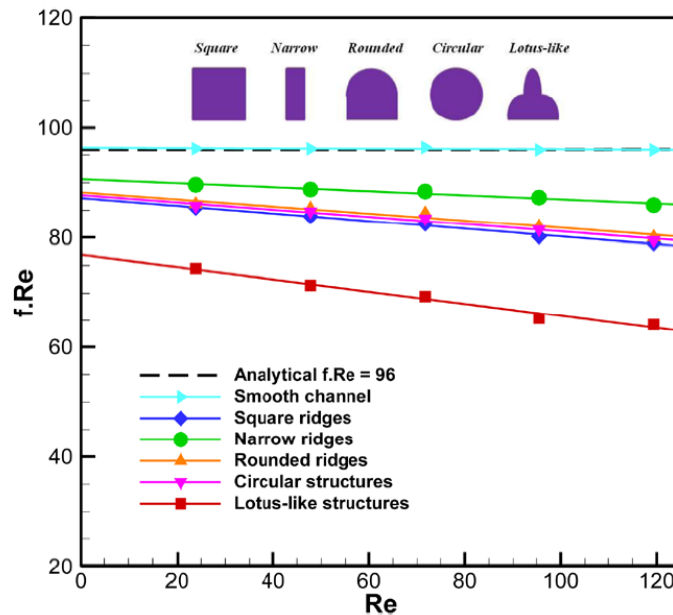


Figure 7. Variation of product of friction factor and Reynolds number with respect to Reynolds number for different ridge geometries (Reprinted from [16])



Most of the superhydrophobic surfaces research has focused on understanding their effect on drag reduction; however, the effects of using SHS on thermal performance enhancement effects is quite limited. Li and Alvarado [17] investigated numerically the effect of varying fractal ratio and slip length ratio on pressure drop and heat transfer enhancement for transversely patterned superhydrophobic surfaces in the laminar flow regime. The fractal ratio (FR) was varied between 0.7 and 1, whereas the length ratio (LR) was varied from 1 to 12, and the corresponding effects on Nusselt number, friction factor, and performance evaluation criteria (PEC) were studied for two Reynolds numbers. The simulation approach proposed first included running a simulation with air cavities present to capture the shear stress value at the interface. Once this was done, the shear stress profile values were used as boundary conditions in the regions where superhydrophobic surfaces were present. The authors concluded that the transverse ribs enhanced heat transfer and reduced pressure drop significantly at lower Reynolds number. Furthermore, the study revealed that increasing Reynolds number and the length of the hydrophilic surface has a significant effect on thermal performance. The influence of Peclet number and cavity fraction on Nusselt number was analyzed by Maynes *et al.* [18] for parallel plate configuration of transversely aligned rib and cavity modules with a constant heat flux on the walls. The increase in Peclet number and the cavity fraction led to an increase in Nusselt number over the rib region. However, the rib and cavity averaged Nusselt number decreased because of the reduction of thermal transport over the superhydrophobic surface. From the application-based point of view, Cheng *et al.* [19] explored the possibility of the use of superhydrophobic surfaces for electronic cooling purposes. The

objective of their research was to systematically investigate the effect of different superhydrophobic geometries on thermal and frictional performance in a laminar flow regime. Figure 8 shows the different geometries considered in their study. The longitudinal and transverse grooves produced the lowest and highest values for the product of friction factor and Reynolds number, respectively. In Cheng *et al.* [19], the square posts and square holes were considered to be a combination of the longitudinal and transverse grooves. The thermal performance of such configurations was found to be in between the longitudinal and transverse groove cases. For Reynolds number less than 20, the product of friction factor and Reynolds number was found to be constant as the flow was regarded as viscous Stokes's flow and had an insignificant inertial effect.

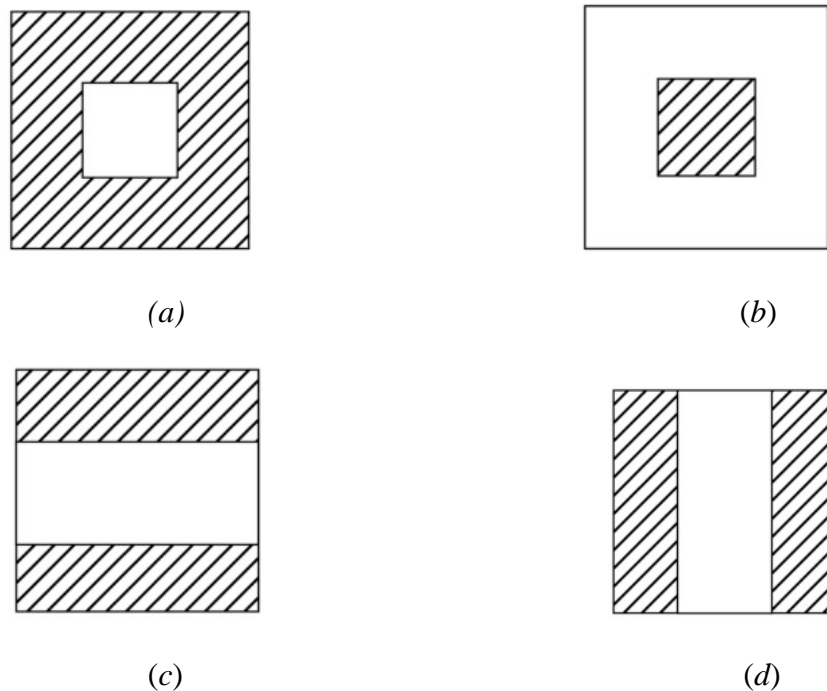


Figure 8. Different micro surface geometries - (a) square holes, (b) square posts, (c) longitudinal grooves and (d) transverse grooves (Reprinted from [19])

With the increase in Reynolds number above 20, the product of friction factor and Reynolds number was found to increase for transverse grooves, square posts, and holes whereas it remained constant for longitudinal grooves. The increase in shear-free fraction led to a decrease in the Nusselt number for all the four geometries considered, whereas the goodness factor representing the combined effect of the frictional and thermal performance was found to increase. The increase in Reynolds number led to an increase in the Nusselt number for the transverse groove, square posts, and square hole microchannel configurations.

### **2.3 Superhydrophobic Surfaces (SHS) in turbulent flow regime**

#### ***Experimental Studies***

Watanabe *et al.* [20] carried out an experimental investigation of Newtonian fluids in a circular pipe for laminar and turbulent flow regimes using a highly repellent wall. A mixture of tap water and aqueous solution was used as a fluid, and the pressure drop, and velocity profile were measured using a pressure transducer and hot-film anemometer. They reported that near the transition from laminar to a turbulent flow regime, the friction factor curve was found to increase at a lower rate in the water repellent walls as compared with smooth walls. While Watanabe *et al.* [20] predicted drag reduction in laminar and turbulent flow regimes, Zhao *et al.* [21], through their experimental setup, concluded that the transition into turbulent flow regime led to decreased drag reduction effects. The increase in friction was attributed to the increase in the disturbance of the flow near the wall in the turbulent flow regime.

Considering the effect of SHS in the turbulent channel flow, Daniello *et al.* [22] designed a setup consisting of streamwise aligned superhydrophobic surfaces in a channel. Drag reduction close to 50% was achieved at a higher Reynolds number. At a fixed Reynolds number, the increase in feature spacing was found to improve drag reduction. Woolford *et al.* [23] also studied the effects of longitudinal and transverse rib-cavity orientation for turbulent channel flows. Figure 9 shows the test section used in their research study. The channel aspect ratio considered for the experiments was set at 8.7. Velocity field measurements were carried out using the particle imaging velocimetry (PIV). The longitudinal rib-cavity configuration of the superhydrophobic surface was found to produce lower turbulence, lower streamwise turbulence intensity which resulted in a 10% reduction in the wall friction factor. The transverse configuration led to a 6.5% increase in the wall friction factor.

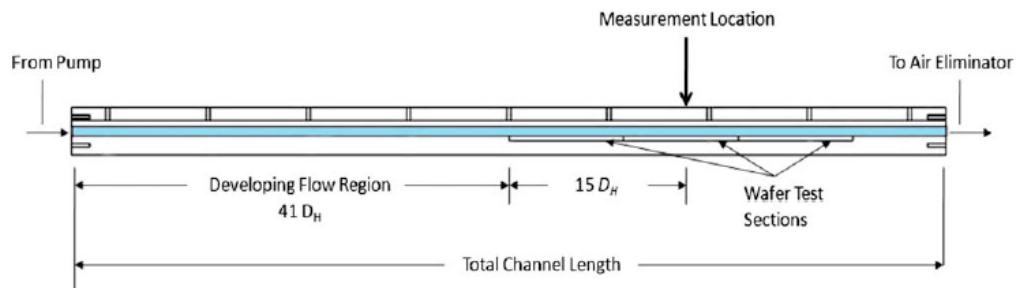


Figure 9. Test section used by Woolford *et al.* [23] (Reprinted from [23])

While most of the research related to superhydrophobic surfaces were carried out for internal flows, Aljallis *et al.* [24] researched their effects in the external flow cases. The study focused on hydrodynamic drag reduction using SHS on flat plates for a wide range of flow velocities covering the transitional and turbulent flow regimes. The

experiments were performed using the tank towing systems, while the surface hydrophobicity was achieved by spraying hydrophobic nanoparticles. It was concluded through the experiments that drag reduction was enhanced with the increase in contact angle of the SHS. Also, a low contact angle hysteresis was deemed essential for effective drag reduction, otherwise the increase in wall shear stress in the turbulent boundary layer led to the removal of air bubbles from the surface.

Unstructured surfaces or randomly textured SHS are a viable option for practical application because of their ease of manufacturing. Bidkar *et al.* [25] developed a random textured SHS using thermal spraying to explore their drag reduction capabilities. The results indicate that the Cassie state formation and the hydrophobicity alone cannot ascertain drag reduction on such surfaces. The surface roughness was seen to have a very marked effect on drag reduction. The surface roughness values smaller than the viscous sublayer thickness ensured a significant drag reduction. Zhang *et al.* [26] experimented with the micro-textured fabricated superhydrophobic surface for  $Re_\theta$  of 810, 990 and 1200. Drag reduction of 10%, 20% and 24% were observed for Re of 810, 990 and 1200, respectively. The reduction in drag was attributed to the slip on the interface and the resulting modification of turbulent structures, which played a significant role at higher Reynolds numbers. Also, the weakening of the vortexes generated by SHS led to the upward shifting of the maximum swirling strength position, which also contributed to the reduction of drag.

Another key common observation seen in multiple studies has been the removal of gas pockets at high Reynolds number, which led to an increase in the drag on the surface

(Aljallis *et al.* [24]). Long-term degradation of drag reduction was studied by Balasubramanian *et al.* [27]. For the flat plate and ellipsoidal configurations, it was seen that the drag reduction approached a limiting value over time. This degradation in drag reduction was caused by the removal of gas pockets on the configured surface. However, when the surface was dried, it led to maximum drag reduction due to the removal of gas pockets. To tackle the issue of removal of gas pockets at higher Reynolds number, continuous air injection over the hydrophobic surface was proposed and tested experimentally by Du *et al.* [28]. This ensured a continuous air layer over the hydrophobic surface. This modification led to a 20% drag reduction when compared to smooth turbulent channel flow. Rosenberg *et al.* [29] compared the drag reduction capabilities of air-impregnated (superhydrophobic surfaces) and liquid-impregnated (liquid-infused surfaces) in the turbulent flow regime for a Taylor-Couette flow. By using a liquid infused surface, the shortcomings of superhydrophobic surfaces could be suppressed including the incipience of high hydrodynamic pressure and its corresponding fluctuations. The liquid-infused surfaces were found to perform even better than air-infused surfaces producing a drag reduction of 14% compared to 10% achieved by the air-infused surfaces. It was also observed that the ratio between the viscosity of water and the infused liquid must be the same order of magnitude to produce a tangible drag reduction effect.

### ***Numerical Studies***

Numerically simulating turbulent flow in superhydrophobic surfaces is a very difficult task. Thus, different types of simplification have been used to accurately simulate

turbulent flow numerically. The two common ways used to simulate turbulent in systems with SHS features are as follows:

i) Texture-Averaged Slip Length Boundary Condition

This approach was used by early researchers who used Direct Numerical Simulation (DNS) [30,31]. In this approach, an averaged slip length is specified at the wall. The main benefit of this approach is a significant reduction in the spatial resolution required to capture the surface textures. This approach was found to work best when the size of the texture was small compared to the turbulent scales.

ii) Texture Resolving Simulations

In this approach, the spatial resolution of the texture was modeled, and different boundary conditions were provided depending on the wall conditions. In this approach, the liquid-gas pocket interface was set as a slip boundary condition whereas the liquid-solid surface was set as a non-slip boundary condition. In this approach, the use of free slip boundary conditions neglects the flow dynamics inside the gas pockets.

DNS simulations are routinely used for solving a wide range of turbulence flow problems in minichannel systems. In these simulation techniques, the whole domain is resolved to Kolmogorov's scale. In such simulations, the whole range of spatial and temporal scales of turbulence are solved numerically. The earliest DNS on a turbulent channel flow was carried out by Kim *et al.* [30]. They solved the unsteady Navier Stokes

equation for Reynolds Number of 3300 on a four-million-nodes grid. The results were compared with experimental data available for low Reynolds numbers.

Most of the turbulent statistics showed a good amount of agreement with the experimental data. The same authors simulated fluid flow through a superhydrophobic channel using DNS [31]. The authors studied the application of slip boundary conditions in the streamwise and the spanwise directions. The authors concluded that the application of slip in the streamwise direction led to a reduction in friction drag, whereas the spanwise application led to an increase in drag. Another important finding was that the slip length needed to achieve drag reduction when using superhydrophobic surfaces should be greater than the nanometer scale level.

Min *et al.* [31] used slip length values to model the superhydrophobic surfaces. On the other hand, Martell *et al.* [32] resolved the surface textures of different surface geometries like square posts and ridges in their DNS simulations directly. Figure 10 shows the two microfeatures considered by Martell *et al.* [32] in their research.

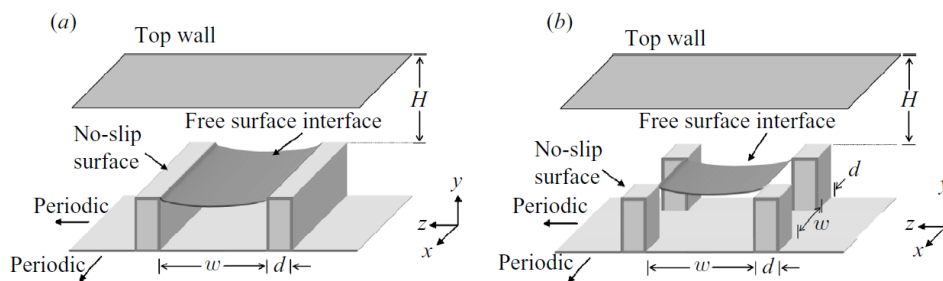


Figure 10. (a) Ridge and (b) square post surface structures considered by Martell *et al.* [32] (Reprinted from [32])

The authors [32] considered the top surface of the microfeatures to be a non-slip boundary condition. The liquid-air interface suspended between the microfeatures was assumed to



be flat and a no-shear boundary condition was set. The objective of the research was to investigate the effect of feature spacing on the overall drag reduction for two different microfeatures. The velocity profiles obtained through simulations indicated that the mean velocity and slip velocities increased with an increase in the spacing ratio. Maximum slip velocity of 65% and 75% of the bulk velocity was achieved for the ridge case and square-post case, respectively. A maximum drag reduction of 40% was achieved using the micro-posts geometry.

Seo *et al.* [33] developed a model, which could predict the kinematics of surface flows associated with superhydrophobic surfaces by incorporating the Stokes flow slip length model. Another feature of their research was that it was simulated over a wide range of texture sizes varying from  $L^+$  of 6 to  $L^+$  of 310 with the solid fractions,  $\phi_s$  varying from 1/9 to 1/64. Also, the authors provided a correlation between the shear over the surface and the slip velocity for the streamwise and spanwise directions. They concluded that for small  $L^+$  values, a single correlation could be used to account for properties in both the directions, which agreed well with Stokes's flow models. For large  $L^+$ , the slip and shear were uncorrelated and thus needed a different correlation to be developed to account for the same conditions. The developed correlation for large  $L^+$  values showed an inverse square root dependence on the solid fraction and a cubic dependence of slip length based on the texture size.

Fairhall and Garcia-Mayoral [34] investigated the slip length model from the spectral perspective and considered different boundary conditions because of the different length scales. The simulations used square posts in the collocated arrangement as

microfeature geometry with a fixed solid fraction of 1/9 while varying the  $L^+$  value from 12 - 47. The range of  $L^+$  value was chosen in such a way that the slip length of the smallest texture size was found to be in the homogeneous region, whereas the largest texture size was in the region where the correlation between shear and velocity was not satisfied. They deduced that the loss of correlation for higher texture size did not affect the apparent slip experienced by length scales greater than the texture size. They proposed that the loss of correlation was attributed to the scattering of the induced energy because of the interaction between the texture-induced flow and overlying mean turbulence. The research carried out by Mani *et al.* [33] and Fairhall and Garcia-Mayoral [34] considered the combined effect of slip and surface texture on the turbulence while the work carried out by Abderrahaman-Elena *et al.* [35] considered their individual effects on turbulence in superhydrophobic surfaces. Filtering the effects of texture-induced flow, Abderrahaman-Elena *et al.* [35] were able to validate the effects of the surface boundary conditions. The surface slip was found not to alter the turbulence in the overlying flow.

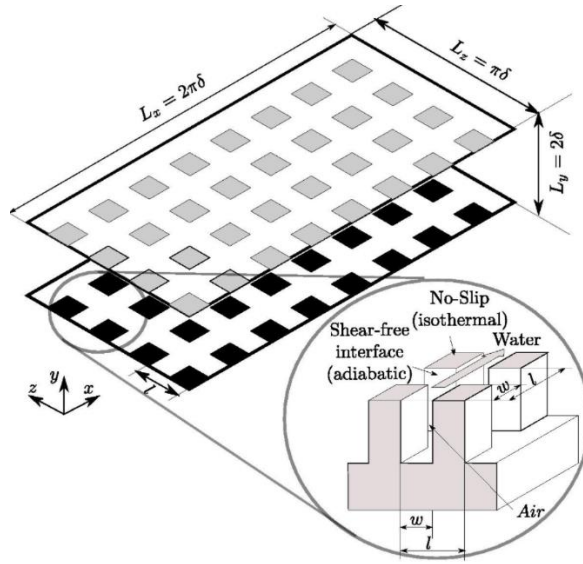
While most of the researchers focused on the turbulent flow in a channel with superhydrophobic surfaces, Costantini *et al.* [36] studied the superhydrophobic surfaces in turbulent pipe flow for high Reynolds number. It was observed that the increase in the periodic length of the pipe led to an increase in the mean velocity profile near the walls. Also, the increase in periodic length led to a decrease in the mass flow rate due to modifications in the turbulent structures near the wall. The impact of mean velocity was more pronounced than modifications in the turbulent structures, thus increasing the mass flow rate and increasing the drag reduction effect. The decrease in gas or cavity fraction

while keeping the periodic length constant led to a reduction in the mean slip velocity. In the study, the slip and no-slip arrangement led to the generation of vortical structures whose closeness depended on the widths of the groove.

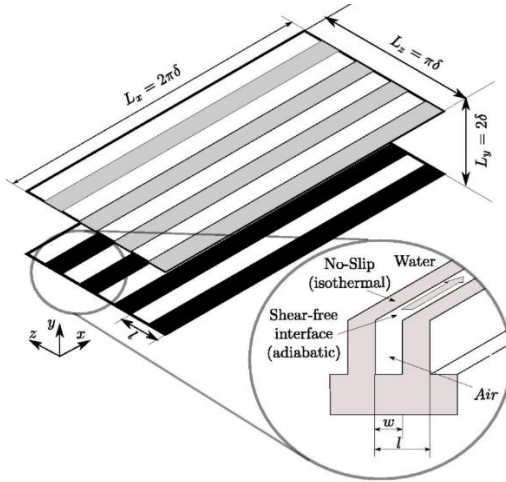
The effect of SHS along with thermal forcing was considered by Fuaad *et al.* [37]. The simulations were performed for a fixed frictional Reynolds number of 180 and Richardson number of 15 over a transversely aligned ridge surface. It was observed that the drag reduction was enhanced by increasing the width to depth ratio for the ridges. A skin friction drag reduction in the range of 10-22% was achieved based on the different texture sizes. Finally, the effect of heating on the net-drag reduction was investigated. The results suggested that the heating led to the mitigation of drag reduction by 6-7%.

### ***Thermal Performance Studies***

SHS effect on forced convection was studied by Fuaad and Prakash [38]. The study focused on two different surface structures: square posts and streamwise aligned ridges. The main objective of the research was to understand the influence of varying feature width and surface textures on the thermal transport mechanisms. Figure 11 shows the two different types of surface textures considered with the dimensions of the control volume. In their research, square posts and ridges were maintained at constant temperature and the gas pockets were assumed to be adiabatic. Slip effects were found to be more pronounced for square posts texture when compared to the ridges. From the thermal performance standpoint, the Nusselt number decreased for the SHS in comparison to the non-slip case because of the adiabatic behavior of the air pockets. A downward shift in temperature distribution over the SHS was noted in comparison with the no-slip channel case.



(a)



(b)

Figure 11. Surface texture: (a) Square Posts (b) Streamwise ridge (Reprinted from [38])

Comparison of heat transfer between the superhydrophobic surface and liquid-infused surfaces (LIS) for turbulent microchannel flow was studied by Leonardi *et al.* [39]. The simulations were performed for two different surface geometries: longitudinal and horizontal arrangement of ridges, respectively. The effects of interface dynamics and fluid

properties on drag reduction and heat transfer were considered in their study. For the interface dynamics, two different conditions were simulated: (a) infinite surface tension between the two fluids forming the interface (flat interface), (b) a constant value of surface tension, which enables dynamic movement of the interface present between the fluids in contact. For the infinite surface tension case, the drag reduction more than 20% was obtained for the case of longitudinal ridges. The drag reduction was found to be more for SHS compared to LIS. The implementation of a dynamic interface led to a significant reduction in drag reduction. From the heat transfer standpoint, the flat interface led to a reduction in the heat transfer by 5-10%. Furthermore, a parametric study considering fluid properties showed that a decrease in thermal diffusivity of the fluid led to a decrease in the heat transfer in the cavities. Also, the low thermal conductivity of air resulted in lower heat transfer in the SHS cases than in LIS ones. Moreover, the thermal slip length was found to be more than the streamwise slip length for the transversal case. On the other hand, streamwise slip length was found to be more than the thermal slip length in the longitudinal case. The streamwise ridges, which induced controlled fluctuations of the interface damping and wall-velocity fluxes led to drag reduction and heat transfer enhancement. The research [39] concluded that using LIS and SHS in different engineering applications could lead to drag reduction (DR) and heat transfer enhancement by adjusting the shape of the texture and properties of the fluid present in the cavities.

## CHAPTER III

### RESEARCH GAPS IDENTIFIED AND OBJECTIVES OF THE STUDY

#### **3.1 Research Gaps Identified**

There have been a significant number of experimental and numerical studies reported in the literature exploring the drag reduction effects of patterned superhydrophobic surfaces in the laminar and turbulent flow regimes. However, limited research publications are available, which focus on the thermal performance effect of SHS. Also, most of the research publications have focused their work mostly on two surface textures: streamwise aligned ridges and square posts. Moreover, the transversely aligned ridges have not been explored in-depth for the turbulent flow regime. While a few authors have focused on understanding the effects of the change in non-slip to slip ratio, others have focused on varying the width of such bands to explore drag reduction using SHS. However, the combined effects of both the variations have been rarely studied. Faaud and Prakash[38] are among the few authors who considered the thermal performance effect of SHS in turbulent flow regimes. However, their research focused on the streamwise alignment of ridges. The literature review also revealed that the effect of Reynolds number on pressure drop and thermal performance using SHS is seldomly considered. These factors should be considered in the simulations of fluid flow in minichannels under turbulent flow conditions.

### **3.2 Objectives of Study**

From the literature review, it is clear that most of the authors performed Direct Numerical Simulations (DNS) to numerically simulate flow over superhydrophobic surfaces. However, these simulations are computationally expensive and complex to set up. Thus, one of the main objectives of this research was to establish a simplified numerical model to simulate superhydrophobic surfaces. Also, one of the objectives was to validate the scheme using available data from the literature.

Another objective of this study was to investigate the thermal performance and pressure drop reduction effects of transversely patterned superhydrophobic surfaces in a turbulent flow regime. Furthermore, the effect of non-slip to slip ratio and width of the non-slip bands on the local and average Nusselt Number and the velocity profiles should be considered. Along with that, the effect of non-slip to slip ratio and width on non-slip bands on boundary layer was also studied.

Also, the study focuses on understanding the effect of Reynolds number on the thermal and pressure drop reduction capabilities of SHS, by comparing the results of the laminar flow and turbulent flow regime simulations.

## CHAPTER IV

### NUMERICAL METHODOLOGY

This chapter presents the numerical approach used to meet the objectives of the study. The physical domain, as well as the numerical scheme used in the study, are discussed in detail below.

Designing a physical experiment to understand the effects of SHS in turbulent and laminar flow can be an expensive and time-consuming task. It involves the development of superhydrophobic surfaces, which requires the use of lithography and surface modification mechanisms, among others. Also, it requires the use of micro-scale particle image velocimetry for flow field measurements. Sophisticated instruments need to be used to analyze and visualize the physical phenomena, temperature, and pressure distribution for various cases. The shortcomings associated with these instruments are that they have physical limitations, which hinders the ability to fully understand the underlying physical phenomena. Although there is no alternative for physical experiments, carrying out these experiments without properly understanding the physics behind them, could lead to an incomplete understanding of the underlying physical mechanisms.

Numerical techniques, which are computational simulations of complex physical scenarios, can provide an alternate way to understand physics at a much cheaper cost. They involve solving algebraic equations, which are approximations of partial differential equations (PDEs) used to represent the physical phenomena. CFD is one of such numerical techniques used to simulate fluid flow and heat transfer behavior. It involves the use of



finite difference schemes to approximate PDEs like Navier-Stokes, continuity, and energy equations.

#### 4.1 Computational Fluid Dynamics Approach for SHS

Considering the complexity associated with experimentally visualizing the flow over SHS in a turbulent flow regime, a numerical simulation methodology was adopted in this study. Figure 12 shows the general methodology for a CFD analysis used in the study.

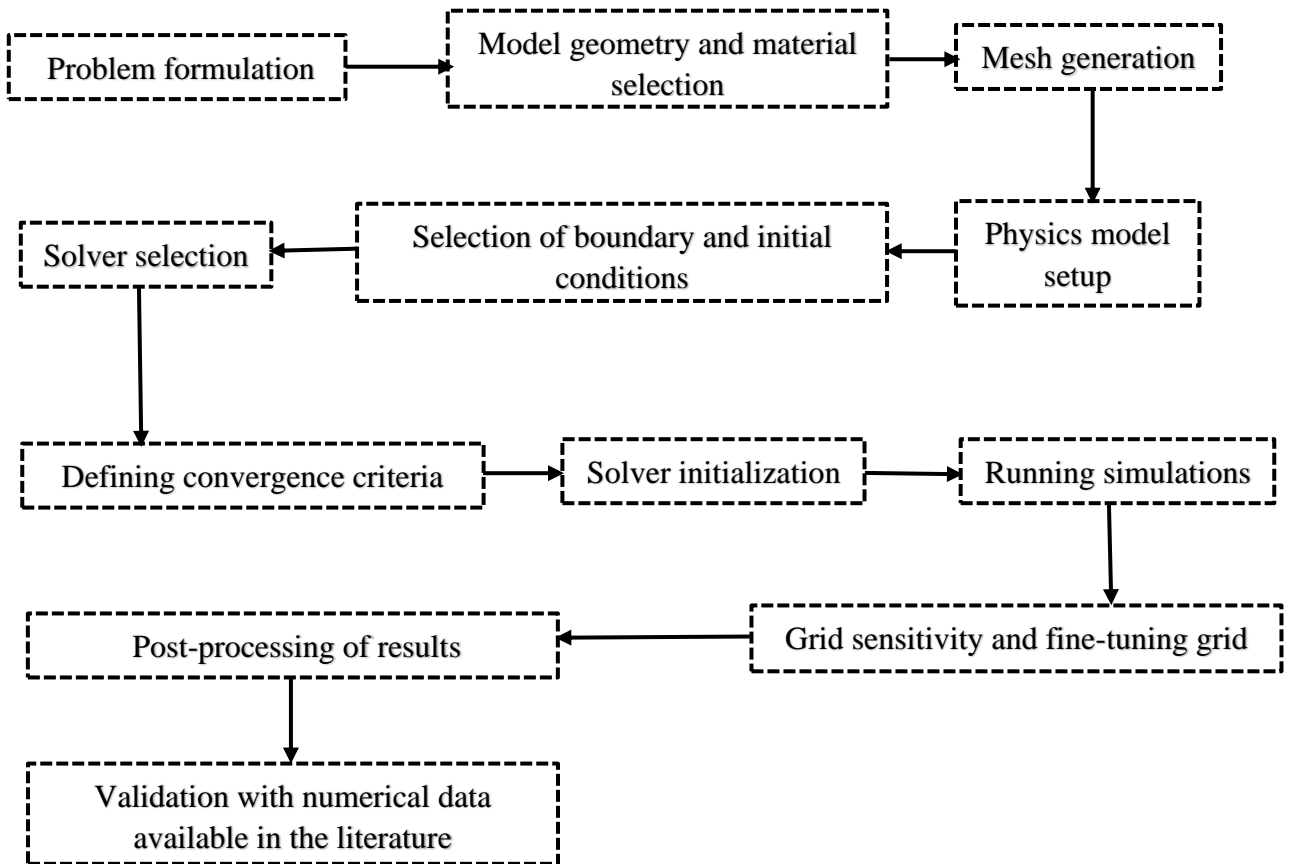


Figure 12. General methodology for a CFD analysis

A description of the key steps shown in Figure 12 are provided as follows:

### ***Problem Formulation***

As discussed in Chapter III, the objective of this study was to conduct numerical simulations to better understand the effects of superhydrophobic surfaces on thermal and pressure drop in turbulent flow regimes. A circular minichannel was considered to study the pressure drop and heat transfer performance under constant heat flux and turbulent flow conditions. Figure 13 shows the system considered in this study, where  $\delta$  represents the radius of the minichannel, and ‘ $a$ ’ and ‘ $b$ ’ represent the width of non-slip bands and slip bands, respectively.

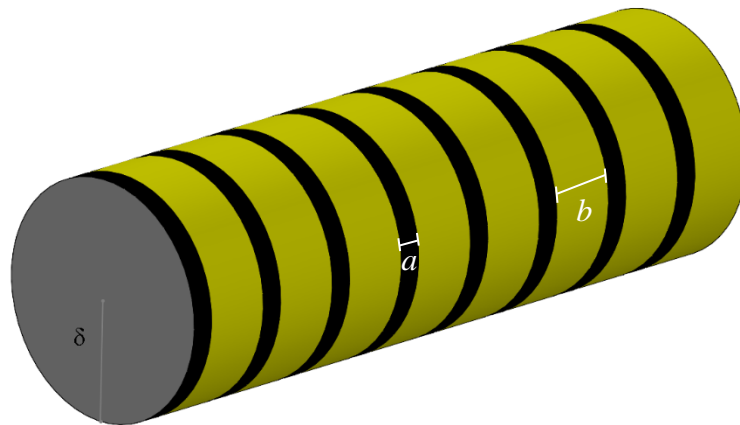


Figure 13. Simulated minichannel with SHS features

In the study, a Reynolds number of 5,600 was used in all the simulations. Furthermore, the effect of the non-slip to slip ratio and the width of non-slip bands on thermal

performance was assessed numerically. Table 1 shows the different cases considered in the study.

**Table 1. Numerically simulated non-slip/slip cases**

Non-slip/Slip ( $a/b$ ) ratio in minichannel	Width of the non-slip band, $a$ , in minichannel		
1:1	$0.2\delta$	$0.4\delta$	$0.8\delta$
1:3	$0.2\delta$	$0.4\delta$	$0.8\delta$

Note:  $\delta$  is the radius of the pipe

As Table 1 shows, two non-slip to slip ratios were considered in the study based on a previous study, which suggested specific ratios for enhanced thermal performance under laminar flow conditions [17].

### ***Numerical Generation of Physical Domain***

The first step associated with a CFD simulation was modeling the chosen geometry using computer-aided design (CAD) software. SOLIDWORKS software was considered for the modeling of the geometries. As part of the overall numerical approach, two different geometries were considered in this study. The first geometry was a rectangular minichannel used for the validation purpose of the turbulent flow numerical scheme, which is discussed later in this chapter. The second geometry considered in the study was a circular minichannel.

### ***Physical Domain used for validation purposes***

The dimensions of the rectangular minichannel were specified to be  $2\pi\delta$ ,  $\delta$  and  $\pi\delta$  in the x, y, and z-directions, respectively.  $\delta$  represents the half channel height, which was

assumed to be 16 mm. The x-direction represented the streamwise flow direction, y represented the spanwise, and z- represented the wall-normal direction. Figure 14 shows SOLIDWORKS geometry considered for validation.

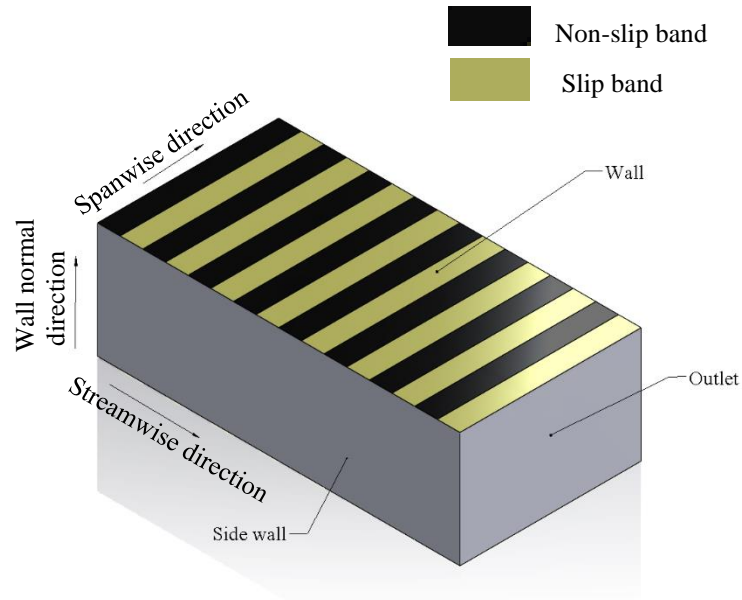


Figure 14. SOLIDWORKS model of the rectangular minichannel used for validation purposes

*Physical Domain used for circular minichannel*

For the circular minichannel, the domain was divided into two parts: a solid copper tube and a liquid water domain. The liquid domain was considered to be a pipe with a radius equal to 16 mm. The copper tube enclosed the water domain. The thickness of the copper tube was taken to be 250  $\mu\text{m}$ . The length of the whole domain was taken to be  $2\pi\delta$ , where  $\delta$  represented the radius of the pipe. Figure 15 shows the SOLIDWORKS model for this geometry.

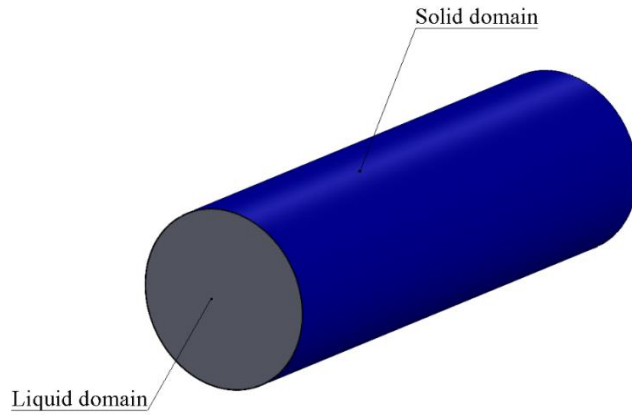




Figure 15. Isometric view of the SOLIDWORKS circular minichannel model

Table 2 shows the cut plane view of the geometries considered to explore the effects of non-slip and slip bands on heat transfer and pressure drop. While the non-slip regions are represented by black color, the slip regions are denoted by grey color in Table 2.

**Table 2. Numerically simulated non-slip/slip cases**

Non-Slip/Slip – 1:1	Non-Slip/Slip – 1:3
Non-slip width – $0.2\delta$	Non-slip width – $0.2\delta$
Non-slip width – $0.4\delta$	Non-slip width – $0.4\delta$

**Table 2. Continued**

<b>Non-Slip/Slip – 1:1</b>	<b>Non-Slip/Slip – 1:3</b>
	
Non-slip width – $0.8\delta$	Non-slip width – $0.8\delta$

***Fluid and Solid Material Selection***

Once the geometry was modeled the next step was to select the working fluid and solid material. Water was used as the working fluid for all the cases. With the variation in temperature, physical properties of water such as thermal conductivity, density, specific heat, and dynamic viscosity, were found to vary. Thus, to account for the effect of temperature on water properties, water was prescribed as per the International Association for the Properties of Water and Steam (IAPWS-IF97). The IAPWS-IF 97 model was pre-built in the StarCCM+ software [40]. Table 3 shows the properties of water at 300K.

**Table 3. Properties of water at 300K**

<b>Physical property</b>	<b>Value</b>
Thermal conductivity	0.6203 W/mK
Density	996.55 kg/m <sup>3</sup>
Specific heat	4.181 kJ/kgK
Dynamic viscosity	8.53 x 10 <sup>-4</sup> Pa-s

Copper was used as material for the minichannel. As with changes in temperature, the properties of copper were found to change. Thus, the specific heat, thermal conductivity, and density were specified as a 3<sup>rd</sup> order polynomial as a function of temperature and given as an input to StarCCM+ [40]. Table 4. shows the thermo-physical properties of copper at 300 K.

**Table 4. Properties of copper at 300K**

Physical property	Value
Thermal conductivity	398 W/mK
Density	8940 kg/m <sup>3</sup>
Specific heat	0.386 kJ/kgK

***Governing Equations for CFD Analysis***

The next step after fluid and solid material selection was to specify the governing equations. The governing equations are used to account for the fluid flow and thermal behavior under constant heat flux and turbulent flow conditions. These equations, which are in the form of partial differential equations, are converted to discrete algebraic equations using different discretization schemes. StarCCM+ uses the finite volume discretization approach. In this approach, the domain is subdivided into a small number of finite control volumes (cells). The integral form of the governing equations are solved and the variables are stored at the cell centroids of the control volume.

The governing equations for fluid flow and thermal transport are the momentum, continuity, and energy equations, as follows:

*Continuity Equation:*

This equation is based on the conservation of mass. The equation is as follows:

$$\frac{\partial \rho}{\partial t} + \nabla \cdot (\rho v) = 0 \quad (2)$$

*Momentum Equation:*

$$\frac{\partial}{\partial t} (\rho v) + \nabla \cdot (\rho v \otimes v) = -\nabla p + \nabla \cdot (\bar{\tau}) + f_b \quad (3)$$

where  $\otimes$  denotes the outer product,  $\bar{\tau}$  the stress tensor and  $f_b$  denotes the resultant of body forces per unit volume.

*Energy Equation:*

$$\rho \left[ \frac{\partial h}{\partial t} + \nabla \cdot (hv) \right] = -\frac{Dp}{Dt} + \nabla \cdot (k\nabla T) + (\bar{\tau} \cdot \nabla)v \quad (4)$$

where  $h$  represents total enthalpy,  $T$  is the temperature.

To predict the turbulent behavior using turbulence schemes, additional equations were considered in this study. Turbulent flows are characterized by unevenly fluctuating flow quantities. Direct numerical simulations (DNS), which aim at resolving small scales and high frequencies in time and space can lead to excessive computational costs. Instead, it is computationally less expensive to solve for averaged quantities and approximate the impact of fluctuating quantities. StarCCM+ turbulence models provide different approaches to model such flow structures. For that reason, the Reynolds-Averaged Navier-Stokes (RANS) turbulence model was used in the current study.



To achieve the equations solved by the RANS turbulence model, the variables of the instantaneous Navier-Stokes equations are decomposed into mean (ensemble-averaged or time-averaged) and fluctuating components as shown in equation 5:

$$\varphi = \bar{\varphi} + \varphi' \quad (5)$$

where  $\varphi$  denotes pressure, velocity components, or energy. Furthermore,  $\bar{\varphi}$  and  $\varphi'$  represent the mean component and fluctuating components, respectively. The equations for mean quantities are obtained by inserting the decomposed solution variables into the Navier-Stokes equations. The equations for mean quantities are identical to the original Navier-Stokes equations except that it includes an additional term, the Reynolds stress tensor, which is generated due to the time-averaging effect. Eddy viscosity and Reynolds stress transport model are the two ways available in StarCCM+ to model Reynolds stress tensor in terms of mean quantities. In this study, the k- $\omega$  SST turbulence model, which uses the eddy viscosity approach was used to simulate the flow over superhydrophobic surfaces in the turbulent flow regime. Further details pertaining to the turbulent scheme and solver selection are discussed later in this chapter.

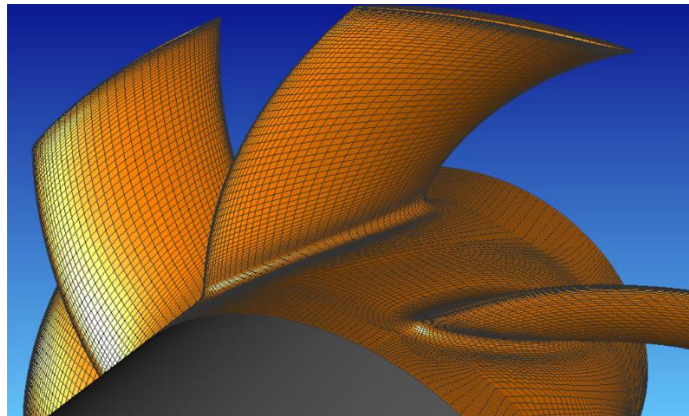
### ***Mesh Generation***

Grid or mesh generation is used to partition the geometry of interest into smaller elements. This process of dividing the geometry into smaller elements is called discretization of the domain. The discretization process generates small control volumes, on which the governing equations are solved. For the finite volume method, the StarCCM+ CFD solver computes values at the center of each mesh cell. Computational cost and the accuracy of the results depend on the grid size generated in each case. Thus, it is very

important to select the right meshing approach to capture all the details and represent the entire physical phenomena as accurately as possible.

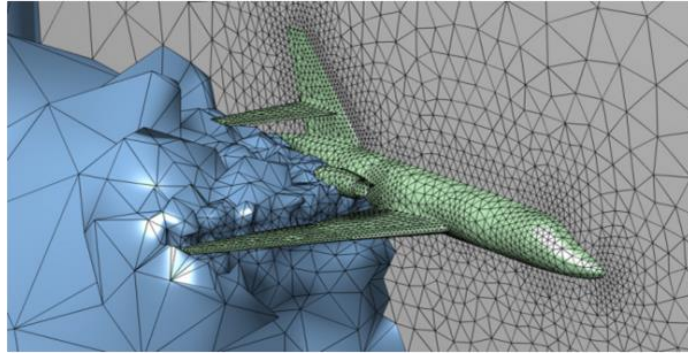
The mesh generated can be mainly classified into two types: structured mesh and unstructured meshes. Structured meshes comprise uniform elements that follow a uniform set pattern, whereas the unstructured mesh do not follow any pattern and are usually made up of tetrahedral or polyhedral elements. Figure 16 shows the structured and unstructured meshes, respectively.

Structured meshes are used for simple geometries, whereas unstructured meshes are used for complex geometries with sharp edges and acute angles. Among the advantages of structured mesh over unstructured mesh are better convergence and higher resolution. Considering the simplicity of the two geometries used in this study, structured meshes were used for both geometries.



(a)

Figure 16. (a) Structured Mesh [41]



(b)

Figure 16. (b) Unstructured mesh [0]

A directed meshing algorithm, which is available in StarCCM+ was used to generate meshes for both geometries. The directed meshing algorithm was used in the study because of its ability to generate high-quality structured meshes in the axial direction (flow direction). This algorithm involves the generation of an initial surface mesh, which is swept through the geometry volume onto a facing target surface.

The workflow associated with directed meshing is as follows:

- 1) Identification of the source and target surface

Identification of the source and the target surface is the first step before generating the surface mesh. The source surface refers to a face of the geometry on which an initial surface mesh is generated. The directed meshing then transfers the source mesh onto the target surface by sweeping it throughout the volume enclosed. Figure 17 shows the source and the target surface for a circular pipe.

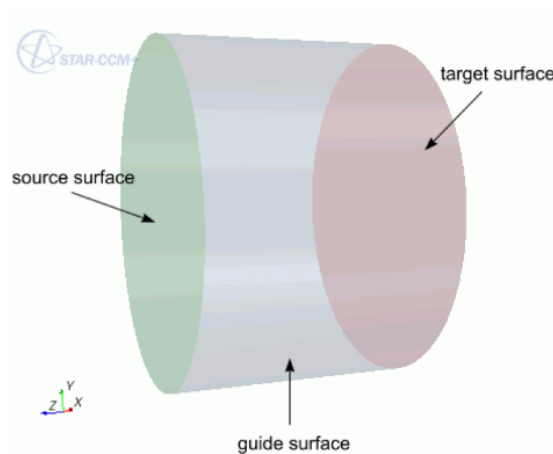


Figure 17. Circular pipe with source and target surfaces

## 2) Creating a source mesh

Source mesh is a 2D planar mesh generated on the selected source surface. The source mesh can be generated in multiple ways. The patch mesh generation approach was considered in this study. A patch is a four-sided shape that is made up of four vertices. Single or multiple patches can be generated on the surface mesh. For each patch, quadrilateral faces can be generated within each patch. Figure 18 shows the patches generated for a circular pipe.

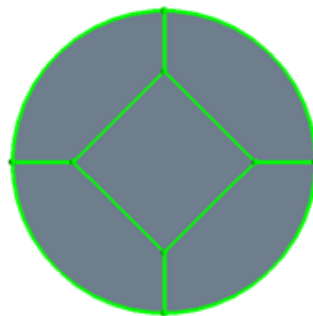


Figure 18. Circular pipe with patches

### 3) Generation of the volume mesh

Once the source mesh is generated, the next step is to generate a volume mesh, which is enclosed between the source and the target surface. This is done by specifying the number of layers to be generated in the volume. The number of layers here refers to the number of copies of the initial surface mesh to be created throughout the volume enclosed between the source and the target surface.

The following subsections discuss the mesh generation parameters used for both geometries.

#### *Mesh generation for numerical scheme validation: rectangular minichannel*

The mesh parameters implemented by Fuaad *et al.* [37] were used for this geometry. The authors considered a cartesian grid of 130 x 130 x 130 elements in the x, y, and z directions, respectively. The grid spacing was specified in terms of wall units. Wall units refer to the non-dimensional distance from the wall as indicated above, and is calculated as follows:

$$\Delta x^+ = \frac{\Delta x u_\tau}{\nu} \quad (6)$$

where  $\Delta x^+$  denotes the distance to the wall,  $u_\tau$  refers to friction velocity and  $\nu$  denotes the kinematic viscosity of the fluid. A uniform grid spacing of 8.7 and 4.35 wall units was specified for the streamwise and spanwise directions, respectively. For the wall-normal direction, a minimum spacing of 0.54 wall units was specified near the wall along with a hyperbolic function. As mentioned in the previous section, a directed meshing approach

was used for meshing the whole geometry. The inlet of the microchannel was considered as the source surface (red) and the outlet as the target surface (green) as shown in Figure 19.



Figure 19. Source and target specification for a rectangular channel

The next step was to generate the surface mesh on the source. A single patch was considered for this case. The patch lines with the same letter representation were divided into the same number of points. Figure 20 shows the source surface with the patch highlighted in green.

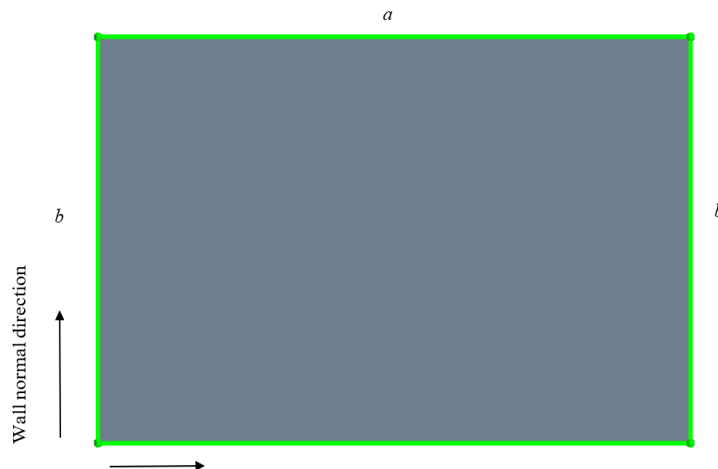


Figure 20. Source surface and patch for channel

To obtain a grid with 130 elements in the spanwise direction, the patch lines parallel to the spanwise direction were divided into 130 parts. For the wall-normal direction, a hyperbolic function was used with a start and end spacing specified. Table 5 shows the parameters set in StarCCM+ for the rectangular channel.

**Table 5. Parameter assigned for surface mesh generation in a rectangular channel**

Representation	Number of Divisions	Points Distribution type	Spacing at start and end
<i>a</i>	130	Evenly distributed along the line	-
<i>b</i>	130	Uneven distribution - Double sided hyperbolic distribution	$4.8 \times 10^{-5}$ m

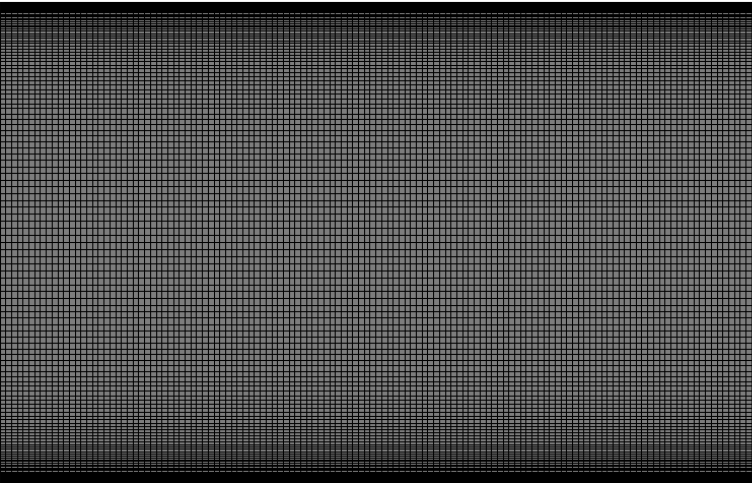


Figure 21. Surface mesh for rectangular channel geometry

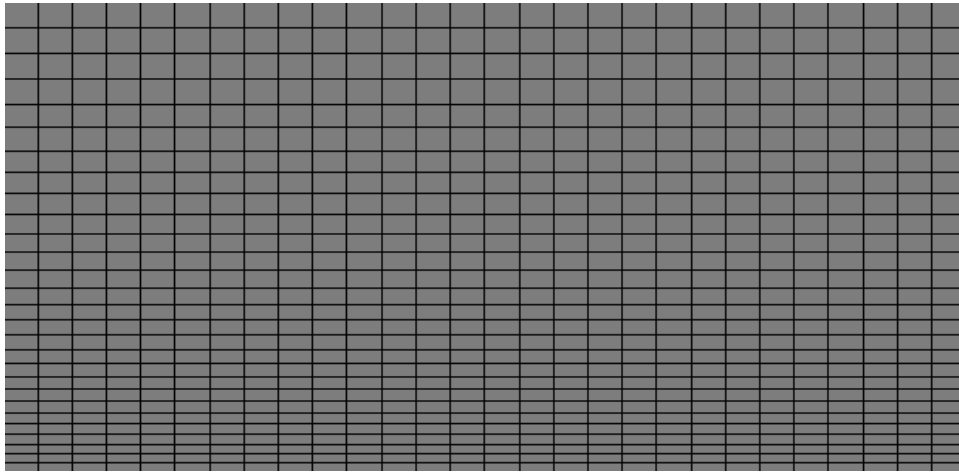


Figure 22. Surface mesh in the near wall region of channel geometry

The volume mesh was generated by specifying 130 layers in the streamwise direction. The final volume mesh generated is shown in Figure 23.

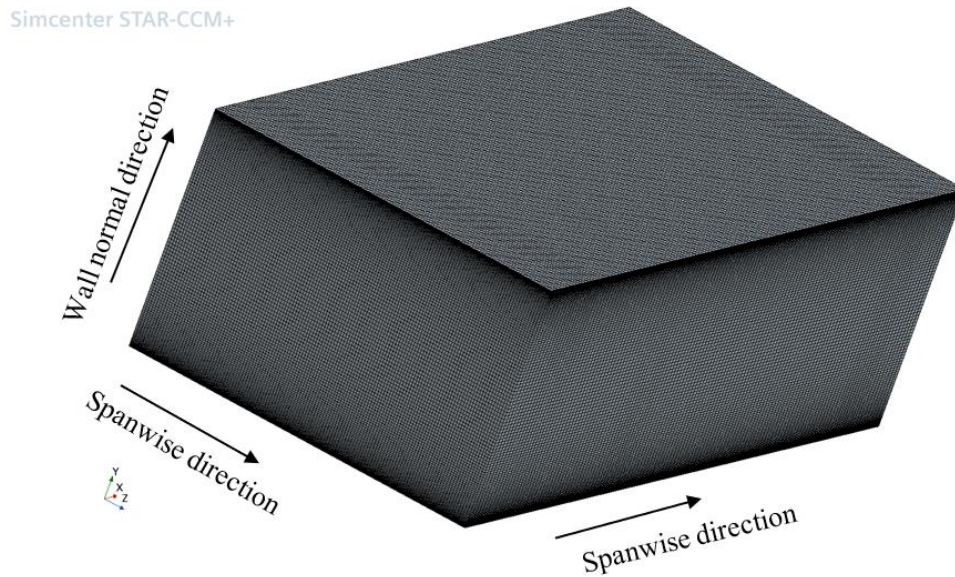


Figure 23. Volume mesh generated for rectangular minichannel



### *Mesh generation for circular minichannel*

The directed meshing approach was used to mesh a circular minichannel. The inlet and outlet of the minichannel were taken as source (red) and target (green) surface respectively, as shown in Figure 24.

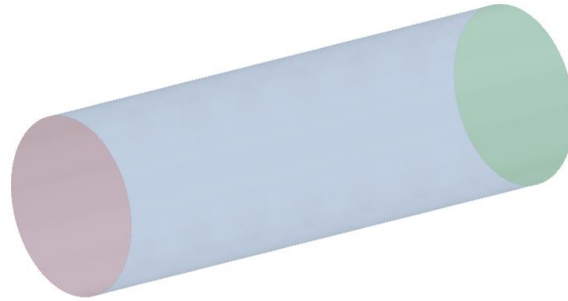


Figure 24. Source and target surfaces representative used to generate volume mesh for a minichannel

A butterfly face mesh was constructed as the initial surface mesh, because of its ability to generate structured meshing elements for a circular topology. Figure 25 shows a butterfly mesh generated for the minichannel. It consists of 5 different patches (1 core and 4 sides).

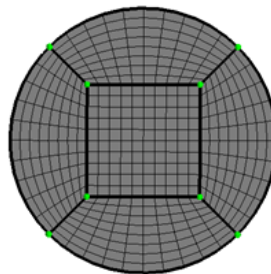


Figure 25. Butterfly face mesh for circular minichannel

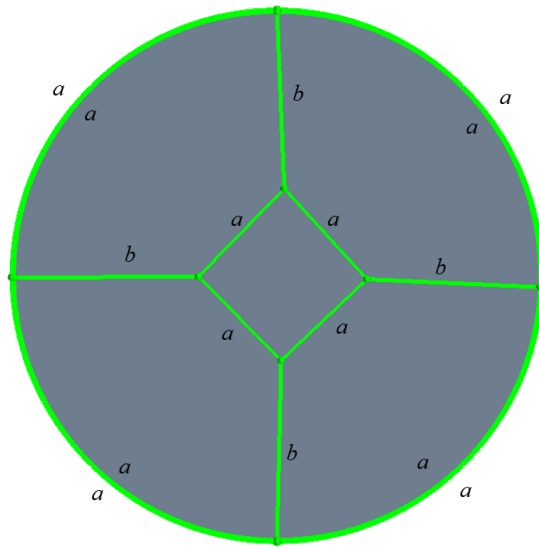


Figure 26. 2D surface of minichannel with patches

Figure 26 shows the patches created for the circular minichannel. The lines and arcs, which are divided into the same number of points were marked with the same letters. Figure 27 shows the magnified view near the solid-liquid interface.

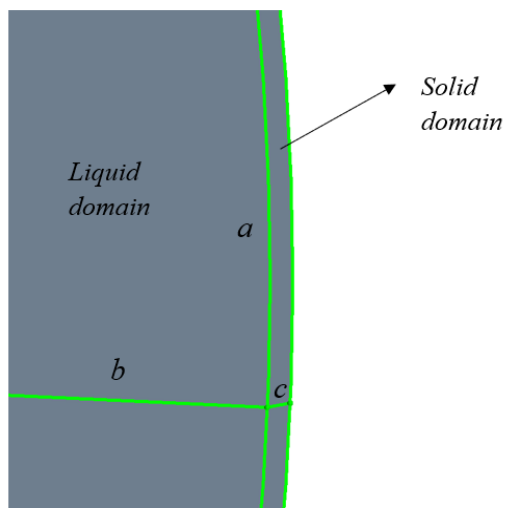
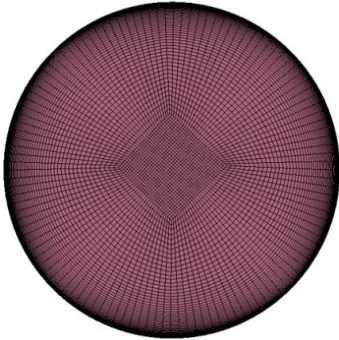


Figure 27. Patch near the solid-liquid interface

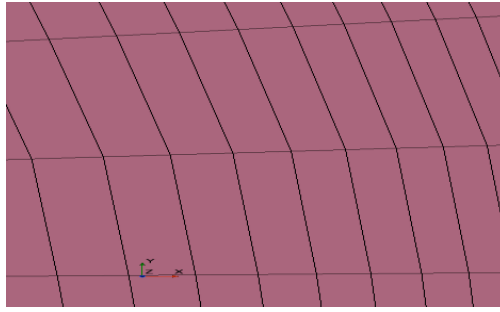
The one-sided hyperbolic function was used to compute the cell distribution growth based on the hyperbolic stretching law. For this approach, the initial spacing at the start of stretching needed to be specified. The spacing at the start of the hyperbolic distribution is shown in Table 6, which represents the distance from the wall, where the first grid point was located. This value was fixed in such a way that the wall  $y^+$  value, which represents the non-dimensional distance normal to the wall, was less than 1. Figure 28 shows the surface mesh generated.

**Table 6. Parameters assigned for surface mesh in circular minichannel**

Representation	Number of Divisions	Points Distribution type	Spacing at start
<i>a</i>	30	Evenly distributed along the line/arc	-
<i>b</i>	50	Uneven distribution - One sided hyperbolic distribution	$3.0 \times 10^{-5}$ m
<i>c</i>	10	Evenly distributed along the line	-



(a)



(b)

Figure 28. Initial surface mesh for minichannel geometry

Once the surface mesh was generated, the next step was to create the volume mesh. The volume mesh was generated by specifying the number of layers required in the sweep direction. 192 layers were considered in order to effectively capture the slip behavior on the surface. Figure 29 shows the volume mesh generated for this study.

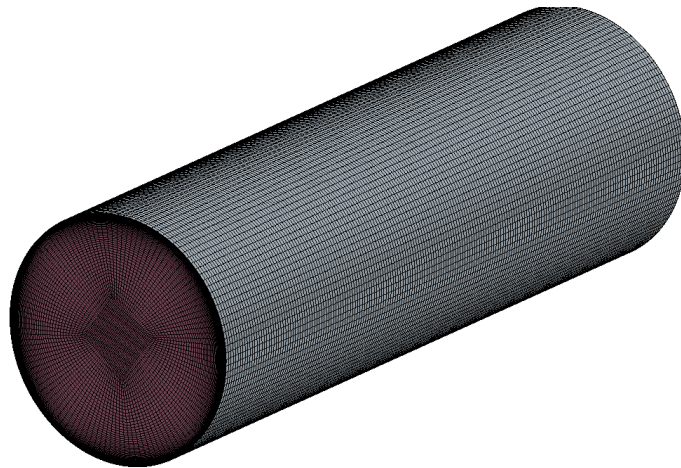


Figure 29. Volume mesh for minichannel geometry

### ***Boundary Conditions***

After the generation of discretized volume domain, the next step was to assign boundary conditions for the two geometries considered in this numerical study. The

following subsection discusses the boundary conditions for rectangular minichannel, which was used for validation purposes and is followed by boundary conditions for circular minichannel.

**a) Rectangular minichannel**

As discussed earlier, the rectangular minichannel geometry was considered for the validation of the implemented numerical scheme. Figure 30 shows the different boundaries of the rectangular minichannel.

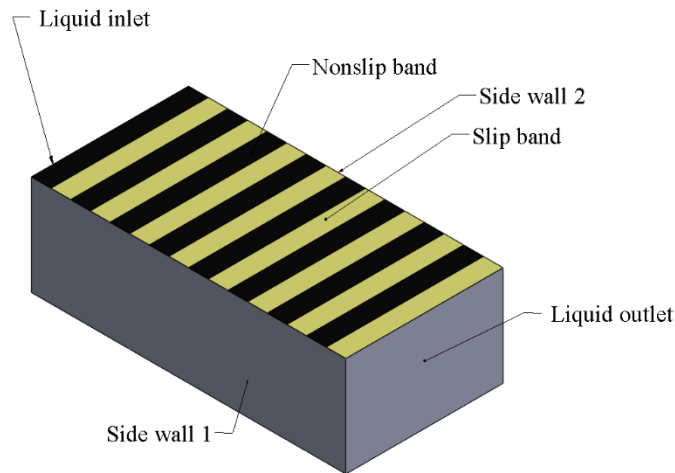


Figure 30. Rectangular minichannel with boundary assignments

The liquid inlet and liquid outlet were coupled together to form a periodic boundary. A pressure jump value was specified for this interface. The pressure jump value was calculated based on the mean pressure gradient value specified in the reference study [37]. The reference study [37] considered a pressure gradient of  $\rho u_\tau^2$  where  $u_\tau$  denotes friction velocity. The sidewall 1 and sidewall 2 were coupled together into a periodic

boundary with zero pressure jump. The non-slip bands were provided with nonslip boundary conditions and the slip bands with slip boundary condition.

Table 7 shows the rectangular minichannel boundary condition values considered in the numerical validation study.

**Table 7. Boundary conditions for rectangular minichannel**

Faces	Physical specification	Value
Liquid inlet	Periodic interface-pressure jump value specified	0.09 Pa
Liquid outlet		
Wall (Slip band)	Shear free (zero shear)	-
Wall (Non-slip band)	No slip Zero fluid velocity at wall	-
Sidewall 1	Periodic interface-pressure jump value specified	0 Pa
Sidewall 2		

***b) Circular minichannel***

As in the validation case, boundary conditions needed to be specified for the circular minichannel. Figure 31 shows the different boundaries on the liquid and solid domains of the minichannels considered in the study. In the figure, the non-slip region is depicted by black color and the slip region is depicted by yellow color.

The liquid inlet and outlet were coupled together to form a periodic interface. A mass flow rate was specified for this interface. The mass flow rate was calculated using the equation

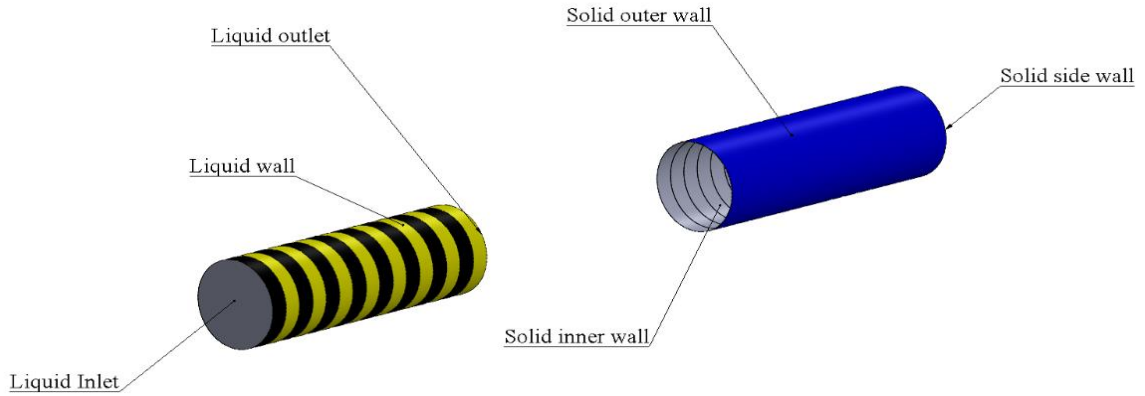


Figure 31. Circular minichannels with solid and liquid domain boundary assignments

$$\dot{m} = \rho A \bar{v} \quad (7)$$

where  $\dot{m}$ ,  $\rho$ ,  $A$  and  $\bar{v}$  represent mass flow rate, the density of the fluid, cross-sectional area of minichannels, and average velocity of the fluid, respectively. The average velocity was calculated for a specific Reynolds number value using the following equation:

$$\bar{v} = \frac{Re \mu}{\rho D} \quad (8)$$

where  $Re$ ,  $\mu$ , and  $D$  denote the Reynolds number, dynamic viscosity of the fluid, and diameter of the minichannel, respectively.

For the liquid wall, two boundary conditions were specified. For the slip and non-slip bands, shear-free boundary and non-slip boundary conditions were specified,

respectively. The solid inner wall of the copper tube and the liquid wall were coupled together to form a thermal interface, which allowed the heat to transfer from the solid to the liquid region. To ensure a 2°C-temperature difference between the two ends of the minichannel, a heat flux value of 60,000 W/m<sup>2</sup> was specified on the solid outer wall. The solid side walls were adiabatic. Table 8 shows the boundary conditions values considered in the numerical study.

**Table 8. Boundary conditions for fluid and solid domain in circular minichannel**

<b>Faces</b>	<b>Physical specification</b>	<b>Value</b>
Liquid inlet and outlet	Periodic interface- mass flow specified	0.120 kg/sec
Liquid wall (Slip band)	Shear free (zero shear)	-
Liquid wall (Non-slip band)	No slip Zero fluid velocity at wall	-
Solid top wall	Heat flux	60,000 W/m <sup>2</sup>
Solid side wall	Adiabatic (no heat transfer)	-

### ***Solver Selection***

After the selection of boundary conditions, the next step was to select the CFD solver and solution methods using Star-CCM+. Table 9 shows the CFD solvers and models implemented in this numerical study.



**Table 9. CFD solvers and models used in the numerical study**

Parameters	Definition
Solver	Three-dimensional, steady state
Viscous model	$\kappa$ - $\omega$ SST low $y^+$ turbulence model
Flow and energy model	Coupled flow and coupled energy model

The  $\kappa - \omega$  turbulence model is a two-equation model, which solves for two transport equations: the turbulent kinetic energy ( $\kappa$ ) and the specific dissipation rate ( $\omega$ ) of turbulent kinetic energy. The advantage of the  $\kappa - \omega$  turbulence model over the  $\kappa - \epsilon$  model is its improved performance for boundary layer flows. Since the slip phenomenon is known to have a greater impact on the near-wall region, it was important to have an accurate numerical scheme near the wall. Thus, the  $\kappa - \omega$  model was selected for this numerical study. Of the available  $\kappa - \omega$  model variants,  $\kappa - \omega$  SST model was used to eliminate the issues related to sensitivity at the inlet conditions. The  $\kappa - \omega$  SST model effectively blends the  $\kappa - \epsilon$  model in the far-field region with the  $\kappa - \omega$  model near the wall.

The low  $y^+$  wall treatment approach was used, in which the boundary layer was resolved with fine-layered mesh. The resolving of boundary layers eliminates the use of wall functions to model the near-wall flow. A coupled flow solver, which solves the conservation of mass and momentum equations simultaneously was used in this study. The coupled solver was chosen over segregated solver because of its robustness and ability to achieve convergence for refined meshes. In general terms, the selection of the CFD solution methods have a direct impact on the pressure, temperature, and velocity solutions in any study. For the computation of convection flux through cells, a 2<sup>nd</sup> order upwind

scheme was chosen for this study. This scheme introduces linear interpolation of cell value on either side of the upstream or downstream face. The coupled energy and coupled solid energy models were used to solve the energy equation. Table 10 shows the CFD solutions method options used in this study.

**Table 10. CFD solution method options used in the numerical study**

Parameters	Definition
Time-integration scheme	Implicit
Convection	2 <sup>nd</sup> order upwind scheme
Under-relaxation factor	0.8

***Convergence criterion for the numerical study***

For the minichannel geometry, two simulations were set up for each of the slip/non-slip cases studied. In the first simulation, the solid outer wall was considered to be adiabatic, and the temperature of the whole system was set to 300 K. In this simulation, the flow was allowed to develop hydrodynamically. The convergence criterion for this simulation was based on the attainment of hydrodynamically fully developed flow. The bulk velocity of the minichannel was monitored over the iterations. Once the bulk velocity reached a constant average value, the flow was considered to be hydrodynamically developed.

After ensuring that the flow was hydrodynamically fully developed, the heat flux condition on the solid outer wall was included in the simulation. The simulation was run until the fluid reached a thermally fully developed state. Local convective heat transfer

value near the end of the domain was also monitored. Once the value of local convective heat transfer reached a constant value, the flow was considered to be thermally fully developed. When the difference between local convective heat transfer values from two consecutive iterations was less than  $1 \times 10^{-5}$ , the simulation was assumed to have converged.

### ***Post Processing***

After the completion of the simulation, the results were collected and compiled for post-processing. Post-processing included analysis of the results using StarCCM+ Viewer, Microsoft Excel, and Tecplot. StarCCM+ was used to visualize the velocity and temperature contours over the length of the minichannel. Excel and Tecplot were used to plot important parameters, which helped understand the thermal performance effects of non-slip/slip surfaces.

To better understand the thermal performance behavior, parameters representative of flow and heat transfer behavior such as local shape factor, local slip length, hydrodynamic boundary layer, thermal boundary layer, heat transfer coefficient, Nusselt number and performance evaluation criteria (PEC) were plotted as a function of streamwise distance along the circular minichannel. These parameters were calculated as follows:

a) Local first shape factor ( $H_{12,z}$ )

To determine the nature of boundary layer flow, the local shape factor was calculated at different streamwise locations ( $z$ ) along the circular minichannel. The local shape factor is defined as:

$$H_{12,z} = \frac{\delta_z^*}{\theta_z} = \frac{\int_0^R \left(1 - \frac{u_z(r)}{u_0}\right) dr}{\int_0^R \left(\frac{u_z(y)}{u_0}\right) \left(1 - \frac{u_z(r)}{u_0}\right) dr} \quad (9)$$

where,

$\delta_z^*$ : displacement thickness

$\theta_z$ : momentum thickness

$u_0$ : centerline velocity

b) Local slip length

Local slip length was used to quantify the magnitude of slip conditions along the minichannel. It was calculated as follows:

$$b = \frac{V_s}{\left(\frac{\partial V}{\partial y}\right)} \quad (10)$$

where,

$b$ : slip length

$V_s$ : slip velocity

$\frac{\partial V}{\partial y}$ : velocity gradient near the wall

c) Hydrodynamic boundary layer

Hydrodynamic or momentum boundary layer refers to the fluid flow region, where the fluid flow patterns are affected by the viscous drag from the surface wall. The hydrodynamic boundary layer thickness ( $\delta_x$ ) was defined as the

distance from the wall where the local velocity reaches 99% of the centerline velocity, as follows:

$$u = 0.99V_c \quad (11)$$

where  $V_c$  refers to the centerline velocity of the minichannel.

d) Thermal boundary layer

The thermal boundary thickness ( $\delta_t$ ) is defined as the normal distance ( $y$ ) of a point away from the surface where the local temperature difference between the fluid and surface reaches 99% of the maximum temperature difference, as follows:

$$(T_s - T_y) = 0.99(T_s - T_c) \quad (12)$$

where  $T_s$ ,  $T_y$  and  $T_c$  denote wall temperature, the temperature at location  $y$ , and centerline temperature, respectively.

e) Local convective heat transfer coefficient ( $h_z$ )

The local convective heat transfer coefficient ( $h_z$ ) at a particular streamwise location ( $z$ ) was calculated as:

$$h_z = \frac{q''}{T_{w,z} - T_{b,z}} \quad (13)$$

where  $q''$  denotes the constant heat flux applied,  $T_{w,z}$  surface temperature at streamwise location  $z$  and  $T_{b,z}$  the fluid bulk temperature at location  $z$ .

f) Local Nusselt number

Local Nusselt number at a streamwise location  $z$  was calculated as:

$$Nu_z = h_z D / k \quad (14)$$

where  $D$ ,  $k$  represents the hydraulic diameter and thermal conductivity of the fluid, respectively.

g) Average Nusselt number

The average Nusselt number for the minichannel was calculated as follows:

$$Nu_{avg} = \frac{\int_{inlet}^{outlet} Nu_z dz}{L} \quad (15)$$

where  $L$  refers to the length of the minichannel.

h) Performance evaluation criteria (PEC)

To understand the thermal performance effects due to the imposed slip/non-slip boundary conditions using Nusselt number and friction factor, the performance evaluation criteria was calculated as follows:

$$PEC = \frac{\left( \frac{Nu_{patterned}}{Nu_{smooth}} \right)}{\left( \frac{f_{patterned}}{f_{smooth}} \right)^{1/3}} \quad (16)$$

where *patterned* refers to configurations with slip/nonslip bands and *smooth* refers to nonslip walls. The friction factor ( $f$ ) was calculated using the Darcy Weisbach formula given by:

$$f = \frac{2\Delta p D}{L \rho \bar{v}^2} \quad (17)$$

where,

$\Delta p$  : pressure drop across the minichannel

$D$  : hydraulic diameter of the minichannel

$L$  : Length of the minichannel

$\rho$  : Density of the fluid

$v$  : Average fluid velocity

## 4.2 Grid Independence Study

While performing numerical simulations, it is very important to ensure that the obtained results are insensitive to the grid resolution or refinement. Thus, a grid independence study was carried out for this study. Three different grid sizes were considered for the grid independence study. The grid convergence index (GCI) has been calculated for the meshes used in this study. The procedure specified by AMSE for calculation of GCI used in the study is as follows [43]:

### **Step 1**

The first step was to define a grid size  $\sigma$ . The grid size for this numerical study was calculated as:

$$\sigma = (V/N)^{1/3} \quad (18)$$

where,

$V$ : Total volume of the meshed domain

$N$ : Total number of elements

## **Step 2**

The next step was to select 3 different grid sizes and run simulations in order to determine the values of variables important in the numerical study. The variable ( $f$ ) used in the grid independent study was the convective heat transfer coefficient,  $h$ .

The grid sizes were selected in such a way that the grid refinement factor,  $r = \frac{\sigma_{coarse}}{\sigma_{fine}}$  was greater than 1.3.

## **Step 3**

This step involved the calculation of apparent order of accuracy,  $p$ , where  $\sigma_3$ ,  $\sigma_2$  and  $\sigma_1$  represented the coarsest, medium, and finest grid sizes, respectively. Also, the ratios among the grid sizes were computed as follows:

$$r_{21} = \sigma_2/\sigma_1$$

$$r_{32} = \sigma_3/\sigma_2$$

The grid sizes were chosen such that  $r_{21}$  could be equal to  $r_{32}$ . The order of accuracy  $p$  was found using the following equation:

$$p = \frac{\ln\left(\frac{f_3-f_2}{f_2-f_1}\right)}{\ln(r_{21})} \quad (19)$$

where,

$f_1$  : Value of the variable for the finest grid size

$f_2$  : Value of the variable for the medium grid size



$f_3$  : Value of the variable for the coarsest grid size

#### **Step 4**

This step involves the calculation of extrapolated values and the Grid Convergence Index (GCI) for the set of meshes. The extrapolated value refers to the estimation of the true value of the variable that was being examined. It is calculated as follows:

$$f_{ext} = (r_{21}^p f_1 - f_2) / (r_{21}^p - 1) \quad (20)$$

The grid convergence quality is calculated using the Grid Convergence Index as shown below and is calculated at refinement steps. Thus, the GCI was calculated for fine and medium mesh grids.

The equation used to compute GCI is as follows:

$$GCI = \frac{F_s |\varepsilon|}{r^p - 1} \quad (21)$$

where  $\varepsilon$  is the error between the grids and  $F_s$  is the factor of safety.

#### **Step 5**

The last step is to check if the grids considered are in the asymptotic range of convergence. The grids are said to be in the asymptomatic range of convergence if  $\frac{GCI_{2,3}}{GCI_{1,2} r^p}$  is approximately equal to 1. If the grids are not in the asymptomatic range of convergence, then the solution cannot be considered to be grid independent.

CHAPTER V  
RESULTS AND DISCUSSION

This chapter discusses the simulation results of all the non-slip/slip cases considered in this study. As part of the CFD simulations, a grid independence study was carried out first to ensure that the results were insensitive to grid resolution. This was followed by validation of the numerical scheme, including thermal validation and pressure drop validation.

The results and discussion of effects of non-slip/slip bands on pressure drop, slip velocity, local Nusselt number, local convective heat transfer coefficient, boundary layer are presented as well.

### 5.1 Grid Independence Study

As discussed in section 4.2, 3 different grid sizes were considered for the grid independence study. Table 11 shows the mesh count and grid size for the three meshes used in the study.

**Table 11. Mesh sizes considered for grid independence study**

Mesh Type	Mesh count	Grid size ( $\mu\text{m}$ )
Fine	1,555,200	37.5
Medium	777,600	47.3
Coarse	388,800	59.6

The convective heat transfer coefficient was considered as the variable of interest for the grid independence study. Table 12 shows the value obtained for the different mesh

sizes used in the study. Using these values, the order of accuracy,  $p$ , was calculated, which was found to be 1.80.

**Table 12. Convective heat transfer coefficient for different grids**

	Fine grid	Medium grid	Coarse grid
<b>Convective heat transfer coefficient (W/m<sup>2</sup>K)</b>	978.26 ( $f_1$ )	985.24 ( $f_2$ )	995.83 ( $f_3$ )

Finally, the GCI values and extrapolated values for the grid refinements were calculated.

Table 13 shows the GCI values for the grid refinement levels.

**Table 13. GCI and extrapolated values for refined grids**

<b>GCI<sub>2,3</sub>(coarse to medium)</b>	<b>GCI<sub>1,2</sub>(medium to fine)</b>	<b>Extrapolated Value</b>
2.6 %	1.79 %	964.13 (W/m <sup>2</sup> K)

Thus, the refinement of the grid led to reduction in the GCI values, ensuring grid independence. Also, the value of  $\frac{GCI_{2,3}}{GCI_{1,2}r^p}$  was found to be 1.0054, thus ensuring that the grid sizes were in the asymptomatic range of convergence.

## 5.2 Validation of Numerical Scheme

To validate the numerical scheme discussed in the previous chapter, the results obtained by Faud *et al.* [37] were reproduced numerically. The cases chosen from the Faud *et al.* [37] research are summarized in Table 14. The cases were used to validate the hydrodynamics of the fluid problem described in Faud *et al.* [37]. The geometry considered for this validation was a rectangular minichannel as discussed in Chapter IV.

**Table 14. Cases considered for numerical validation**

Type of simulation	Friction Reynolds number	Nonslip/slip ( <i>a/b</i> ) ratio in minichannel	Width of nonslip band, ( <i>a</i> ), in minichannel
Uncontrolled Turbulence (Nonslip walls)	180	-	-
Ridges in transverse direction [37]	180	1:1	$0.4\delta$

Figure 32 shows the variation of normalized mean velocity with  $y^+$  values for uncontrolled turbulence. It is evident from the figure that the simulation results were in good agreement with the reference thus validating the numerical setup for the uncontrolled turbulence case. Table 15 shows the comparison of the normalized bulk velocity to further ascertain the claim that the numerical setup proposed is physically accurate.

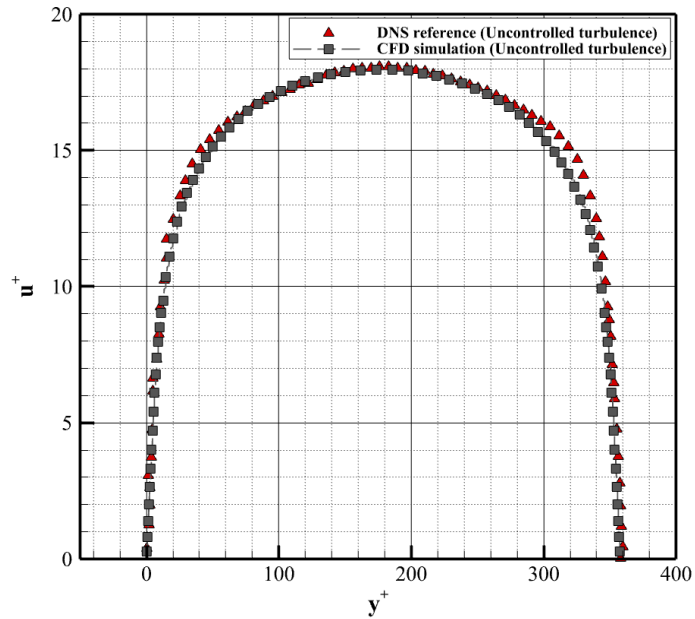


Figure 32. Variation of normalized mean velocity with  $y^+$  values for uncontrolled turbulence case

**Table 15. Normalized Bulk Velocity Comparison for Uncontrolled Turbulence**

	Reference [37]	Simulation	%Error
$U_b/u_\tau$ ( Normalized Bulk Velocity)	15.70	15.68	0.12

Figure 33 shows the comparison of the normalized mean velocity for the case of a non-slip to slip ratio of 1. From the figure, it can be concluded that there is a good agreement between the CFD and the reference solution [37] near the wall region. In the core domain of the fluid, the current CFD simulation underpredicts the velocity in comparison to the reference [37]. The reason for this could be the fact that the current simulations used RANS models whereas Direct Numerical Simulation was employed in the reference paper. The normalized bulk mean velocity obtained from the simulation had a 2.5% error compared to the reference, as mentioned in Table 16.

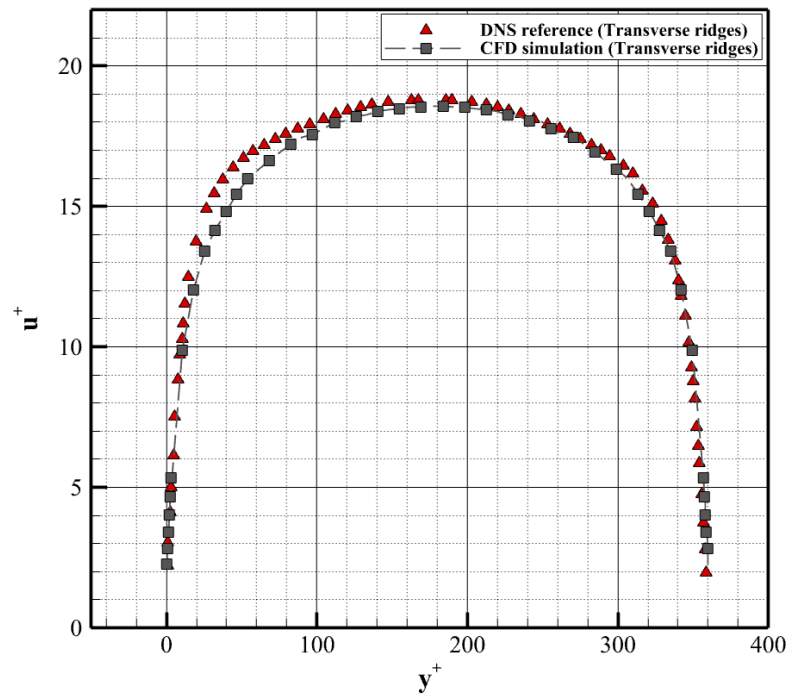


Figure 33. Variation of normalized mean velocity with respect to  $y^+$  values for transverse ridges case

**Table 16. Comparison of normalized bulk velocity for 1:1 ridges**

	Reference [37]	Simulation	%Error
$U_b/u_\tau$ (Normalized Bulk Velocity)	16.60	16.18	2.5

***Thermal Validation***

To ensure that the thermal performance results obtained from the numerical study are accurate, a thermal validation study was performed. In this study, the average Nusselt number obtained from the simulation was compared against the Nusselt number obtained using the Gnielinski analytical correlation for the specified Reynolds number. The simulation was performed on the circular minichannel geometry with constant heat flux conditions on the walls for a Reynolds number of 5600.

Gnielinski's correlation was used for comparison purposes. The correlation is as follows:

$$Nu_D = \frac{\left(\frac{f}{8}\right)(Re_D - 1000)Pr}{1 + 12.7\left(\frac{f}{8}\right)^{1/2}(Pr^{2/3} - 1)} \quad (22)$$

where  $f$ ,  $Re_D$ ,  $Pr$  denote friction factor, Reynolds number, and Prandtl number respectively. The friction factor was calculated using the Petukhov correlation given by

$$f = (0.79 \ln(Re_D) - 1.64)^{-2} \quad (23)$$

Table 17 shows the analytical and simulated average Nusselt number values.

**Table 17. Analytical and simulated values of average Nusselt number for circular minichannel**

Average convective heat transfer coefficient (h)(W/m <sup>2</sup> k)	Average Nusselt number (simulation)	Theoretical Nusselt number	% Error
978.12	50.78	45.31	11.06

An 11.06 % error was reported between the simulated and correlation obtained Nusselt number. It should be noted that Gnielinski’s empirical correlation provides values with +/- 10%.

***Validation of pressure drop in circular minichannel***

For the pressure drop validation, the Darcy-Weisbach equation was used. The equation is given as follows:

$$\Delta p = f \frac{L}{D} \frac{\rho}{2} \bar{v}^2 \tag{24}$$

where,

$\Delta p$  : pressure drop across the minichannel

$f$  : friction factor

$L$  : length of the minichannel

$\rho$  : Density of the fluid

$\bar{v}$  : Average fluid velocity

Table 18 shows the analytical and simulated pressure drop values.

**Table 18. Analytical and simulated pressure drop value for circular minichannel**

Analytical Pressure drop (Pa)	Pressure drop (Simulation)	% Error
1.30	1.37	4.7

**5.3 Effect of non-slip/slip ratio and width of non-slip bands on pressure drop**

As discussed in Chapter III, one of the objectives of this research was to study the effect of non-slip/slipcases on pressure drop. Table 19 shows the different configurations considered in this study and their corresponding pressure drop values.

**Table 19. Nonslip/slip configurations simulated in the study**

<b>Configuration</b>	<b>Nonslip/Slip (a)/(b) ratio in minichannel</b>	<b>Width of non-slip band, <math>a</math>, in minichannel</b>	<b>Pressure drop (Pa)</b>
1(Base case)	-	-	1.37
2	1:1	$0.2\delta$	1.27
3	1:1	$0.4\delta$	1.26
4	1:1	$0.8\delta$	1.22
5	1:3	$0.2\delta$	1.08
6	1:3	$0.4\delta$	0.97
7	1:3	$0.8\delta$	0.82

From the table it can be seen that the pressure drop was found to be highest for the base case which had non-slip walls. Pressure drop was found to be lower for all the non-slip/slip cases simulated in comparison to the base case. It was observed that the non-slip to slip ratio of  $\frac{1}{3}$  produced a higher reduction in pressure drop when compared to the non-slip to slip ratio of 1. This was due to the increase in slip surface for the non-slip to slip ratio of  $\frac{1}{3}$ , causing higher slip velocities and thus reducing the frictional resistance to flow. A lower frictional resistance led to a lesser pressure drop for a fixed mass flow rate.

For the non-slip to slip ratios, increasing the widths of the bands led to a reduction in pressure drop. Configuration 7 (Nonslip/slip ratio of 1:3 and nonslip band width of  $0.8\delta$ ) and configuration 2 (Nonslip/slip ratio of 1:1 and nonslip band width of  $0.2\delta$ ) depicted the highest and lowest reduction in pressure drop of 40.1% and 7.3% respectively when compared to the base case.

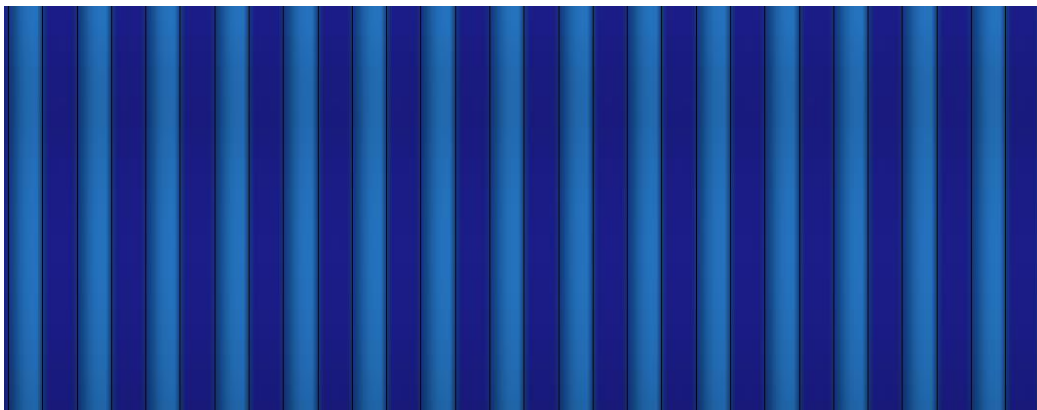


#### 5.4 Effect of non-slip/slip bands on slip velocity

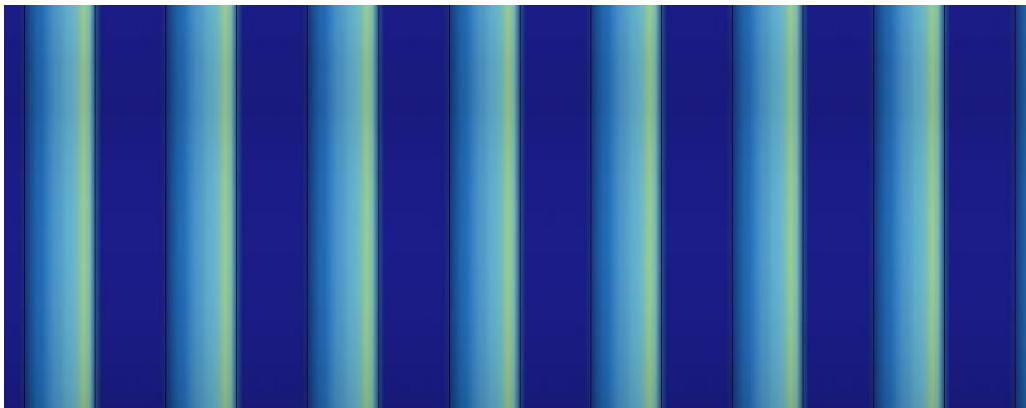
This subsection discusses the effect of the non-slip to slip ratio and the width of non-slip bands on the slip velocity profile on the surface of the circular minichannel.

**Error! Reference source not found.** and Figure 35 show the slip velocity contours on the surface of the minichannel for all the non-slip/slip cases considered in this study.

(a)



(b)



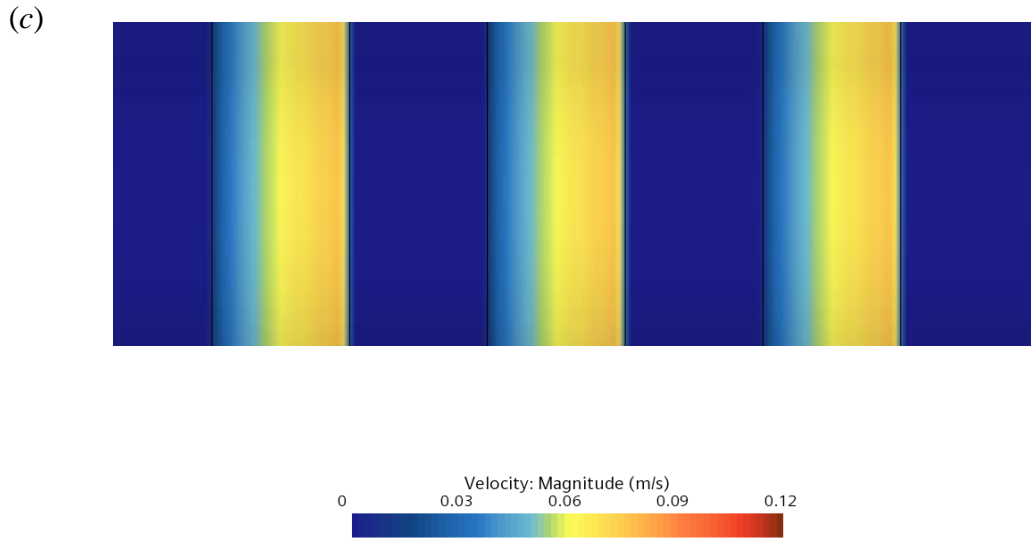
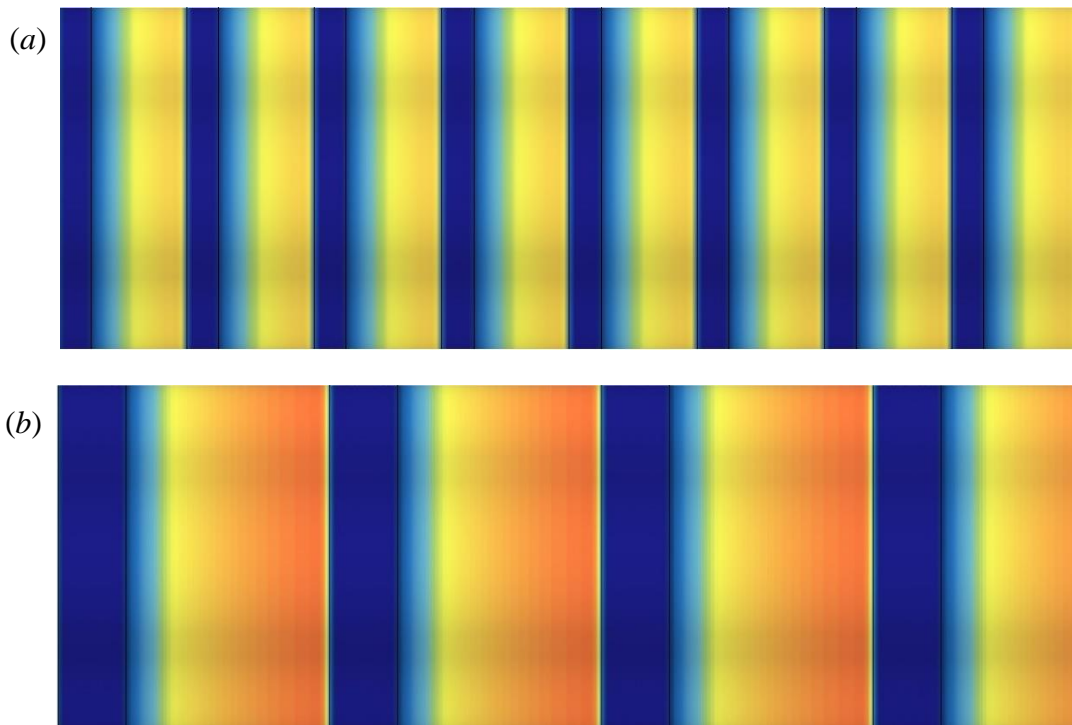


Figure 34. Slip velocity contour for non-slip to slip ratio 1.0 and non-slip width of (a)  $0.2\delta$ , (b)  $0.4\delta$ , (c)  $0.8\delta$



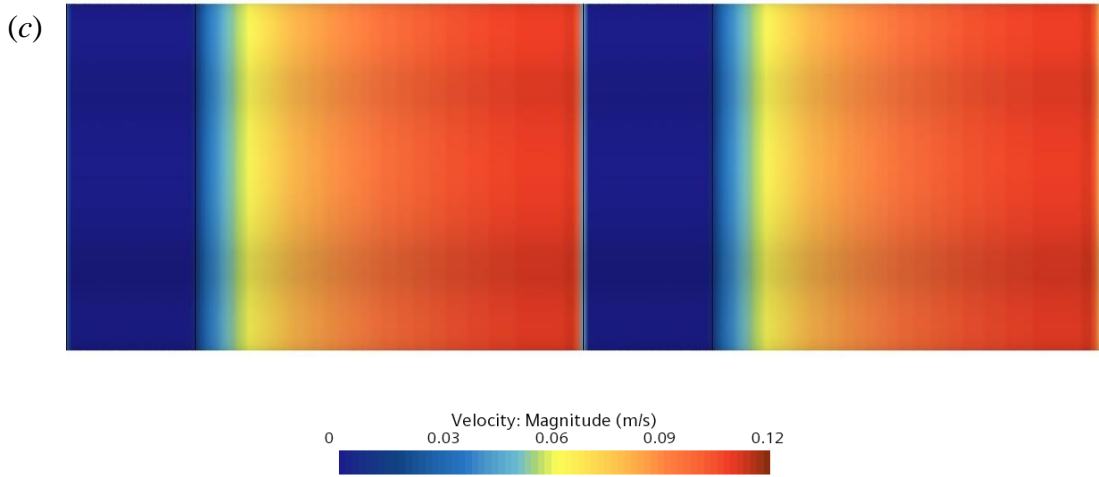
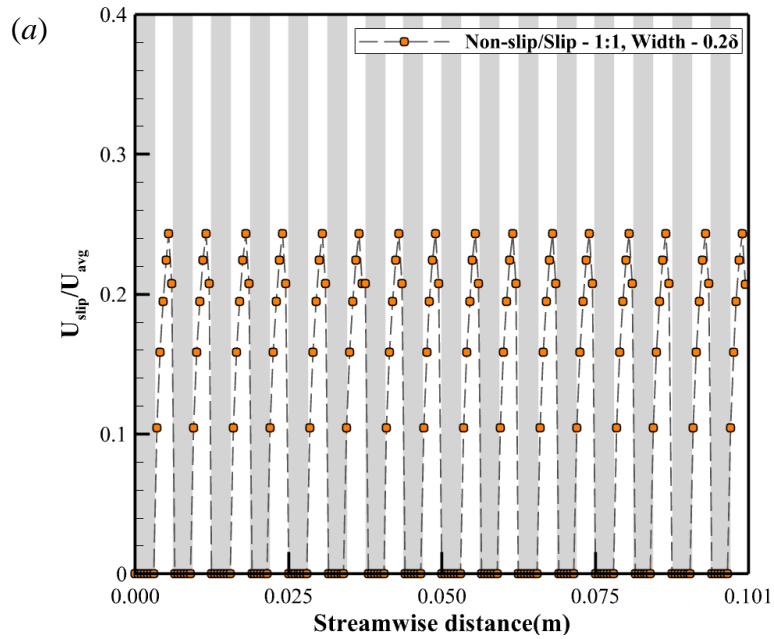


Figure 35. Slip velocity contour for non-slip to slip ratio 1/3 and non-slip width of (a)  $0.2\delta$ , (b)  $0.4\delta$ , (c)  $0.8\delta$

From Figure 34 and Figure 35, it is evident that the change in non-slip to slip ratio and width of non-slip bands leads to change in slip velocities at the surface. To better understand that effect, the slip velocities are plotted along the streamwise length for all non-slip/slip configurations as shown in Figure 36 and Figure 37.



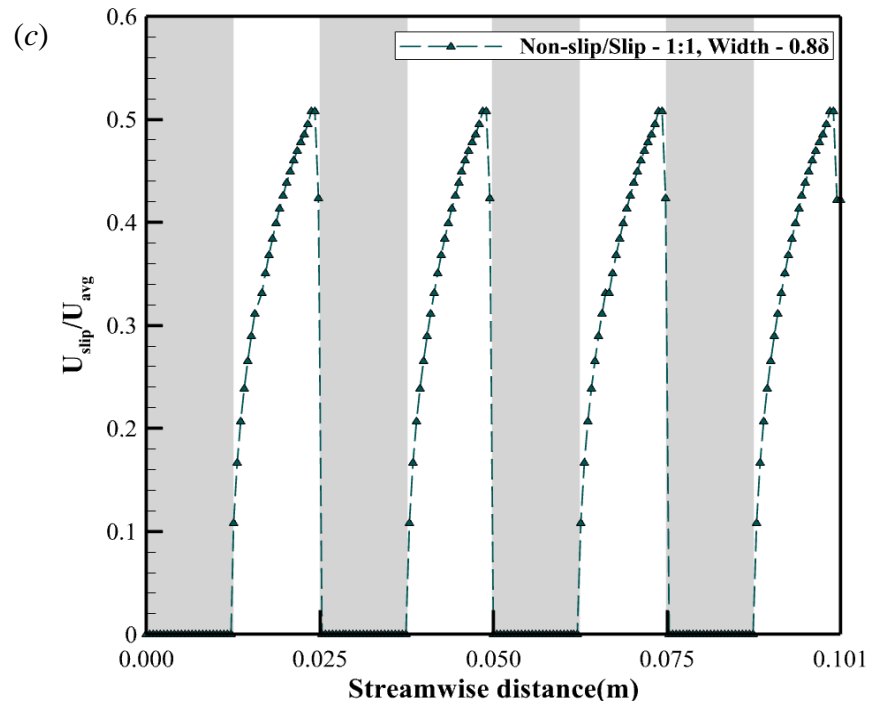
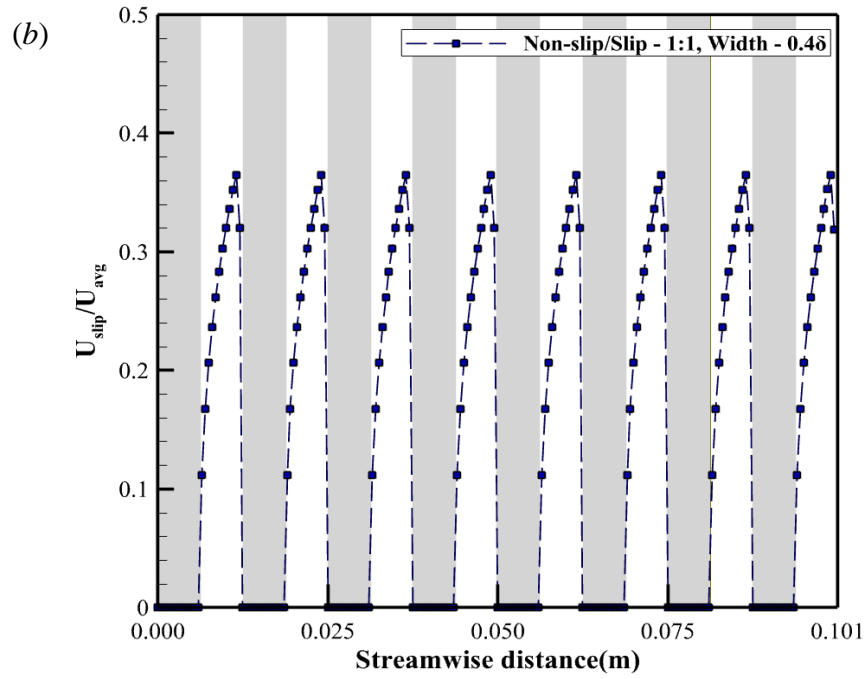
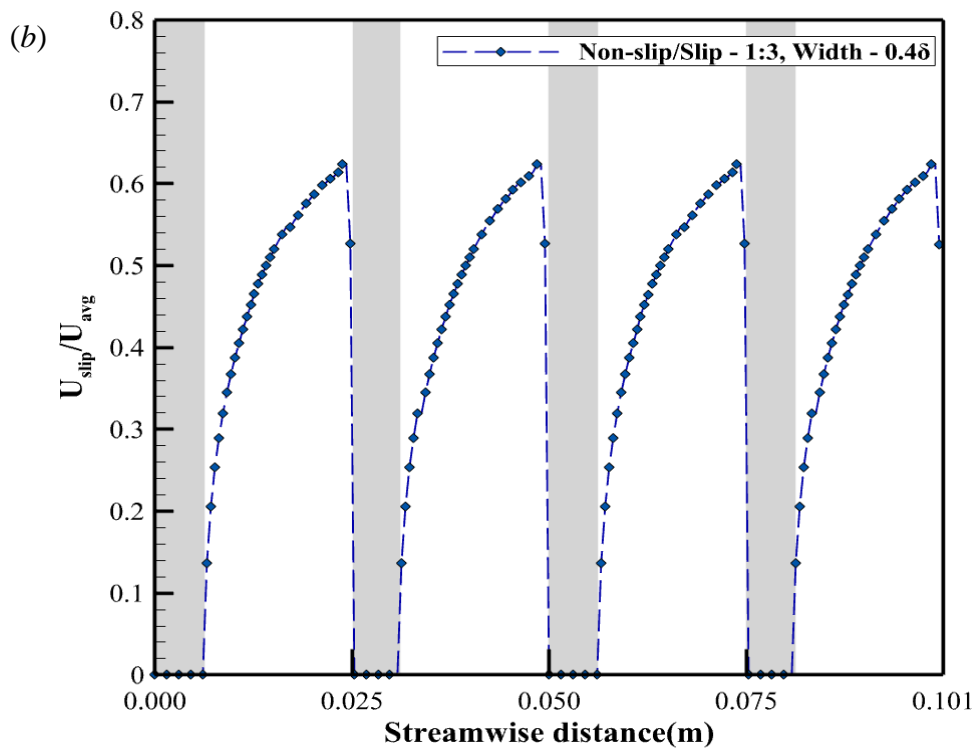
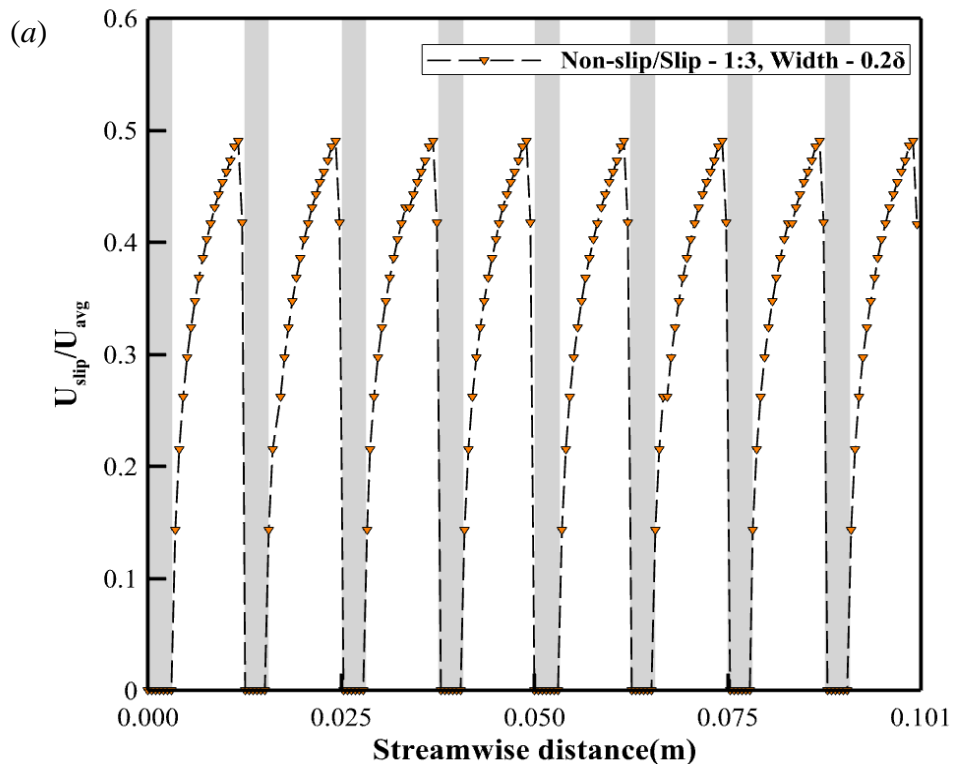


Figure 36. Slip velocity profile for non-slip to slip ratio of 1.0 and non-slip width of (a)  $0.2\delta$ , (b)  $0.4\delta$ , (c)  $0.8\delta$



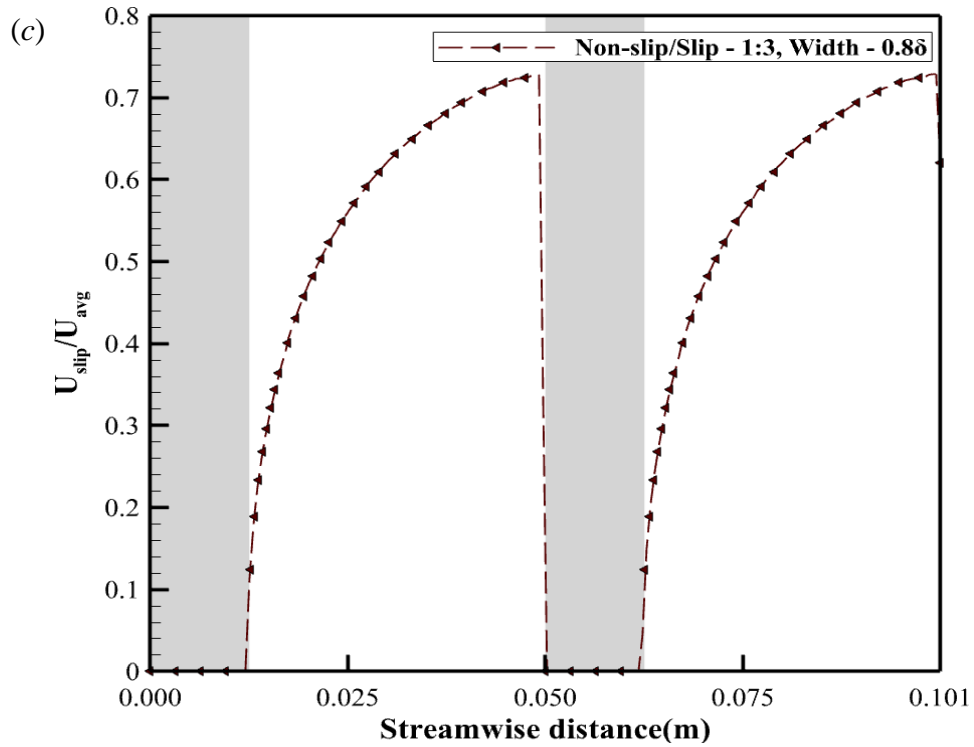


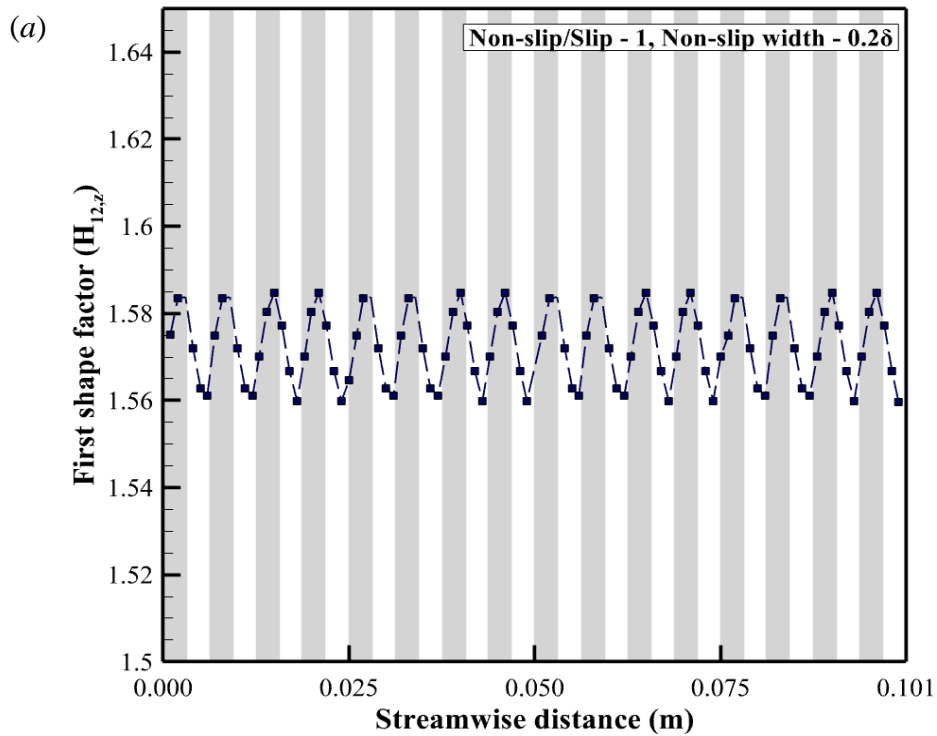
Figure 37. Slip velocity profile for non-slip to slip ratio of 1/3 and non-slip width of (a)  $0.2\delta$ , (b)  $0.4\delta$ , (c)  $0.8\delta$

From Figure 36 and Figure 37, it is evident that the fluid slip velocity increases from zero to a peak value over the slip surface and then reduces sharply as it comes in contact with the non-slip surface. It can also be observed that, with the change of non-slip to slip ratio from 1 to  $\frac{1}{3}$ , the peak value of the slip velocity increases. This was because the slip surface length increases with a decrease in the non-slip to slip ratio. Also, for a fixed non-slip to slip ratio, the increase in width of the nonslip band increases the peak value of the slip velocity. Another important finding was that the shape of the slip velocity profile over the slip region was not symmetric. This is due to the high shear stress encountered due to the non-slip surface after each slip band. Thus, it can be concluded that

non-slip/slip patterned surfaces have the ability to affect flow structure under turbulent flow conditions.

### 5.5 Effect of non-slip/slip bands on local first shape factor

To understand the nature of boundary layer flow in the circular minichannel, the local first shape factor ( $H_{12,z}$ ) was calculated for all the non-slip/slip cases simulated along the streamwise length. A value of  $H_{12,z}$  close to 2.59 indicates laminar boundary layer flow, and a value close to 1.3-1.4 indicates turbulent layer flow [44]. For the base case with non-slip walls, the value of  $H_{12,z}$  was found to be 1.63. Figure 38. Local first shape factor for non-slip to slip ratio of 1.0 and non-slip width of (a)  $0.2\delta$ , (b)  $0.4\delta$ , (c)  $0.8\delta$  Figure 38 and Figure 39 show the variation of local shape factor for all the non-slip/slip cases simulated in this study.



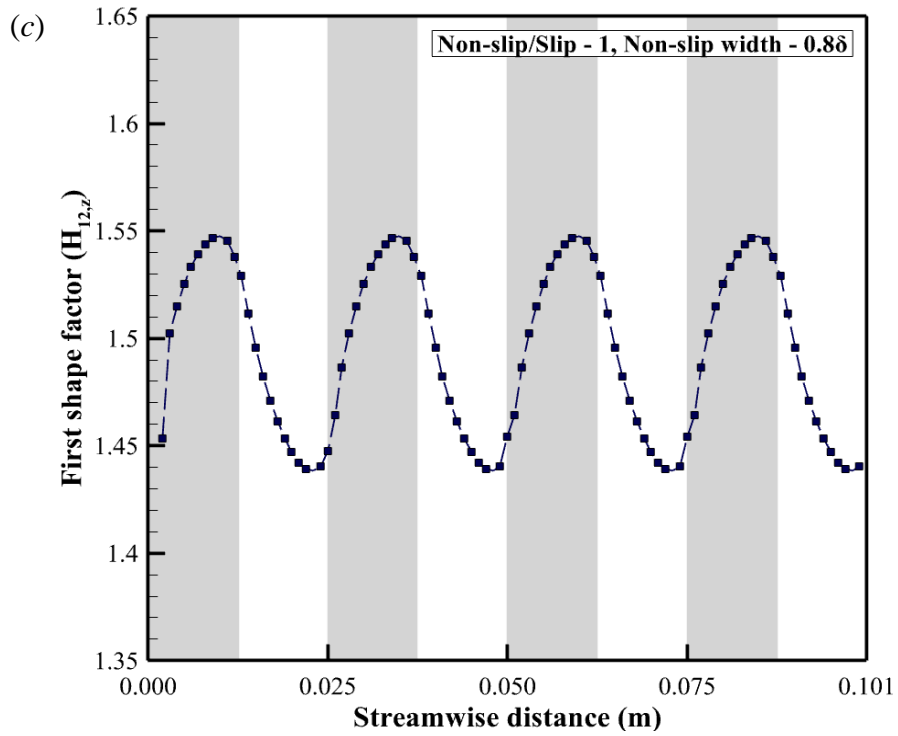
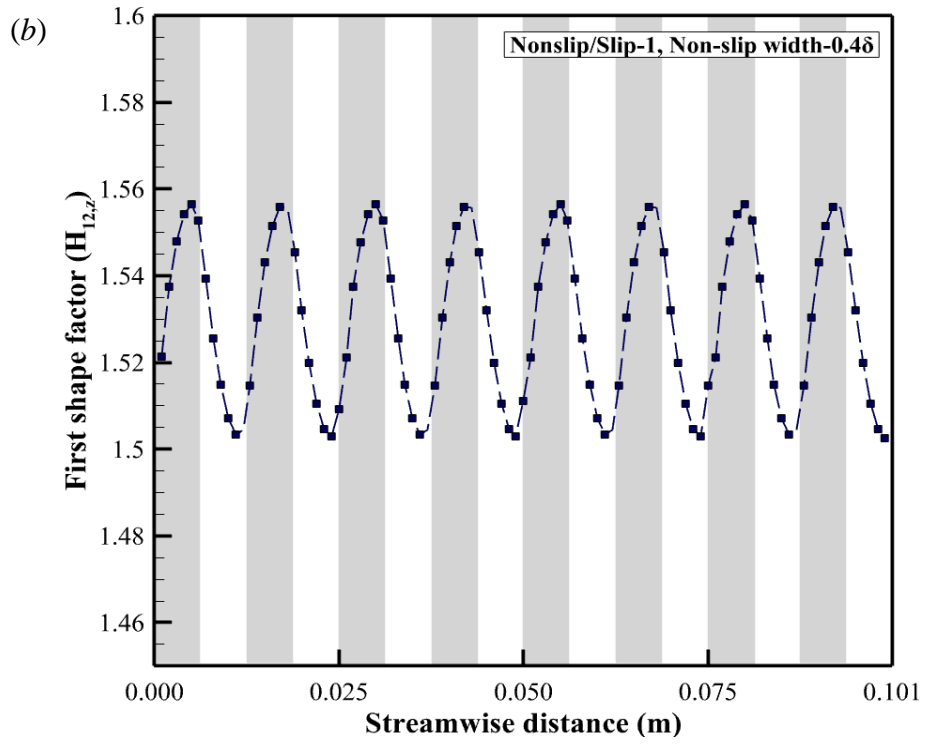
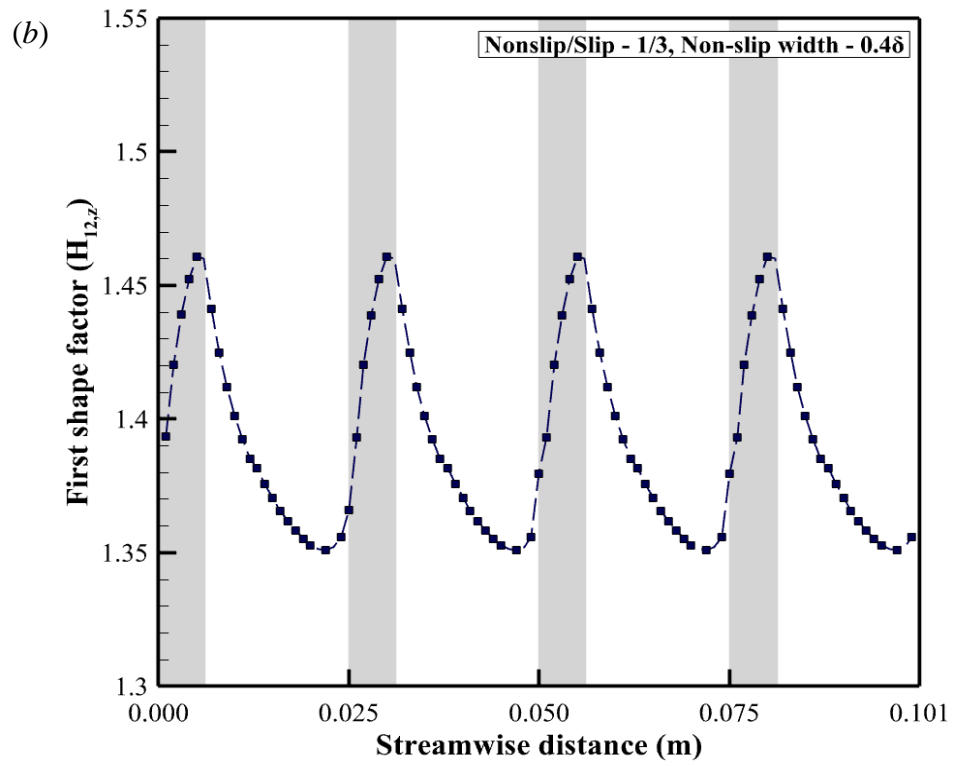
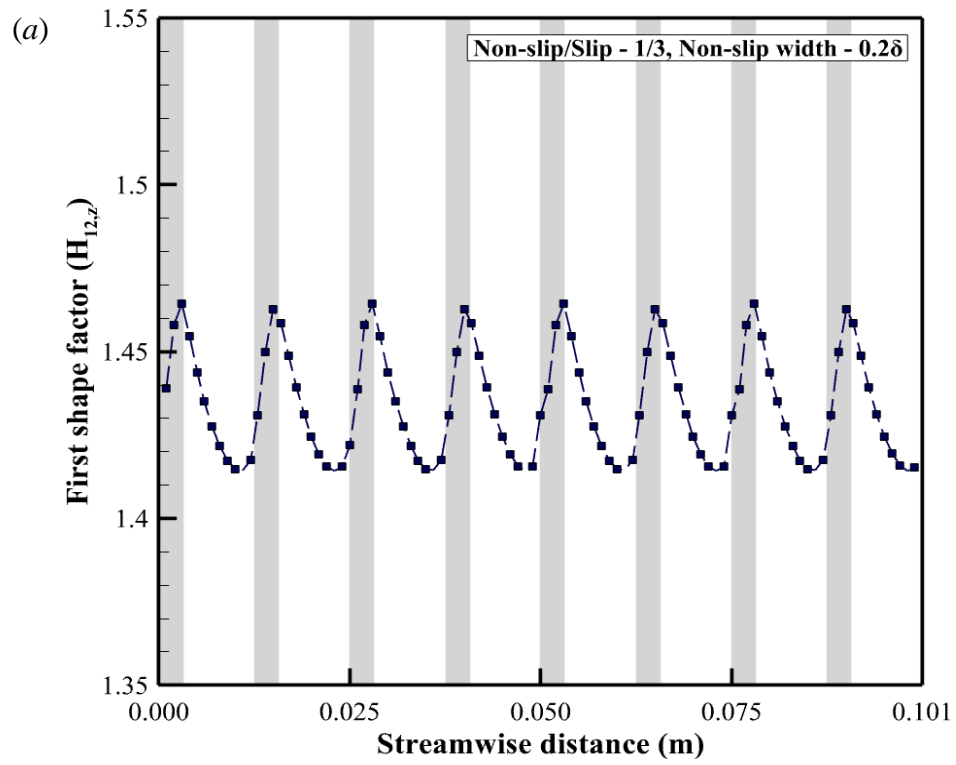


Figure 38. Local first shape factor for non-slip to slip ratio of 1.0 and non-slip width of (a)  $0.2\delta$ , (b)  $0.4\delta$ , (c)  $0.8\delta$





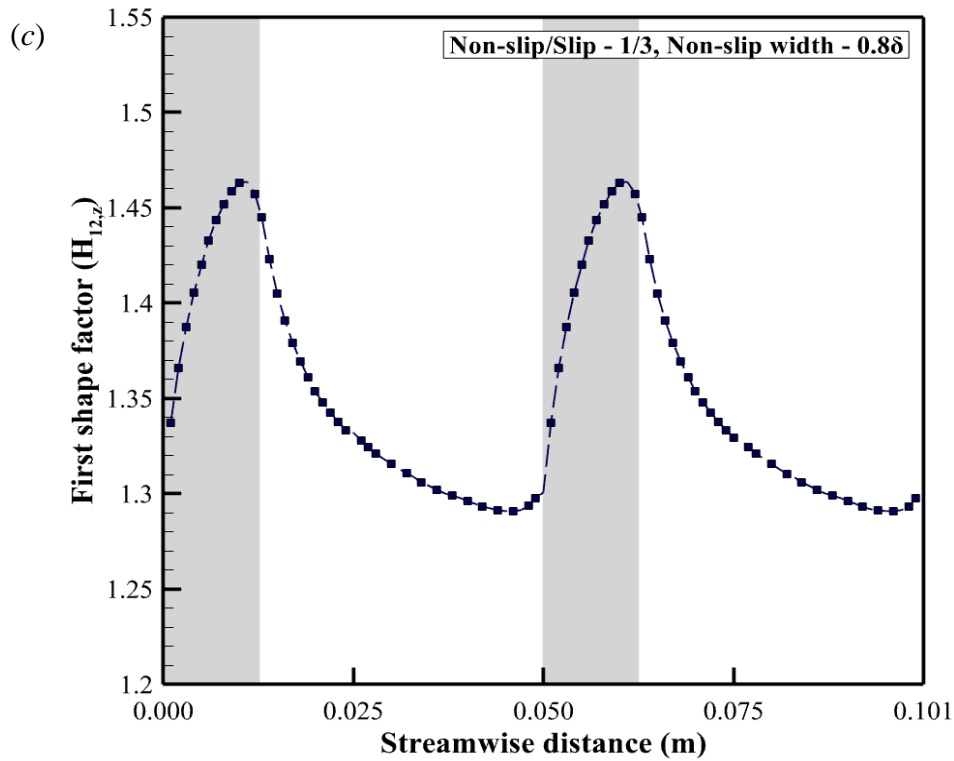


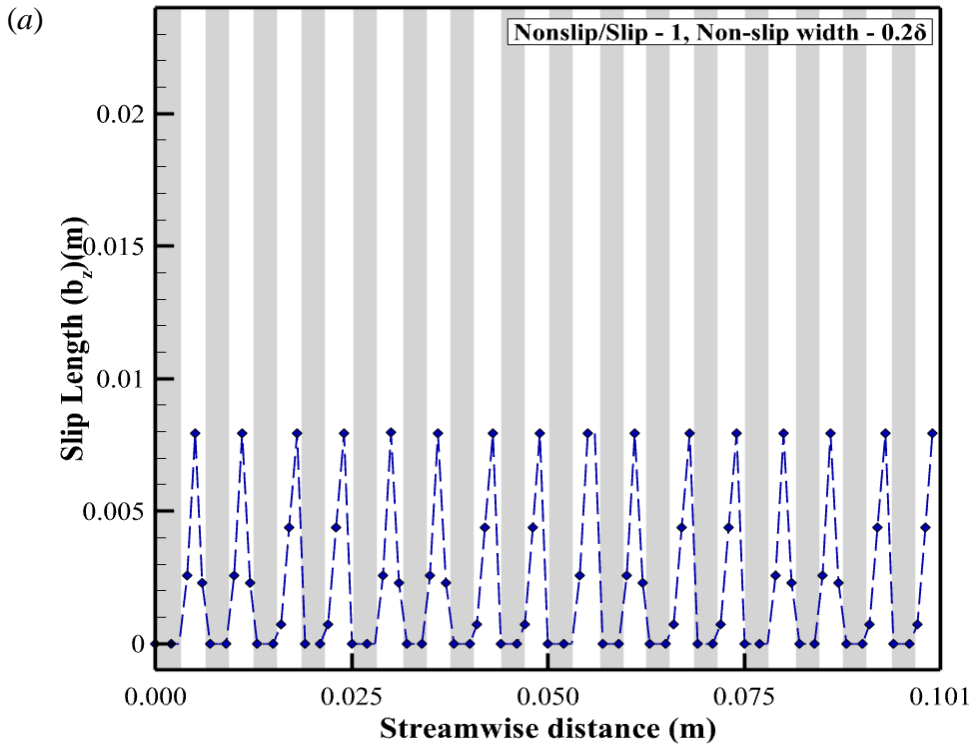
Figure 39. Local first shape factor for non-slip to slip ratio of  $1/3$  and non-slip width of (a)  $0.2\delta$ , (b)  $0.4\delta$ , (c)  $0.8\delta$

From Figure 38 and Figure 39, it can be concluded that all the non-slip/slip cases simulated had the local shape factor less than for the base case (1.63). This indicates that the boundary layer flow was more turbulent in comparison to the base case even though all the cases had a similar Reynolds number value. Also, it can be observed that the local shape factor in the slip region was less than the local shape factor in the non-slip region. The increased velocities near the wall led to an increase in turbulence in the slip region. It was also observed that, with a change in non-slip to slip ratio from 1 to  $1/3$ , the local shape factor was found to decrease. This was due to the increase in the slip region which increased the slip velocities, leading to a greater level of turbulence in the turbulent boundary layer region. For the non-slip to slip ratios, the increase in width of the bands

also led to a decrease in the first shape factor. In summary, a more turbulent boundary layer led to intensive mixing of the fluid, which helped enhance heat transfer within the minichannel section.

### 5.6 Effect of non-slip/slip bands on local slip length

The local slip length was calculated to quantify the effect of slip conditions for the non-slip/slip cases simulated. Figure 40 and Figure 41 show the local slip length profiles for the different non-slip/slip cases considered.



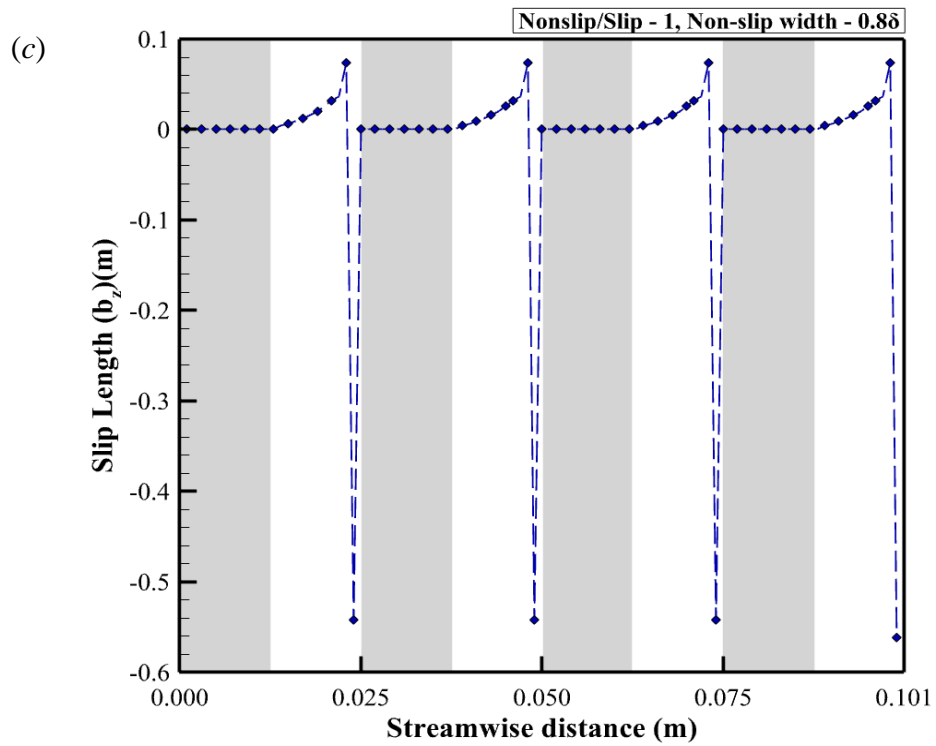
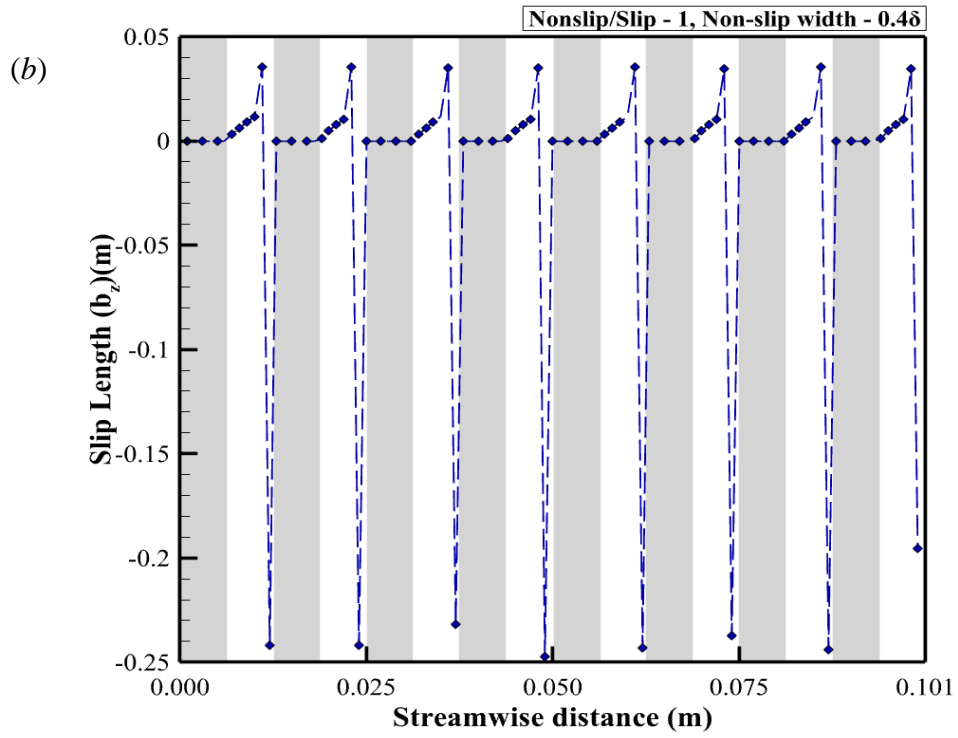
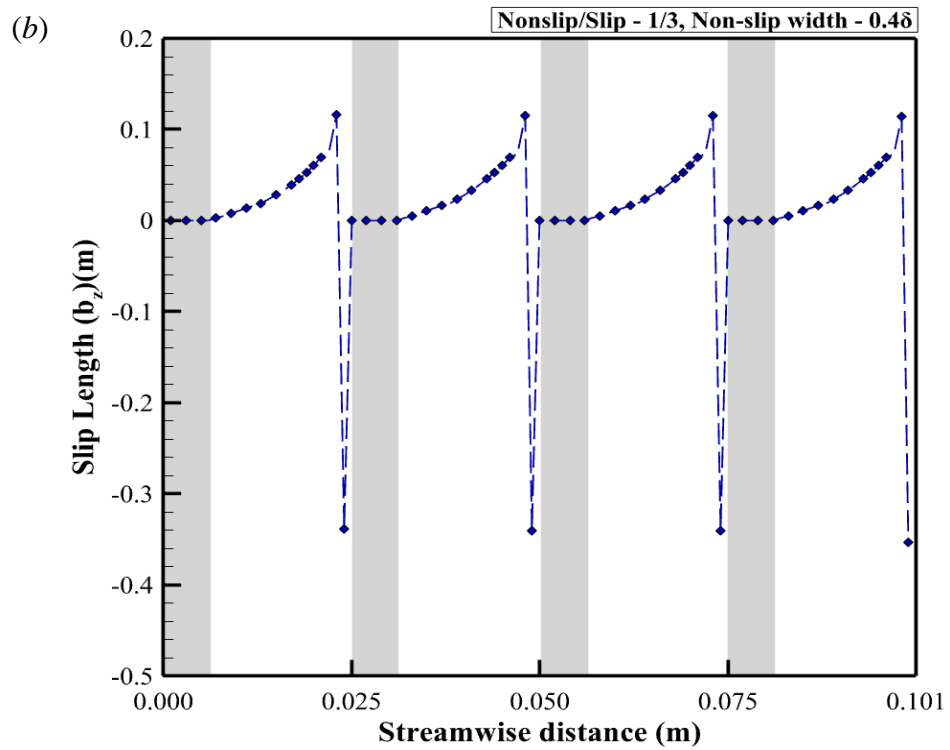
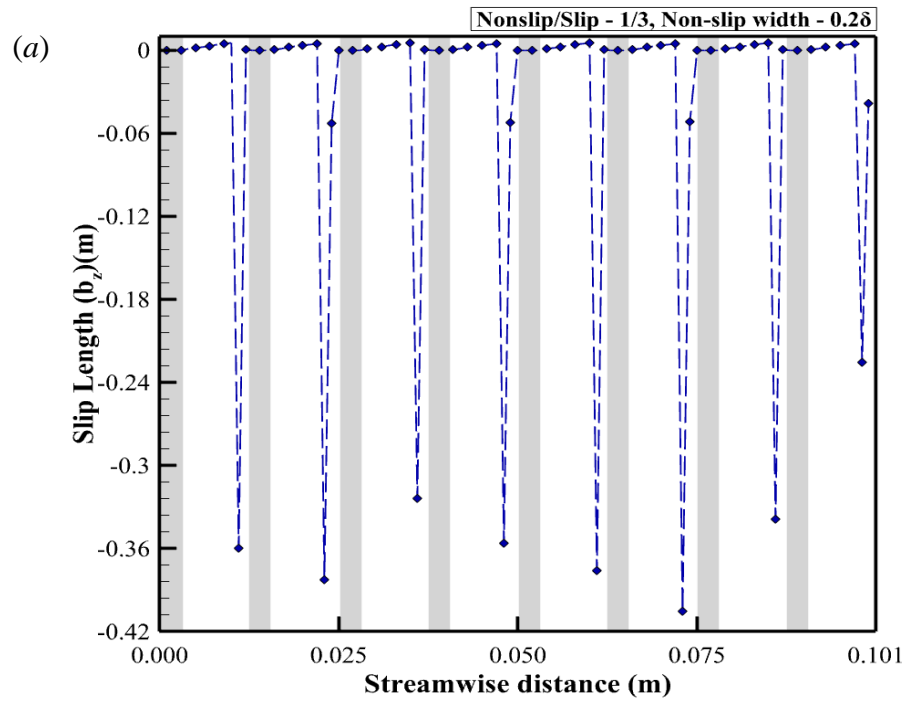


Figure 40. Local slip length for non-slip to slip ratio of 1.0 and non-slip width of (a)  $0.2\delta$ , (b)  $0.4\delta$ , (c)  $0.8\delta$



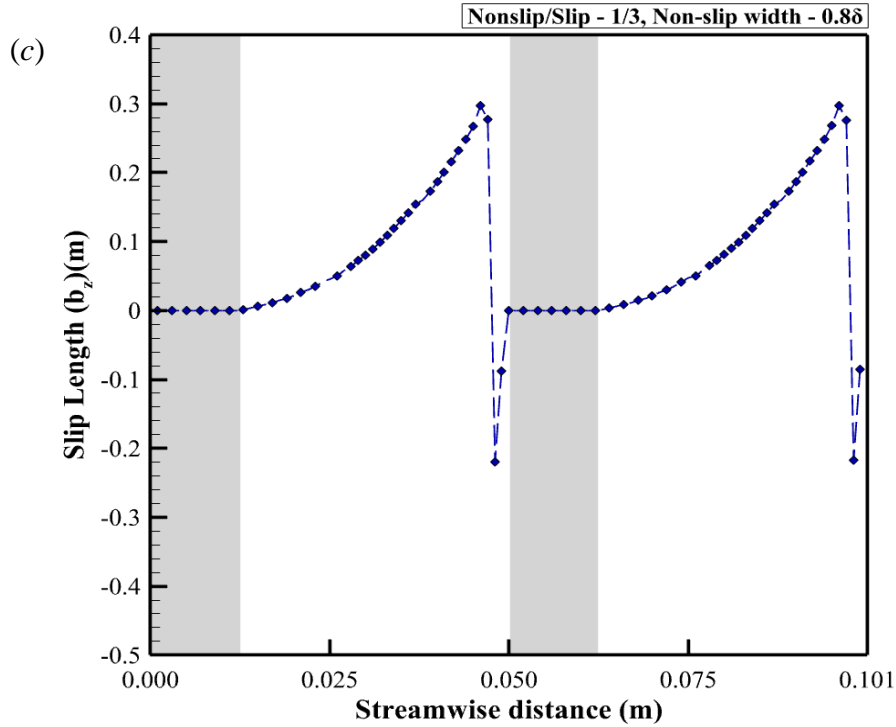


Figure 41. Local slip length for non-slip to slip ratio of 1/3 and non-slip width of (a)  $0.2\delta$ , (b)  $0.4\delta$ , (c)  $0.8\delta$

The slip length value was found to increase over the slip region for all the cases with an increase in the slip velocity. As seen in the figures, the slip length decreases dramatically when the slip velocity decreases. As the fluid approaches the non-slip surface, the slip length reaches a negative value. This implies that, near the slip to non-slip transition, the slip velocity was higher than the fluid velocity in the vicinity of the surface. Also, the change in non-slip to slip ratio from 1 to  $\frac{1}{3}$  led to an increase in slip length because of the increase in slip region.

### 5.7 Effect of non-slip/slip bands on boundary layer thickness

As discussed in Chapter III, one of the main objectives of this numerical study was to understand the effect of non-slip to slip ratio and change in width of non-slip bands on

boundary layer thicknesses. The hydrodynamic and thermal boundary layer thicknesses for the base case (non-slip walls) are shown in Figure 42.

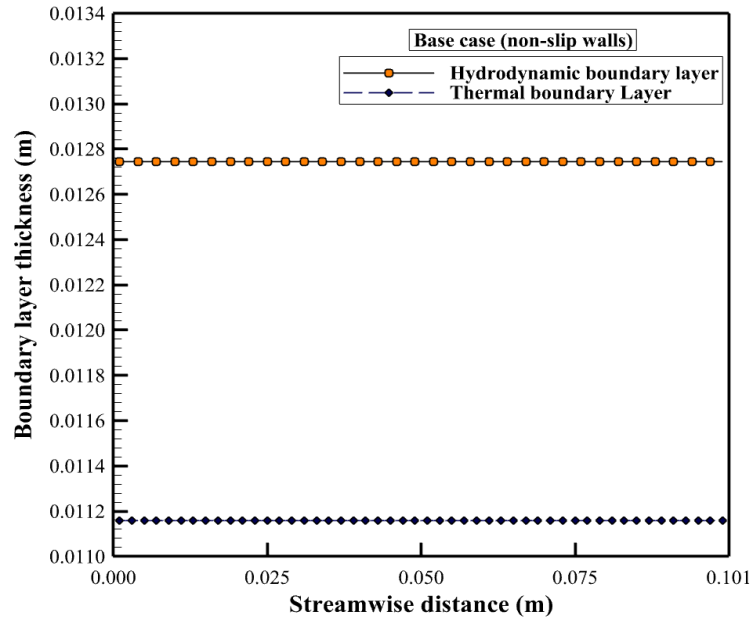
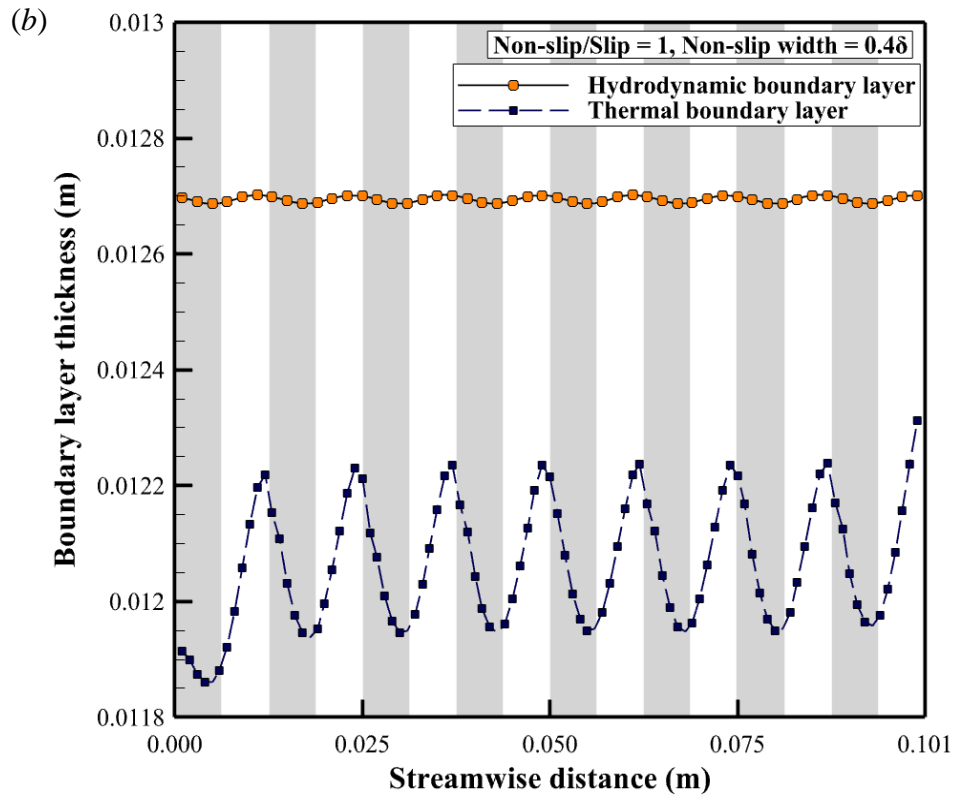
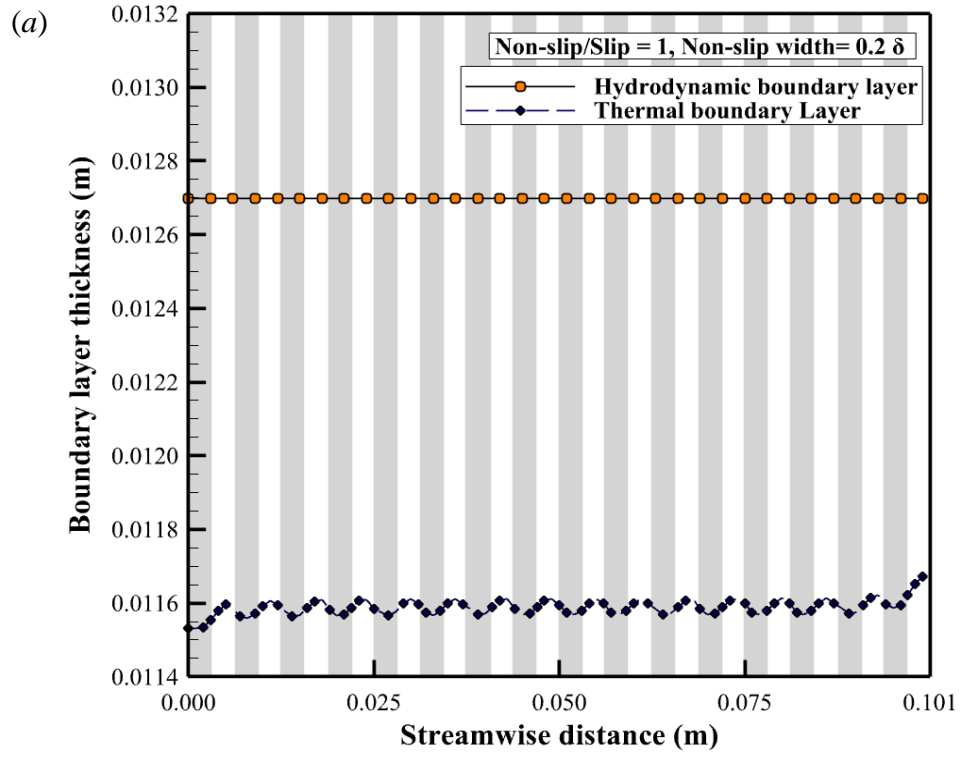


Figure 42. Boundary layer thicknesses for base case simulation

As shown in Figure 42, the thickness was found to have a constant value as the flow became thermally and hydrodynamically fully developed. The hydrodynamic boundary layer thickness was found to be greater than the thermal boundary layer thickness. This suggests that the momentum diffusivity was greater than the thermal diffusion for the base case. The following figures show the hydrodynamic and thermal boundary layers thicknesses for the different non-slip/slip cases considered. For Figure 43 (a),(b), and (c) the non-slip to slip ratio was fixed at 1 while the non-slip width was varied from  $0.2\delta$  to  $0.8\delta$ . Similarly, for Figure 44 (a),(b), and (c) the non-slip to slip ratio was fixed at  $\frac{1}{3}$ , while the non-slip width was varied from  $0.2\delta$  to  $0.8\delta$ .





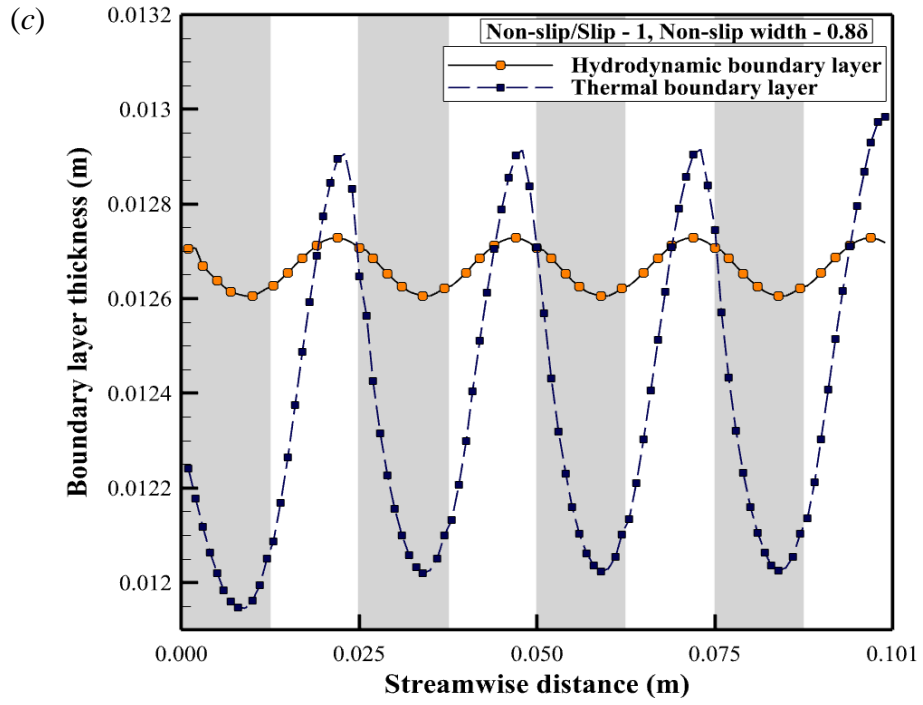
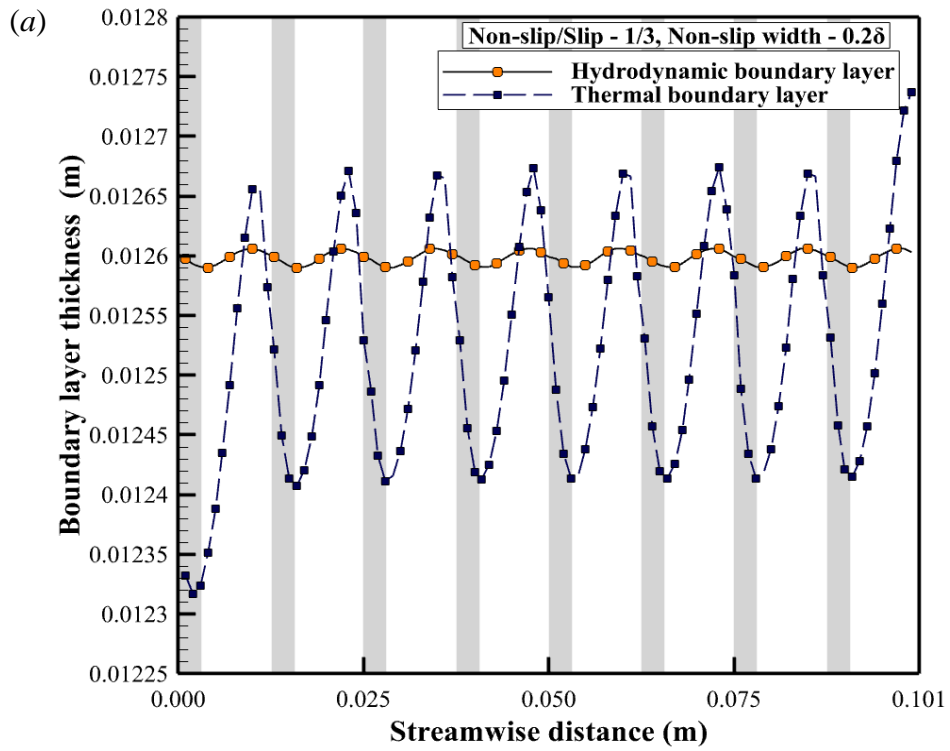


Figure 43. Boundary layer thickness for non-slip to slip ratio of 1.0 and non-slip width of (a)  $0.2\delta$ , (b)  $0.4\delta$ , (c)  $0.8\delta$



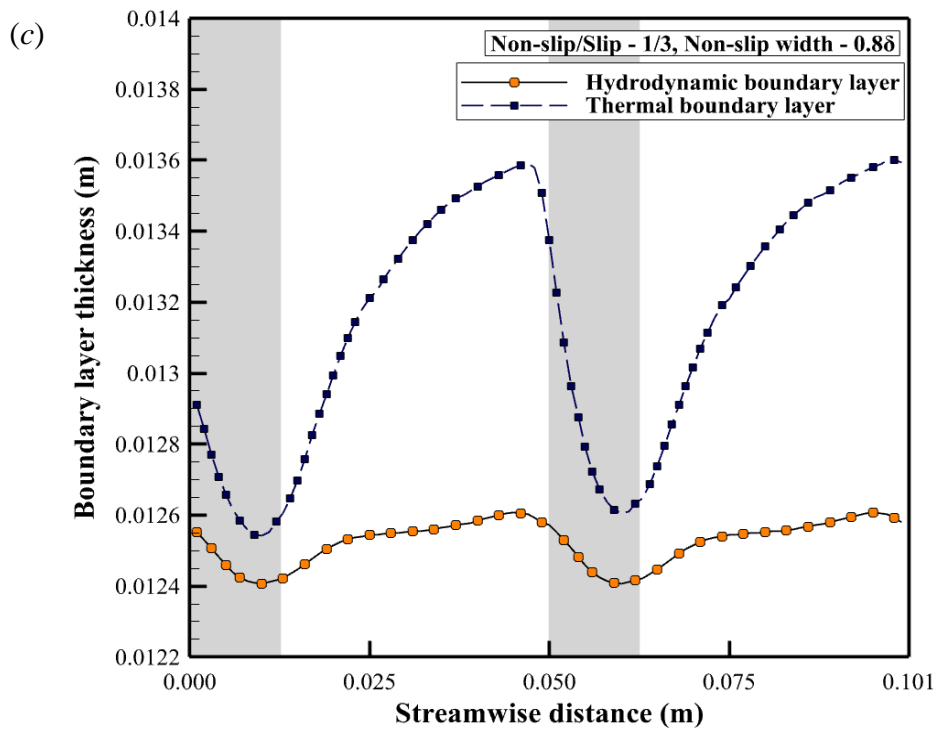
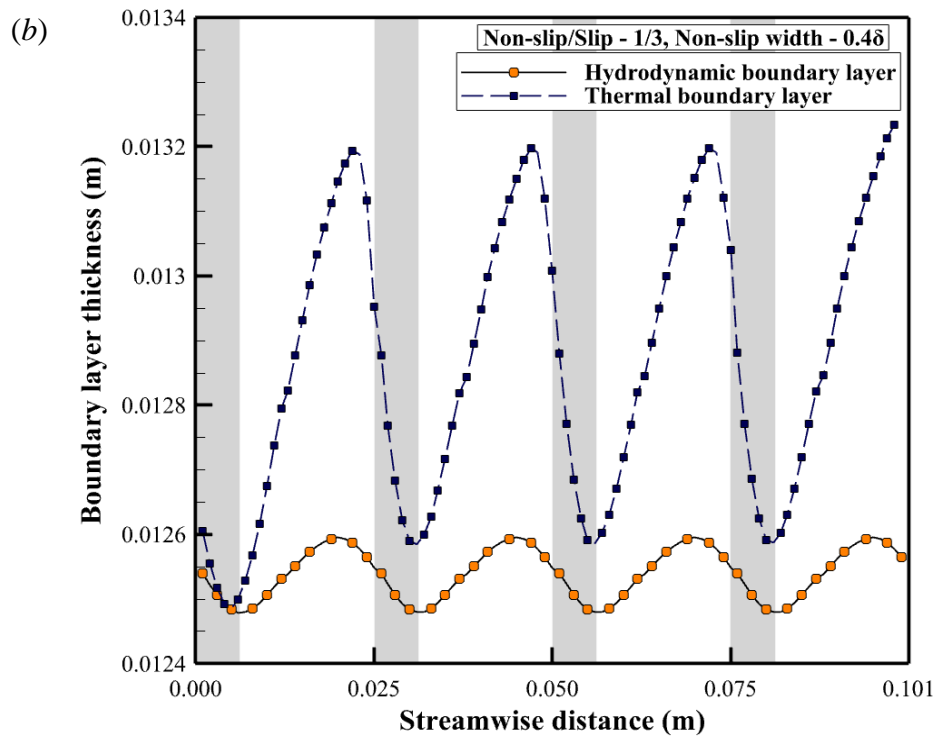


Figure 44. Boundary layer thickness for non-slip to slip ratio of 1/3 and non-slip width of (a)  $0.2\delta$ , (b)  $0.4\delta$ , (c)  $0.8\delta$

By comparing Figure 43 and Figure 44 with Figure 42, it was found that the overall hydrodynamic (velocity) boundary layer thickness had decreased for all the non-slip/slip cases simulated. This decrease can be attributed to the high slip velocity near the pipe surface, which reached about 99% of the centerline velocity closer to the wall. The decrease in hydrodynamic boundary layer thickness was found to be less for the non-slip to slip ratio of 1 when compared with the non-slip to slip ratio of  $\frac{1}{3}$ . This was due to the increased slip region for the non-slip to slip ratio of  $\frac{1}{3}$ , which led to higher slip velocities.

The overall thermal boundary layer thickness for all non-slip/cases was found to be greater than the thermal boundary layer thickness of the base case. The increase in thickness of the thermal boundary layer suggests an increase in the thermal diffusion of the fluid. This increase in thermal diffusion led to more penetration of thermal effects into the core of the fluid.

From Figure 43 (a),(b), and (c), it was observed that the increase in width of the slip region led to an increase in thermal boundary layer thickness for a fixed non-slip to slip ratio of 1. For the non-slip width of  $0.2\delta$ , the thermal boundary layer thickness was significantly smaller compared to the hydrodynamic boundary layer. However, as the non-slip width increased, the thermal boundary layer thickness increased as well. For the non-slip width of  $0.8\delta$ , the thermal boundary layer thickness was found to be greater than the hydrodynamic boundary layer thickness in the slip region.

For the fixed non-slip to slip ratio of  $\frac{1}{3}$ , the thermal boundary layer thickness increased with an increase in slip width. This was attributed to the fact that the increase in slip width increased the slip velocity near the surface. This increase near-wall velocity

enabled greater heat dissipation, thus allowing the effects of the wall heat flux to be felt in the core regions of the fluid. The thermal boundary layer was thicker than the hydrodynamic boundary layer for the non-slip width of  $0.4\delta$  and  $0.8\delta$ .

To explore the effect of change in the sequence of non-slip/slip bands, a case was simulated in which the last slip band was split into two equal parts. One of the two parts was added near the inlet of the pipe, while the other one at the outlet. Figure 45 shows the geometry used for this simulation. Non-slip to slip ratio of  $1/3$  and non-slip width of  $0.4\delta$  were chosen for this case, since it had shown the maximum difference between the inlet and outlet thermal boundary layer thickness values, when compared with the main domain thermal boundary layer thickness values.

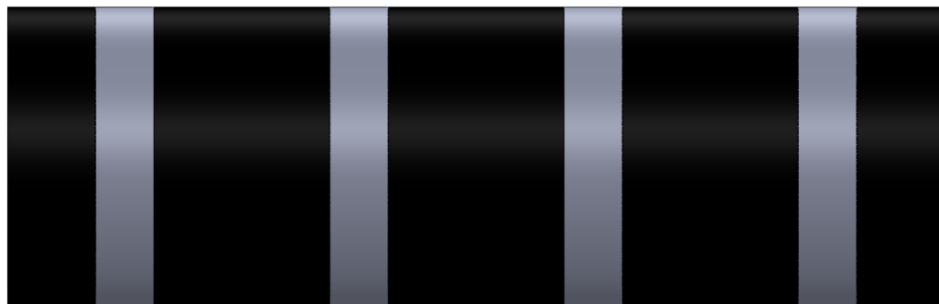


Figure 45. Geometry with slip (black) and non-slip (grey) bands for the case with slip surface at the inlet

Figure 46 shows the thermal boundary layer thickness plot for the geometry shown in Figure 45. The grey region represents the slip region, and the white region represents the non-slip region.

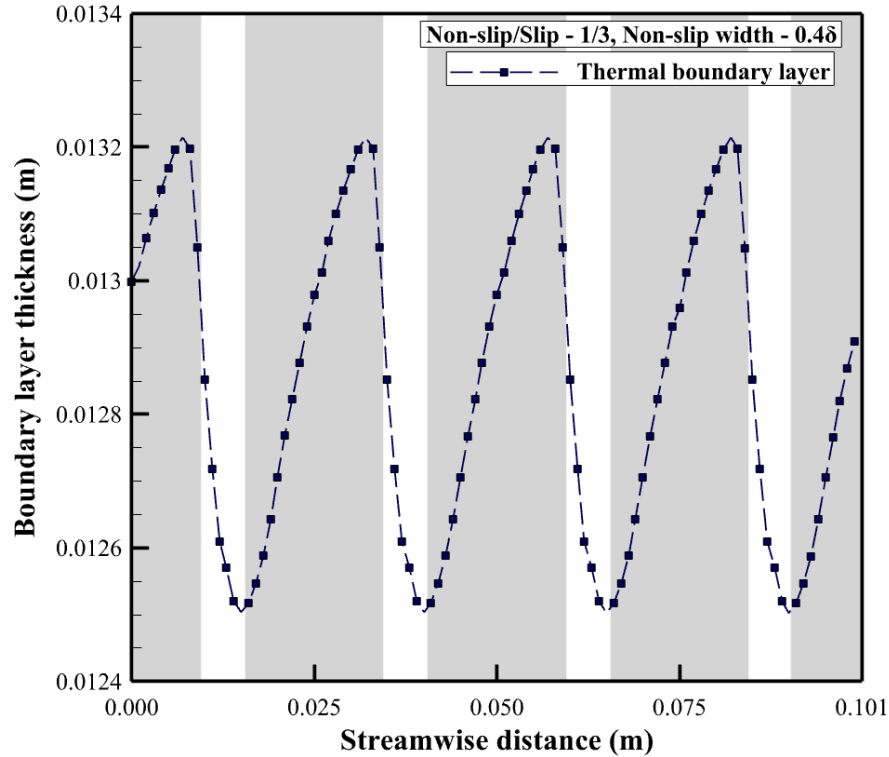


Figure 46. Thermal boundary layer thickness for non-slip to slip ratio of 1/3 and non-slip width of  $0.4\delta$  for the case with slip surface at the inlet

From Figure 46, it can be inferred that:

1. The change in the sequence of the bands has an impact on the thermal boundary layer thickness values.
2. Previously, starting with a non-slip band led to different thermal boundary layer thickness values near the inlet and outlet of the pipe when compared with the main domain regions. However, for this case, it is evident from the figure that the values are consistent throughout the domain.
3. The thermal boundary layer thickness was found to vary between the two values as seen in previous cases.

- In comparison to the previous cases, which had a non-slip band at the inlet, both cases had similar highest values for thermal boundary layer thickness. The lowest thermal boundary layer thickness value was for the current case is within 1% of the previous case.

### 5.8 Effect of non-slip/slip bands on local Nusselt number ( $Nu_z$ ) and local convective heat transfer coefficient ( $h_z$ ) and PEC

The thermal performance effect of slip, non-slip surfaces was analyzed by evaluating  $h_z$  and  $Nu_z$  for all the six cases considered in this study. Figure 47 shows the variation of  $h_z$  and  $Nu_z$  with streamwise distance for the base case (non-slip walls).

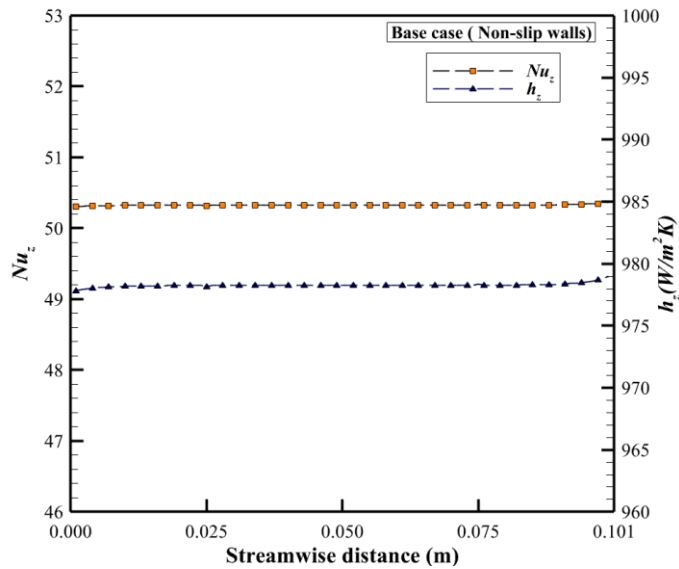
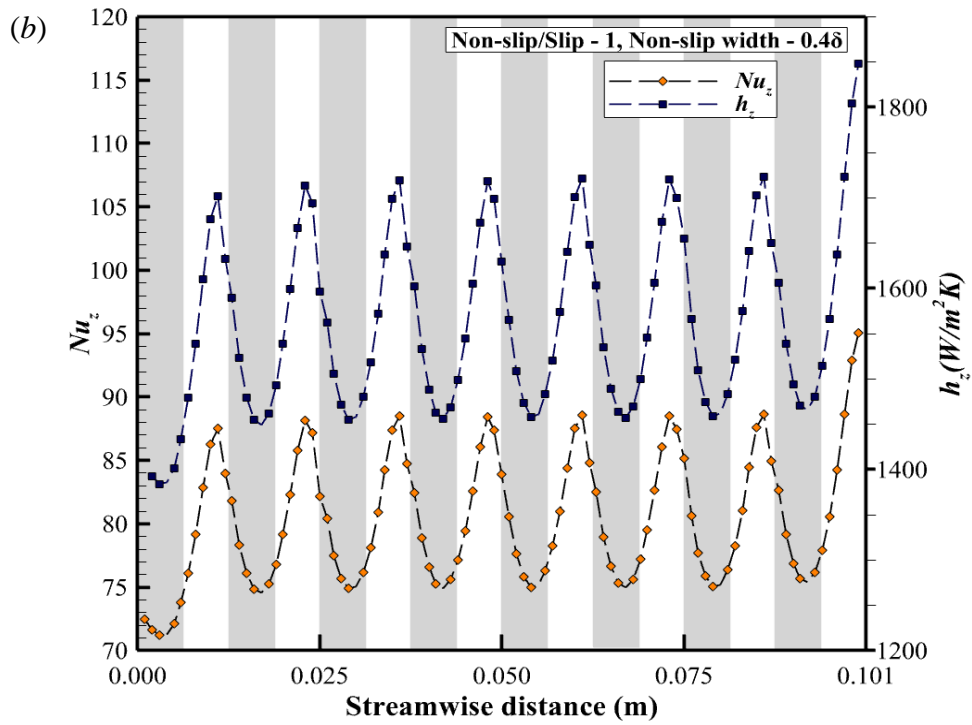
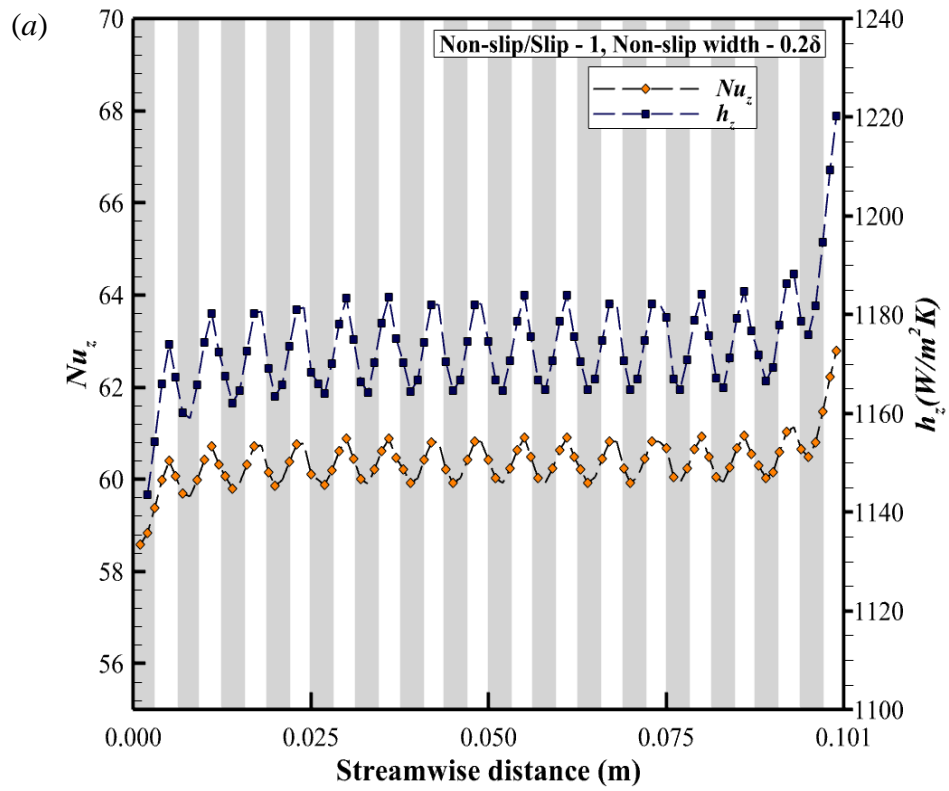


Figure 47.  $h_z$  and  $Nu_z$  variation with respect to streamwise distance for base case with non-slip walls

This case referred to the base case with only non-slip walls, thus the  $h_z$  and  $Nu_z$  were found to be constant. Figure 48 and Figure 49 show the different non-slip/slip cases considered.



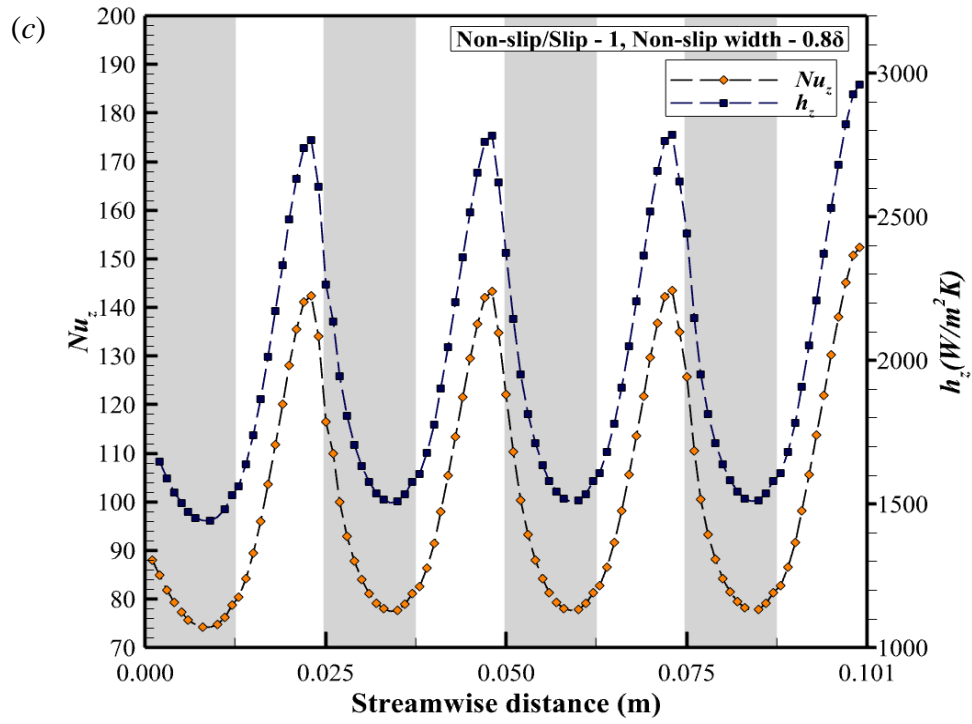
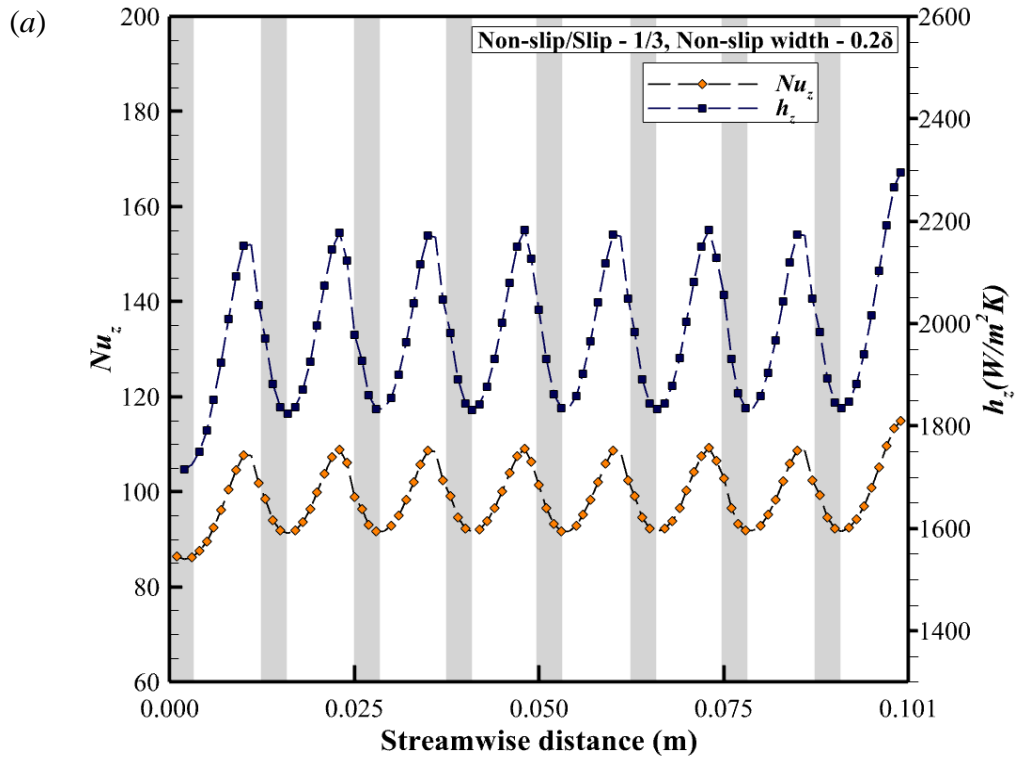


Figure 48.  $h_z$  and  $Nu_z$  values for non-slip to slip ratio of 1 and non-slip width of (a)  $0.2\delta$ , (b)  $0.4\delta$ , (c)  $0.8\delta$





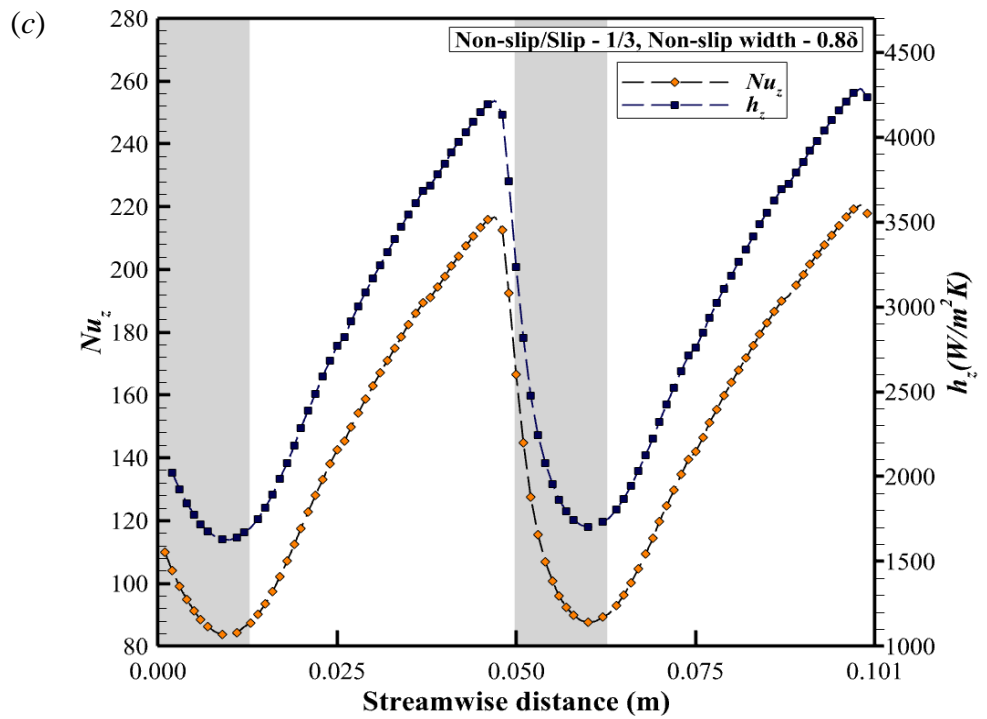
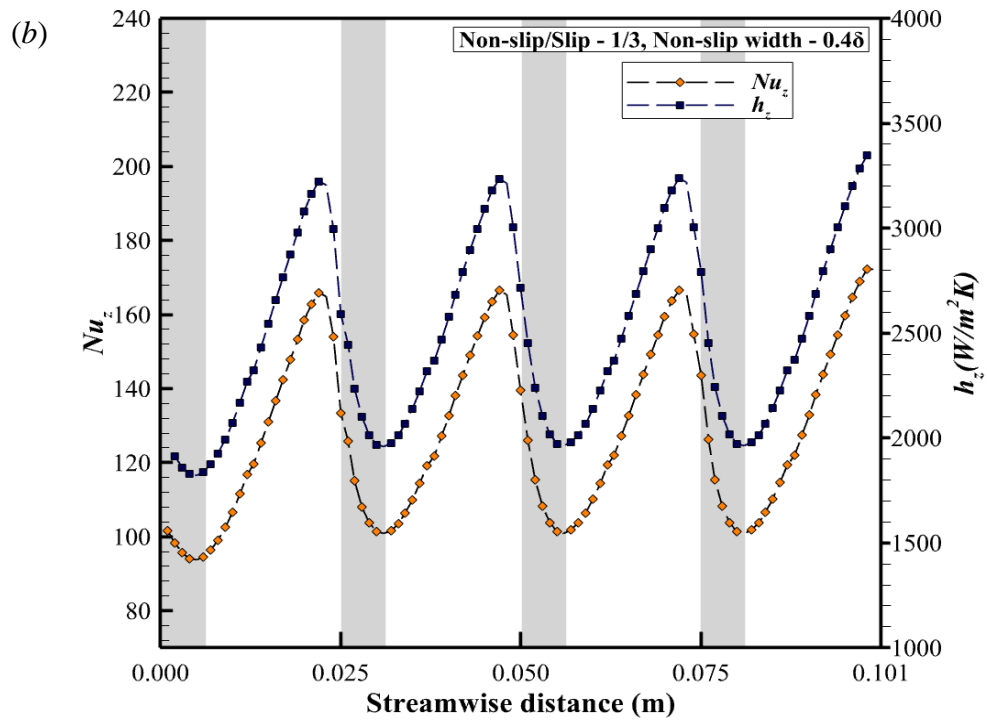


Figure 49.  $h_z$  and  $Nu_z$  values for non-slip to slip ratio of 1/3 and non-slip width of (a)  $0.2\delta$ , (b)  $0.4\delta$ , (c)  $0.8\delta$

For all the non-slip/slip cases, it was found that the  $h_z$  and  $Nu_z$  were higher in comparison to the base case. The higher value of  $Nu_z$  indicates the presence of greater convection in the non-slip/slip cases. For the fixed non-slip to slip ratio 1, the increase in width of the non-slip band led to an increase in  $h_z$  and  $Nu_z$  in the slip and non-slip region. This was also found to be true for the non-slip to slip ratio of  $\frac{1}{3}$ . The increase in width of bands led to an increase in convective heat transfer because of the fluid slip, which enhanced fluid mixing. The fluid mixing led to enhanced heat transfer into the core of the fluid. Also, at the end of the slip region, the fluid velocity decreases causing the heat transfer to diminish and thus leading to a decrease in the Nusselt number. This can be seen in all the non-slip/slip cases. Change in non-slip/slip ratio from 1 to  $\frac{1}{3}$ , while keeping the width of the non-slip region constant also led to an increase in Nusselt number. With the change in the non-slip to slip ratio, the length of the slip region was increased, which led to higher slip velocities and an increase in heat transfer.

The following table shows the average Nusselt number and maximum and minimum of Nusselt number values obtained for all the non-slip/slip cases simulated in this study. Also, the percentage change in Nusselt number in comparison with the base case has been provided in the table. Columns 2 and column 3 show the values of the non-slip to slip ratio and the width of non-slip bands considered for each configuration.

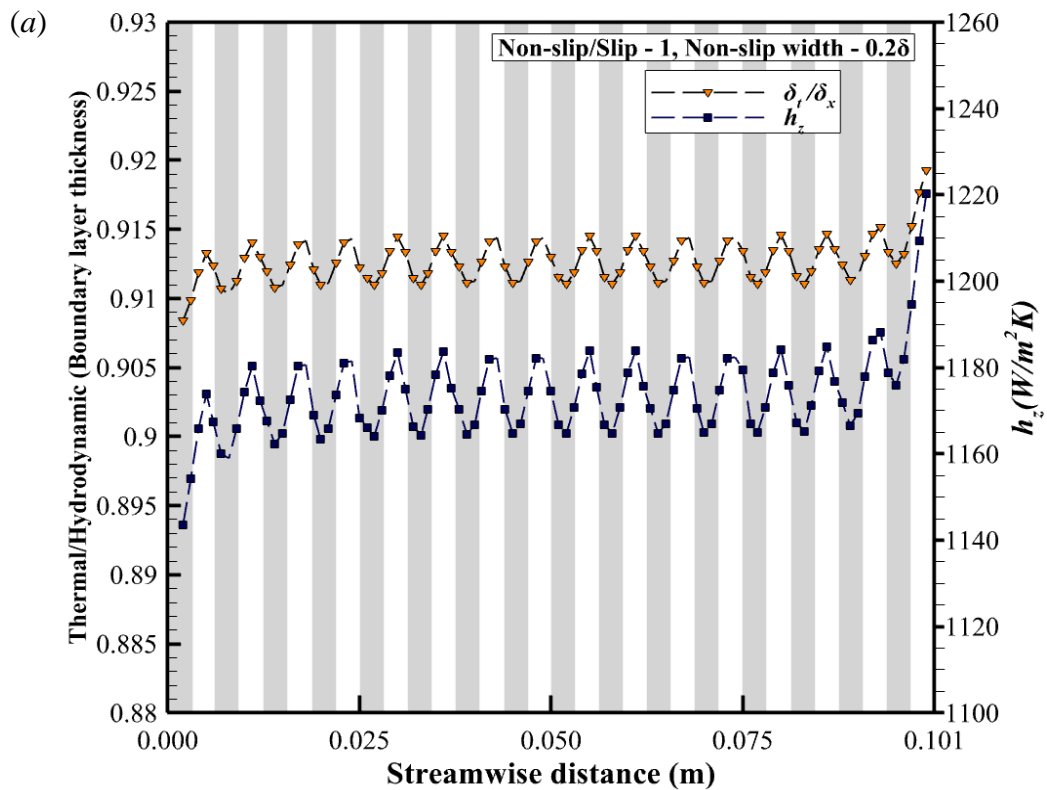
**Table 20. Nusselt number values for the non-slip/slip case simulated**

<b>Configura tion</b>	<b>Nonslip/Slip (a)/(b) ratio in minichannel</b>	<b>Width of non-slip band, <math>a</math>, in minichannel</b>	<b>Average Nusselt number</b>	<b>Nusselt number range</b>	<b>% increase in Nusselt number</b>
1 (Base case)	-	-	50.78	-	-
2	1:1	$0.2\delta$	60.34	58.14 - 62.78	18.8
3	1:1	$0.4\delta$	80.29	71.18 - 95.06	58.1
4	1:1	$0.8\delta$	100.49	74.16 - 152.31	97.8
5	1:3	$0.2\delta$	98.73	85.81 - 114.80	94.4
6	1:3	$0.4\delta$	128.08	93.67 - 172.11	152.2
7	1:3	$0.8\delta$	145.78	83.68 - 220.48	334.1

From Table 20, it is clear that the average Nusselt number for all the non-slip/slipcases simulated was greater than the base case Nusselt number. Also, it can be observed that the minimum Nusselt number for non-slip/slip cases simulated was greater than the base case Nusselt number. This suggests that the addition of the slip surface increases the Nusselt number in the slip as well as in the non-slip region. For the fixed non-slip to slip ratio of 1, the average, minimum, and maximum Nusselt number increase with the increase in width of the bands. For the non-slip to slip ratio of 1/3, the average and the maximum Nusselt number were found to increase with an increase in the width of the bands. However, the minimum Nusselt number was found to be the lowest for the largest width size of  $0.8\delta$ . Thus, if the aim was to increase the average Nusselt number, then the case with a non-slip to slip ratio of 1/3 and width size of  $0.8\delta$  should be considered in future studies. However, if the aim was to increase the minimum Nusselt number of a

system, then the case with a non-slip to slip ratio of  $1/3$  and width size of  $0.4\delta$  should be considered in future studies.

In the following figures, the thermal/hydrodynamic boundary layer ratio ( $\delta_t/\delta_x$ ) and local convective heat transfer coefficient ( $h_z$ ) are plotted for all the non-slip/slip cases to check for any dependence between both variables. For Figure 50 (a),(b) and (c) the non-slip/slip ratio was fixed at 1 whereas the non-slip width varied from  $0.2\delta$  to  $0.8\delta$ . For Figure 51 (a),(b) and (c) the non-slip/slip ratio was fixed at  $1/3$ .



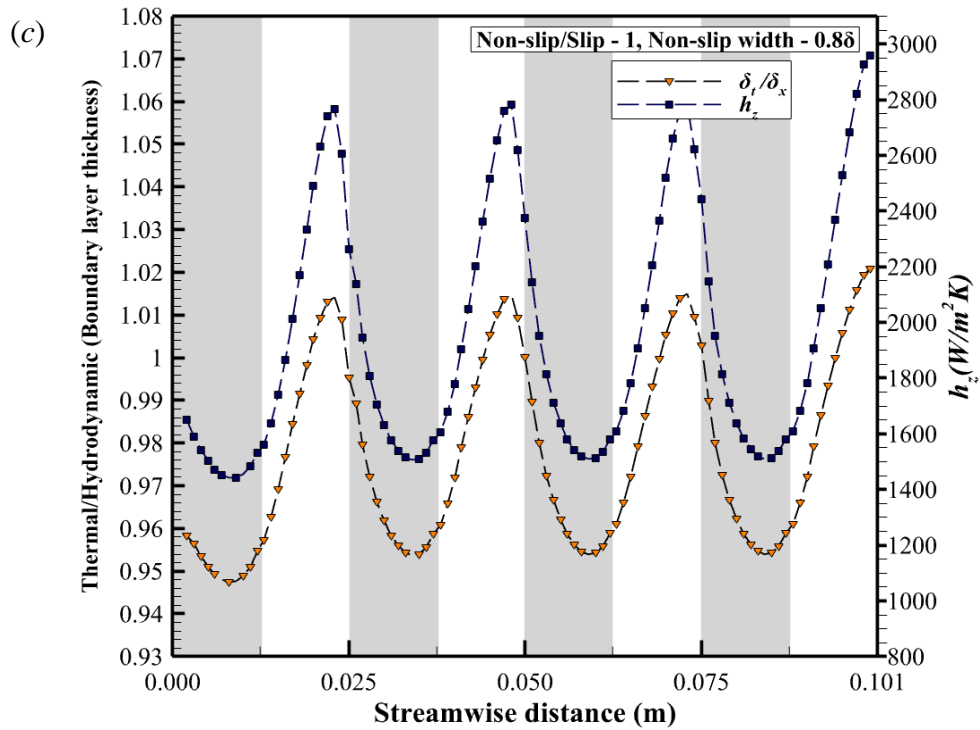
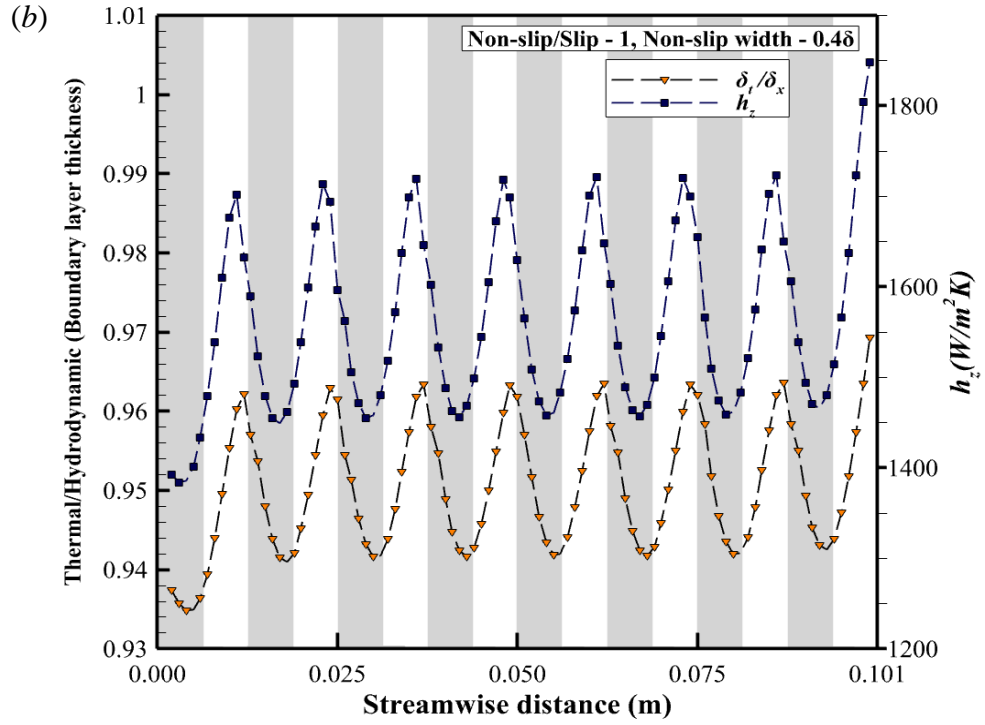
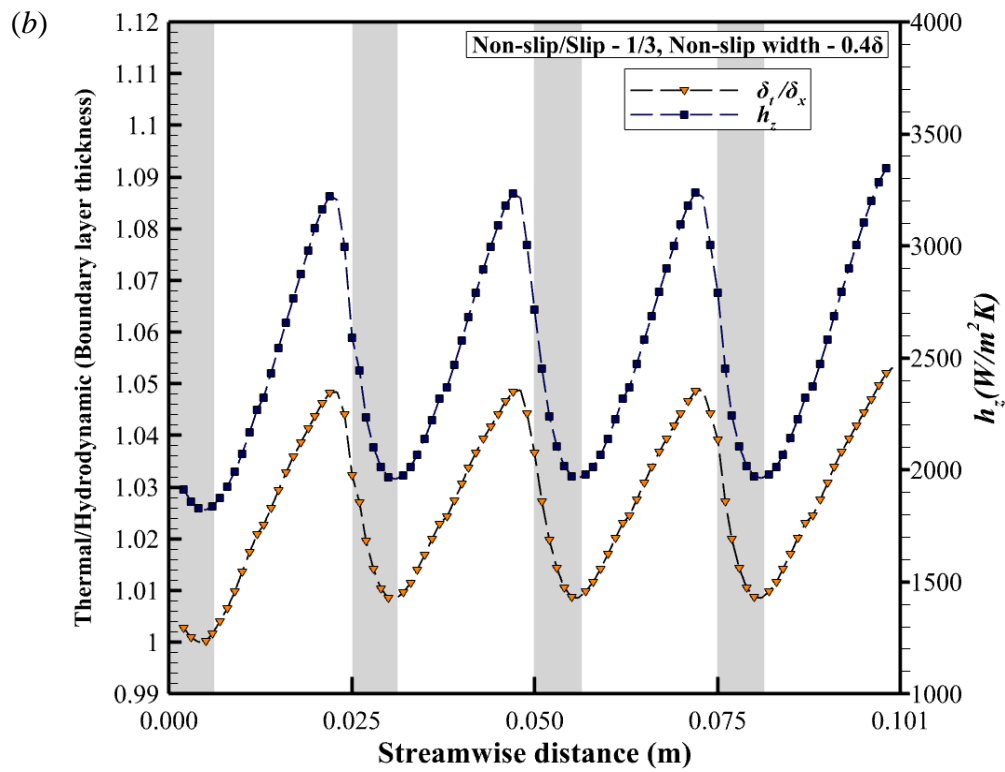
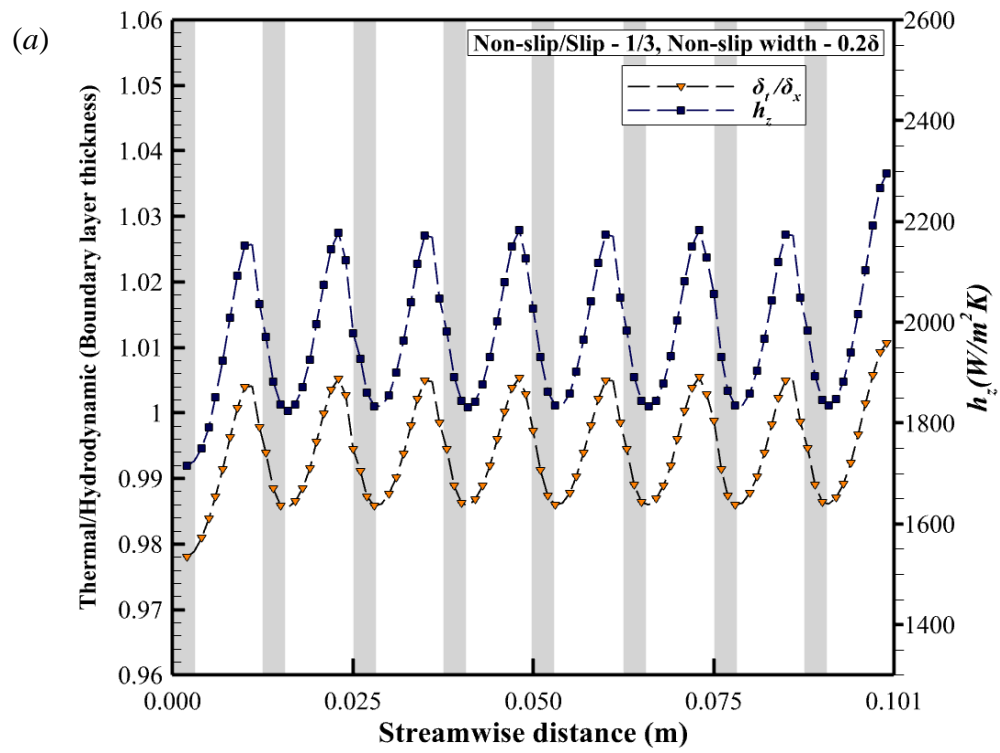


Figure 50.  $\delta_t/\delta_x$  and  $h_z$  values for non-slip to slip ratio of 1.0 and non-slip width of (a)  $0.2\delta$ , (b)  $0.4\delta$  and (c)  $0.8\delta$



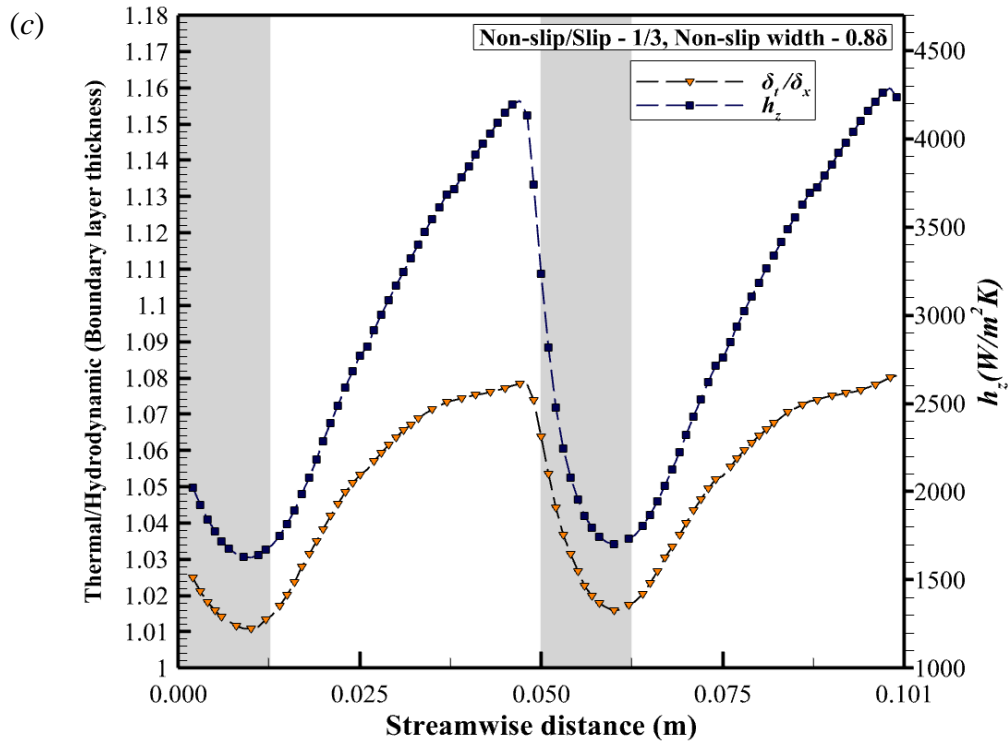


Figure 51.  $\delta_t/\delta_x$  and  $h_z$  values for non-slip to slip ratio of 1/3 and non-slip width of (a)  $0.2\delta$ , (b)  $0.4\delta$  and (c)  $0.8\delta$

From Figure 50 and Figure 51, it is evident that the  $h_z$  profile has the same shape and trend as  $\delta_t/\delta_x$  curves for all the non-slip/slip cases used in this numerical study. Thus, there is a strong influence of  $\delta_t/\delta_x$  on heat transfer within the minichannel. Also, the  $\delta_t/\delta_x$  and  $h_z$  were found to decrease in the non-slip region. In the slip region, with an increase in slip velocity, which leads to an increase in heat transfer, the  $\delta_t/\delta_x$  ratio and  $h_z$  were found to increase as well. It was also observed that in the cases with non-slip to slip ratio of 1/8, the  $\delta_t/\delta_x$  values were greater than 1, indicating a thicker thermal boundary layer in comparison with the hydrodynamic boundary layer. In such cases, the  $h_z$  was found to increase at a higher rate in comparison to cases with  $\delta_t/\delta_x$  less than 1.

### ***Performance Evaluation Criterion (PEC)***

To understand the combined effect of non-slip to slip ratio and slip band width on thermal performance, the performance evaluation criterion (PEC) was calculated for all the nonslip/slip cases. If the surface was able to increase heat transfer and/ or reduce friction factor in comparison to the base case, then the PEC should be greater than 1. Table 21 shows the PEC values for all the configurations considered in the numerical study.

**Table 21. Nusselt number, friction factor, and PEC values for different configurations for Re of 5600**

<b>Configuration</b>	<b>Non-slip/slip ratio</b>	<b>Width of non-slip band</b>	<b>Nusselt number</b>	<b>Friction factor</b>	<b>PEC</b>
Base Case (1)	-	-	50.78	0.0391	-
2	1	0.2 $\delta$	60.34	0.0360	1.22
3	1	0.4 $\delta$	80.29	0.0359	1.62
4	1	0.8 $\delta$	100.49	0.0348	2.05
5	1/3	0.2 $\delta$	98.73	0.0308	2.10
6	1/3	0.4 $\delta$	128.08	0.0277	2.82
7	1/3	0.8 $\delta$	145.78	0.0235	3.39

It is evident from the table that all the non-slip/slip cases simulated produced a PEC value greater than 1. Configuration 7 was found to be the most effective while configuration 2 was found to be least effective in thermal performance enhancement. Configuration 2 is characterized by having the smallest non-slip width of 0.2 and a non-slip/slip ratio of 1. In this case, the slip region was considerably less compared to other cases, thus resulting in minimal slip velocity and minimal heat transfer.



### 5.9 Effect of Reynolds number on the thermal performance of circular minichannel

The effect of distinct Reynolds number values (laminar and turbulent) on two different cases have been studied. The two cases considered in this study correspond to the non-slip/slip configurations with the highest and the lowest PEC values, respectively. Simulations were carried out for Reynolds numbers of 500 and 5600 in the laminar and turbulent flow regimes, respectively.

Table 22 shows the comparison of the Nusselt number, friction factor, and PEC value for the two different Reynolds number cases simulated.

**Table 22. Nusselt number, friction factor, and PEC values**

Configuration	Reynolds number - 500			Reynolds number- 5600		
	Nu	Friction factor	PEC	Nu	Friction factor	PEC
Base Case	4.36	0.128	-	50.78	0.0391	-
Non-slip/slip - 1 Non-slip width – $0.2\delta$	5.5	0.127	1.26	60.34	0.0360	1.22
Non-slip/slip - 1/3 Non-slip width – $0.8\delta$	6.65	0.082	1.76	145.78	0.0235	3.39

From Table 22, it is evident that the Reynolds number has an impact on the thermal performance of the minichannel. For the non-slip to slip ratio of 1 and a non-slip width of  $0.2\delta$ , the PEC values obtained for Reynolds numbers of 500 and 5600 were almost identical. However, for the non-slip to slip case of 1/3 with a non-slip width of  $0.8\delta$ , a higher Reynolds number (i.e., 5600) has a greater effect on thermal performance than at a

lower Reynolds number (i.e., 500). Figure 52 shows the relative slip velocity for the two cases considered.

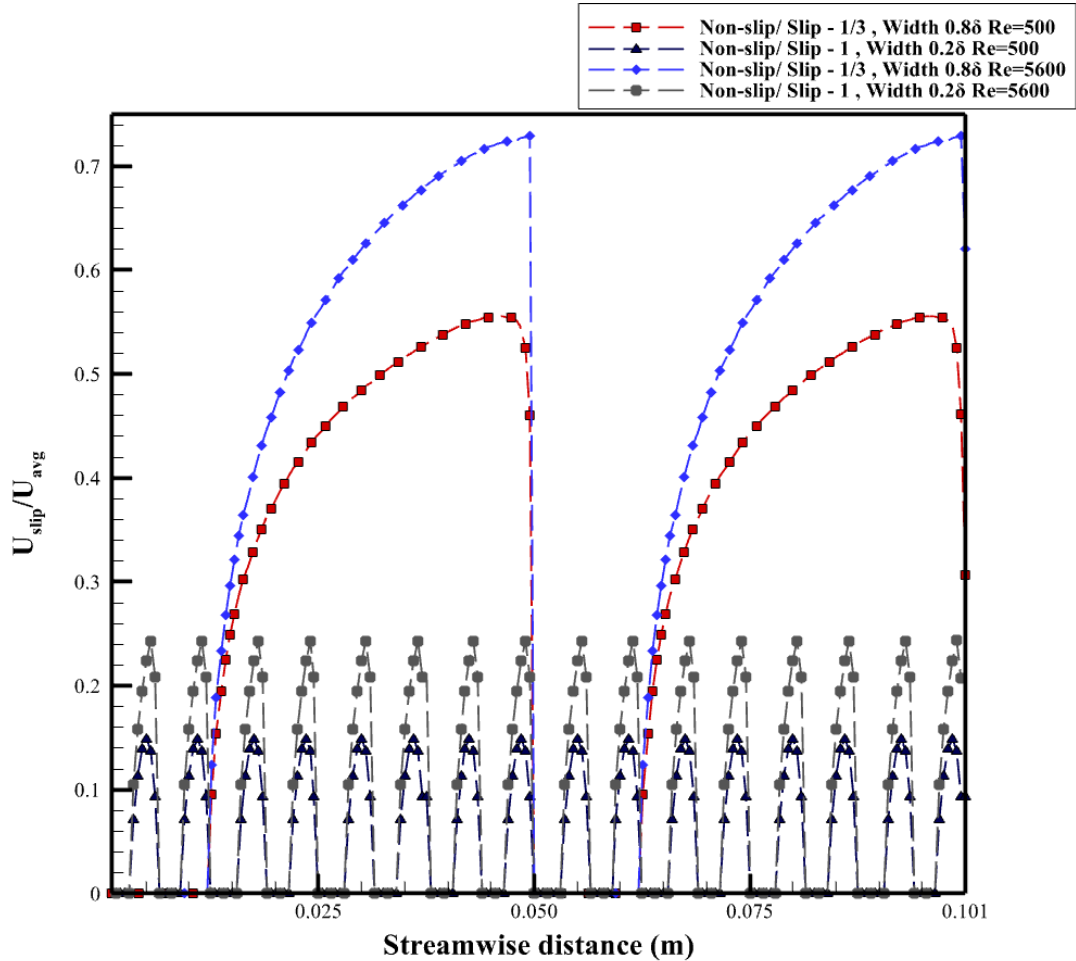


Figure 52. Relative slip velocity for the two non-slip/slip cases

It is evident from the figure that for both the cases, the laminar regime led to a lower relative slip velocity in comparison to the turbulent regime. The reason for this could be the high viscous forces present in the laminar flow regime, which prevents the fluid flow from slipping further near the slip wall. The following table shows the Nusselt number values for the above cases.

**Table 23. Nusselt number for laminar and turbulent flow cases**

<b>Reynolds Number</b>	<b>Non-slip/slip -1 Non-slip width - <math>0.2\delta</math></b>	<b>Non-slip/slip -1/3 Non-slip width - <math>0.8\delta</math></b>	<b>% Change at same Reynolds Number</b>
500	5.5	6.657	20.1
5600	60.34	145.78	141.59

**Table 24. Pressure Drop for laminar and turbulent flow cases**

<b>Reynolds Number</b>	<b>Non- Slip/slip -1 Non-slip width - <math>0.2\delta</math></b>	<b>Non-slip/slip -1/3 Non-slip width - <math>0.8\delta</math></b>	<b>% Change at same Reynolds Number</b>
500	0.035	0.023	34.2
5600	1.26	0.82	34.9

It is clear from Table 23 and Table 24 that the Reynolds number has a significant effect on the thermal performance of the circular minichannel.

## CHAPTER VI

### CONCLUSION AND SCOPE FOR FUTURE WORK

#### 6.1 Conclusion

The main objective of this numerical study was to understand the effect of non-slip/slip ratio and width of non-slip bands on pressure drop and thermal performance for a circular minichannel. This was achieved by simulating the flow through the minichannel by considering two non-slip to slip ratios (1 and 1/3) and 3 different non-slip widths ( $0.2\delta$ ,  $0.4\delta$  and  $0.8\delta$ ). The important findings related to the present study are as follows:

- Effect on pressure drop – The reduction in pressure drop was found to increase with a reduction in non-slip to slip ratio from 1.0 to 1/3. Also, it was observed that as the non-slip width increased, the reduction in pressure drop increased. Thus, the configuration with a non-slip to slip ratio of 1/3 and width of  $0.8\delta$  showed a 40% reduction in pressure drop when compared with the base case.
- Effect on slip velocity – The change in non-slip to slip ratio from 1 to 1/3 led to an increase in slip velocity. Also, the change in width from  $0.2\delta$  to  $0.8\delta$  was found to increase the slip velocity. A maximum relative slip velocity of 0.8 was achieved for the configuration with a non-slip to slip ratio of 1/3 with non-slip width of  $0.8\delta$ .
- Effect on boundary layer thickness – The increase in slip velocity with a decrease in non-slip ratio from 1 to 1/3 caused the hydrodynamic boundary layer to decrease. Also, the same effect was noted when the non-slip width was increased

from  $0.2 \delta$  to  $0.8\delta$ . The thermal boundary layer thickness was found to be greater for all the non-slip/slip cases simulated in comparison to the base case.

- Effect on Nusselt number and PEC – The average Nusselt number was found to increase with a decrease in the non-slip to slip ratio. Also, the increase in non-slip width increased the average Nusselt number value. Another important finding related to the Nusselt number was that the minimum value of the Nusselt number increased with an increase in width of non-slip bands for the non-slip to slip ratio of 1. However, this was not found to be true for the non-slip to slip ratio of 1/3. PEC was used to quantify the enhancement in terms of friction factor and Nusselt number. The PEC value showed an increase with a decrease in non-slip to slip ratio and with an increase in non-slip band width.

Thus, it can be concluded that enhancement of thermal performance in turbulent regime is the combined effect of non-slip to slip ratio and width of non-slip bands.

## **6.2 Scope for future work**

The work conducted for this thesis helped identify opportunities for future studies involving minichannels, as follows:

- CFD simulations should consider small-scale air cavities to account for slip surfaces to better understand the superhydrophobic surface phenomena and their thermal performance effects.
- Experimental work should be conducted to validate the results shown in this numerical study.

- Numerical optimization of non-slip to slip ratio and non-slip width bands should be conducted to identify the best combination of both variables to achieve the best thermal performance of minichannels.
- The effect of different types of ridge geometries on thermal performance should be explored in future studies as well.

## REFERENCES

1. Shien, E (2017, April 17). *Moore's Law turns 55: Is it still relevant?* TechRepublic. <https://www.techrepublic.com/article/moores-law-turns-55-is-it-still-relevant/>
2. Lawrence, A (2020, December 7). *Rack Density is Rising*. Uptime Institute. <https://journal.uptimeinstitute.com/rack-density-is-rising/>
3. Bar-Cohen, A., Kraus, A. D., & Davidson, S. F. (1983). Thermal frontiers in the design and packaging of microelectronic equipment. *Mech Engr*, 105(6), 53-59.
4. Singhal, V., Garimella, S. V., & Raman, A. (2004). Microscale pumping technologies for microchannel cooling systems. *Appl. Mech. Rev.*, 57(3), 191-221.
5. Stone, H. A., Stroock, A. D., & Ajdari, A. (2004). Engineering flows in small devices: microfluidics toward a lab-on-a-chip. *Annu. Rev. Fluid Mech.*, 36, 381-411.
6. Cheng, Y., Xu, J., & Sui, Y. (2015). Numerical study on drag reduction and heat transfer enhancement in microchannels with superhydrophobic surfaces for electronic cooling. *Applied Thermal Engineering*, 88, 71-81.
7. Cui, J., & Fu, Y. (2012). A numerical study on pressure drop in microchannel flow with different bionic micro-grooved surfaces. *Journal of Bionic Engineering*, 9(1), 99-109.
8. Lu, G., Zhao, J., Lin, L., Wang, X. D., & Yan, W. M. (2017). A new scheme for reducing pressure drop and thermal resistance simultaneously in microchannel heat sinks with wavy porous fins. *International Journal of Heat and Mass Transfer*, 111, 1071-1078.
9. Ludwig, E (2010, May 17). *The Lotus Effect*. Future Prospects. <https://futureprospects.wordpress.com/2010/05/17/the-lotus-effect/>
10. Han, S., Yang, R., Li, C., & Yang, L. (2019). The wettability and numerical model of different silicon microstructural surfaces. *Applied Sciences*, 9(3), 566.
11. Martell, M. B. (2009). Simulations of turbulence over superhydrophobic surfaces. *Masters Theses*, 252.
12. Ou, J., Perot, B., & Rothstein, J. P. (2004). Laminar drag reduction in microchannels using ultra hydrophobic surfaces. *Physics of fluids*, 16(12), 4635-4643.
13. Ou, J., & Rothstein, J. P. (2005). Direct velocity measurements of the flow past drag-reducing ultra-hydrophobic surfaces. *Physics of fluids*, 17(10), 103606.

14. Byun, D., Kim, J., Ko, H. S., & Park, H. C. (2008). Direct measurement of slip flows in superhydrophobic microchannels with transverse grooves. *Physics of Fluids*, 20(11), 113601.
15. Davies, J., Maynes, D., Webb, B. W., & Woolford, B. (2006). Laminar flow in a microchannel with superhydrophobic walls exhibiting transverse ribs. *Physics of fluids*, 18(8), 087110.
16. Gaddam, A., Garg, M., Agrawal, A., & Joshi, S. S. (2015). Modeling of liquid–gas meniscus for textured surfaces: effects of curvature and local slip length. *Journal of Micromechanics and Microengineering*, 25(12), 125002.
17. Li, Q., & Alvarado, J. L. (2015). Thermal performance of microchannels with patterned super-hydrophobic surfaces under laminar flow. *Numerical Heat Transfer, Part A: Applications*, 67(11), 1163-1186
18. Maynes, D., Webb, B. W., Crockett, J., & Solovjov, V. (2013). Analysis of laminar slip-flow thermal transport in microchannels with transverse rib and cavity structured superhydrophobic walls at constant heat flux. *Journal of heat transfer*, 135(2).
19. Cheng, Y., Xu, J., & Sui, Y. (2015). Numerical study on drag reduction and heat transfer enhancement in microchannels with superhydrophobic surfaces for electronic cooling. *Applied Thermal Engineering*, 88, 71-81.
20. Watanabe, K., Udagawa, Y., & Udagawa, H. (1999). Drag reduction of Newtonian fluid in a circular pipe with a highly water-repellent wall. *Journal of Fluid Mechanics*, 381, 225-238.
21. Zhao, J. P., Du, X. D., & Shi, X. H. (2007). Experimental research on friction-reduction with super-hydrophobic surfaces. *Journal of Marine Science and Application*, 6(3), 58-61.
22. Daniello, R. J., Waterhouse, N. E., & Rothstein, J. P. (2009). Drag reduction in turbulent flows over superhydrophobic surfaces. *Physics of Fluids*, 21(8), 085103.
23. Woolford, B., Prince, J., Maynes, D., & Webb, B. W. (2009). Particle image velocimetry characterization of turbulent channel flow with rib patterned superhydrophobic walls. *Physics of Fluids*, 21(8), 085106.
24. Aljallis, E., Sarshar, M. A., Datla, R., Sikka, V., Jones, A., & Choi, C. H. (2013). Experimental study of skin friction drag reduction on superhydrophobic flat plates in high Reynolds number boundary layer flow. *Physics of fluids*, 25(2), 025103.



25. Bidkar, R. A., Leblanc, L., Kulkarni, A. J., Bahadur, V., Ceccio, S. L., & Perlin, M. (2014). Skin-friction drag reduction in the turbulent regime using random-textured hydrophobic surfaces. *Physics of Fluids*, 26(8), 085108.
26. Zhang, J., Tian, H., Yao, Z., Hao, P., & Jiang, N. (2015). Mechanisms of drag reduction of superhydrophobic surfaces in a turbulent boundary layer flow. *Experiments in Fluids*, 56(9), 1-13.
27. Balasubramanian, A. K., Miller, A. C., & Rediniotis, O. K. (2004). Microstructured hydrophobic skin for hydrodynamic drag reduction. *AIAA journal*, 42(2), 411-414.
28. Du, P., Wen, J., Zhang, Z., Song, D., Ouahsine, A., & Hu, H. (2017). Maintenance of air layer and drag reduction on superhydrophobic surface. *Ocean Engineering*, 130, 328-335.
29. Rosenberg, B. J., Van Buren, T., Fu, M. K., & Smits, A. J. (2016). Turbulent drag reduction over air-and liquid-impregnated surfaces. *Physics of Fluids*, 28(1), 015103.
30. Kim, J., Moin, P., & Moser, R. (1987). Turbulence statistics in fully developed channel flow at low Reynolds number. *Journal of fluid mechanics*, 177, 133-166.
31. Min, T., & Kim, J. (2004). Effects of hydrophobic surface on skin-friction drag. *Physics of Fluids*, 16(7), L55-L58.
32. Martell, M. B., Perot, J. B., & Rothstein, J. P. (2009). Direct numerical simulations of turbulent flows over superhydrophobic surfaces. *Journal of Fluid Mechanics*, 620, 31-41.
33. Seo, J., & Mani, A. (2016). On the scaling of the slip velocity in turbulent flows over superhydrophobic surfaces. *Physics of Fluids*, 28(2), 025110.
34. Fairhall, C. T., & García-Mayoral, R. (2018). Spectral analysis of the slip-length model for turbulence over textured superhydrophobic surfaces. *Flow, turbulence and combustion*, 100(4), 961-978.
35. Fairhall, C. T., Abderrahaman-Elena, N., & García-Mayoral, R. (2019). The effect of slip and surface texture on turbulence over superhydrophobic surfaces. *Journal of Fluid Mechanics*, 861, 88-118.
36. Costantini, R., Mollicone, J. P., & Battista, F. (2018). Drag reduction induced by superhydrophobic surfaces in turbulent pipe flow. *Physics of Fluids*, 30(2), 025102.
37. Fuaad, P. A., Baig, M. F., & Ahmad, H. (2016). Drag-reduction in buoyant and neutrally buoyant turbulent flows over super-hydrophobic surfaces in transverse orientation. *International Journal of Heat and Mass Transfer*, 93, 1020-1033.

38. Fuaad, P. A., & Prakash, K. A. (2018). Slip effects on turbulent heat transport over post and ridge structured superhydrophobic surfaces. *International Journal of Heat and Mass Transfer*, 122, 31-44.
39. Ciri, U., & Leonardi, S. (2021). Heat transfer in a turbulent channel flow with superhydrophobic or liquid-infused walls. *Journal of Fluid Mechanics*, 908.
40. Star-CCM+. <https://support.sw.siemens.com/documentation>
41. *Create high quality mesh using Pointwise*. Cadence.  
<https://info.pointwise.com/webinar-structured-meshing-axial-pumps>
42. *High-Quality Unstructured Mesh Generation for Implicit Geometries*. Computing Science Research  
<https://crd.lbl.gov/departments/applied-mathematics/math/software/distmesh-high-quality-unstructured-mesh-generation-for-implicit-geometries/>
43. Celik, I. B., Ghia, U., Roache, P. J., & Freitas, C. J. (2008). Procedure for estimation and reporting of uncertainty due to discretization in CFD applications. *Journal of fluids Engineering-Transactions of the ASME*, 130(7).
44. Schlichting, H., & Gersten, K. (2016). *Boundary-layer theory*. Springer.

## APPENDIX A

### MATLAB CODE FOR SHAPE FACTOR CALCULATIONS

Code for shape factor calculation

```
for j=1:2:200
    for i=1:80
        First_Term(i,j)=1-(Data_New(i,j+1)/Data_New(1,j+1));
    end
    total_disp=0;
    for i=2:80
        displacement(i,j)=(First_Term(i-
1,j)+First_Term(i,j))*(Data_New(i,j)-Data_New(i-1,j))/2;
        total_disp= total_disp+displacement(i,j);
    end
    for i=1:80
        Second_Term(i,j)=(Data_New(i,j+1)/Data_New(1,2))*(1-
(Data_New(i,j+1)/Data_New(1,j+1)));
    end
    total_momentum=0;
    for i=2:80
        momentum(i,j)=(Second_Term(i-
1,j)+Second_Term(i,j))*(Data_New(i,j)-Data_New(i-1,j))/2;
        total_momentum= total_momentum+momentum(i,j);
    end
    First_Shape_Factor(j)= total_disp/total_momentum;
    for i=1:80
        Third_Term(i,j)=(Data_New(i,j+1)/Data_New(1,2))*(1-
((Data_New(i,j+1)^2)/(Data_New(1,j+1)^2)));
    end
    total_energy=0;
    for i=2:80
        energy(i,j)=(Third_Term(i-1,j)+Third_Term(i,j))*(Data_New(i,j)-
Data_New(i-1,j))/2;
        total_energy= total_energy+energy(i,j);
    end
    Second_Shape_Factor(j)= total_energy/total_momentum;
End
```

Where Data\_New is an excel file containing velocity data at 100 different locations along the minichannel

## APPENDIX B

### STARCCM+ MACRO FOR PLANE GENERATION

For the calculation of local shape factor, local boundary layer thickness, local Nusselt number and local convective heat transfer coefficient, data needed to be collected from different locations across the minichannel. Data was collected across 100 planes spread over the streamwise length of the minichannel. To manually create 100 planes would have been a cumbersome tasks. Thus a macro to generate multiple planes was used in StarCCM+. The macro takes in the number of planes, the offset between them and the direction of orientation as an input and then generates the required amount of planes.

The macro is as follows:

```
/ Simcenter STAR-CCM+ macro: PlaneCreation.java
// Written by Simcenter STAR-CCM+ 16.02.009
package macro;

import java.util.*;

import star.common.*;
import star.base.neo.*;
import star.vis.*;

public class PlaneCreation extends StarMacro {

    public void execute() {
        execute0();
    }

    private void execute0() {

        Simulation simulation_0 =
            getActiveSimulation();

        Units units_0 =
```

```
simulation_0.getUnitsManager().getPreferredUnits(Dimensions.Builder().length(1).build());
```

```
Scene scene_1 =  
    simulation_0.getSceneManager().getScene("Geometry Scene 1");
```

```
scene_1.setTransparencyOverrideMode(SceneTransparencyOverride.MAKE_SCENE_TRANSPARENT);
```

```
PartDisplayer partDisplayer_7 =  
    ((PartDisplayer) scene_1.getCreatorDisplayer());
```

```
partDisplayer_7.initialize();
```

```
scene_1.getCreatorGroup().setQuery(null);
```

```
Region region_0 =  
    simulation_0.getRegionManager().getRegion("Pipe_w_3d_0.2delta.Liquid");
```

```
Region region_1 =  
    simulation_0.getRegionManager().getRegion("Pipe_w_3d_0.2delta.Solid");
```

```
scene_1.getCreatorGroup().setObjects(region_0, region_1);
```

```
scene_1.getCreatorGroup().setQuery(null);
```

```
InterfaceBoundary interfaceBoundary_0 =  
    ((InterfaceBoundary)  
    region_0.getBoundaryManager().getBoundary("Liquid_Nonslip [Liquid/Solid]"));
```

```
InterfaceBoundary interfaceBoundary_1 =  
    ((InterfaceBoundary)  
    region_0.getBoundaryManager().getBoundary("Liquid_Slip [Liquid/Solid 2]"));
```

```
scene_1.getCreatorGroup().setObjects(interfaceBoundary_0,  
interfaceBoundary_1);
```

```
PartDisplayer partDisplayer_8 =  
    scene_1.getDisplayerManager().createPartDisplayer("Section Surface", -1, 1);
```

```
partDisplayer_8.initialize();
```

```

int counter = 0;
int Numberofplanes = 100;
int Offset = 0;

while (counter < Numberofplanes) {

    PlaneSection planeSection_1 =
        (PlaneSection) simulation_0.getPartManager().createImplicitPart(new
        NeoObjectVector(new Object[] {}), new DoubleVector(new double[] {0.0, 0.0, 1.0}),
        new DoubleVector(new double[] {(0.0), 0.0, (0.0+(Offset*0.001005696))}), 0, 1, new
        DoubleVector(new double[] {0.0}));
        planeSection_1.getInputParts().setObjects(interfaceBoundary_0,
interfaceBoundary_1);
        counter++;
        Offset++;

    }

}

```

Here the highlighted part refers to the distance between two planes.